University of Colorado
Nuclear Physics Laboratory
Department of Physics
and Astrophysics

Technical Progress Report

Contract AT (11-1)-535

November 1, 1973
COO-535-693

MASTER

DISTRIBUTION OF THIS DOCUMENT IS UNLIMITED

DISCLAIMER

This report was prepared as an account of work sponsored by an agency of the United States Government. Neither the United States Government nor any agency Thereof, nor any of their employees, makes any warranty, express or implied, or assumes any legal liability or responsibility for the accuracy, completeness, or usefulness of any information, apparatus, product, or process disclosed, or represents that its use would not infringe privately owned rights. Reference herein to any specific commercial product, process, or service by trade name, trademark, manufacturer, or otherwise does not necessarily constitute or imply its endorsement, recommendation, or favoring by the United States Government or any agency thereof. The views and opinions of authors expressed herein do not necessarily state or reflect those of the United States Government or any agency thereof.

DISCLAIMER

Portions of this document may be illegible in electronic image products. Images are produced from the best available original document.

24,717

TECHNICAL PROGRESS REPORT

CONTRACT AT(11-1)-535

November 1, 1973

COO-535-693

NOTICE

This report was prepared as an account of work sponsored by the United States Government. Neither the United States nor the United States Atomic Energy Commission, nor any of their employees, nor any of their contractors, subcontractors, or their employees, makes any warranty, express or implied, or assumes any legal liability or responsibility for the accuracy, completeness or usefulness of any information, apparatus, product or process disclosed, or represents that its use would not infringe privately owned rights.

MASTER

DISTRIBUTION OF THIS DOCUMENT IS UNLIMITED

TABLE OF CONTENTS

Page

I. INTRODUCTION. 1

II. EXPERIMENTAL PROGRAM. 2

A. Nuclear Physics 2

1. Charged Particle Experiments. 2

a. Single-Nucleon Transfer Reactions . . . 2

i. $^{107}Ag(p,d)^{106}Ag$ and $^{106}Pd(p,d)^{105}Pd$ Reactions 2

ii. Comparison of (α,τ) and (α,t) Reactions on ^{24}Mg 3

iii. The (d,d*) and (d,p) Reactions on ^{12}C at 17.3 MeV 4

b. Two or More Nucleon Transfer Reactions. 7

i. Violation of Isospin Conservation in Two-Nucleon Pickup Reactions. . . . 7

ii. The $^{90,92,94,96}Zr(p,\alpha)^{87,89,91,93}Y$ Reactions. 7

iii. Preliminary Studies of $(^3He,^7Be)$ Using the Magnetic Spectrometer . . 8

c. Charge Exchange Reactions 9

i. Charge Exchange Reactions on ^{91}Zr . 9

d. Elastic and Inelastic Scattering. . . . 10

i. Scattering of 27-MeV Protons by Polarized ^3He 10

ii. $^{89}Y(\alpha,\alpha')$ at 35.60 MeV. 11

iii. Strong Absorption Radii of ^{70}Ge and ^{72}Ge. 12

iv. Inelastic Scattering of Protons and Alpha Particles from ^{40}Ca 14

v. A Study of the Helion Optical Potential Ambiguities for ^{40}Ca and ^{58}Ni. 14

vi. $^{40}Ca(\alpha,\alpha)$ and $^{58}Ni(\alpha,\alpha)$ at 82.0 and 85.6 MeV. 17

2. Gamma Ray Experiments and Beta Decay. . . . 21

a. The Decay of ^{36}K. 21

b. $(^3He,2n)$ Reaction Cross Sections on Several Light Nuclei. 22

c. The Level Structure of ^{88}Y and ^{90}Y from a Study of the $(\alpha,n\gamma)$ Reaction. 24

Page

d. Ge(Li) Detector Efficiency Calibration Using Resonant Proton-Capture Gamma Rays. 26
e. Sodium-20 Beta Decay. 26
f. The $^{133}Cs(\alpha,n\gamma)$ Reaction. 27
g. The Level Structure of ^{106}Ag by the $^{103}Rh(\alpha,n\gamma)$ Reaction. 28
h. Search for Delayed Gamma Rays from the $^{91}Zr(p,\alpha)^{88}Y$ Reaction 30
i. Total Cross Sections and Excitation Functions for ^{1}H, ^{2}H, ^{3}He, and ^{4}He on Targets of Natural Mg, Al, and Si 30
j. Measurements of Gamma Ray Branching Ratios in ^{28}Al 33

3. Neutron Time-of-Flight Experiments. 35

a. The (p,n) Reaction on High Z Elements . . 35
b. Widths of Analog States in Heavy Elements 38
c. Neutron-Proton Density Distributions. . . 41
d. Comparison of (p,n) Reaction Cross Section with Activity Measurement for ^{13}C 42
e. Differential Cross Sections for $^{10}B(p,n)^{10}C$ and $^{11}B(p,n)^{11}C$ and Some Macroscopic Reaction Relationships. 44
f. The Anti-Analog State Transition $^{56}Fe(p,n)^{56}Co(0^{+}AAS)$. 48

4. Other Activities. 51

a. Thick Target Measurement of Stellar Reaction Rates. 51
b. Trace Element Analysis. 53

i. Trace Amounts of Fluorine Determined by the $^{19}F(p,p'\gamma)$ Reaction. 53

c. Neuron Damage by Alpha Particles 56

5. X-Ray Fluorescence Analysis 59

a. Introduction. 59
b. Developmental Work. 59
c. The Molybdenum Project. 60
d. Trace Element Imbalance in Uremia 61
e. Outside Services. 65

B. Intermediate Energy Physics 67

1. Proposal for the Study of Giant Multipole Resonances by Pion Scattering at LAMPF. . . . 67
2. Phase Shift Fits to Pion Elastic Scattering . 67
3. Slit Scattering in the EPICS Beam Line. . . . 68

Page

4. Glauber Calculation of Pion-Deuteron Scattering . 69

C. Apparatus and Facility Development. 71

1. The Magnetic Spectrograph System. 71

a. Introduction. 71
b. The Beam Swinger. 72
c. Zoom Lens and Charged Particle Spectrograph . 75
d. Magnetic Spectrograph Trim Coils. 78
e. Focal Plane Detection 78
f. Experimental Results. 83
g. Present Status and Expected Improvements. . . 83

i. Scattering Chamber. 85
ii. Electrostatic Deflection Plates 85
iii. Acceptance Solid Angle Delimitation with Slits 85

2. Development of Time-of-Flight System. 86

a. Beam Swinger. 86
b. Detectors 86
c. 30 Meter Flight Path Facility 86

3. Short Rabbit. 89

4. A High-Pressure Gas Rabbit. 91

5. Fast Neutron Beam 93

a. New Beam Line 93
b. Collimator. 94
c. Targets 94
d. Time-of-Flight Thick Target Yield and Spectra Studies 94
e. Work in Progress. 95

6. Computer Program Development. 96

a. OPTICS. 96
b. SPECTR. 96
c. PEAKFIND. 96
d. Energy Loss Calculations. 96

7. Electronics Maintenance and Development 98

D. Cyclotron Operation 100

E. Outside Users of Cyclotron Facilities 102

Page

III. THEORETICAL PROGRAM. 103

A. Pionic Reaction Investigations 103

Dup. — B. Microscopic Calculations of (p,n) Reactions to Isobaric Analog States. 104

C. Microscopic Studies of (p,n) Reactions to Unbound Final States 108

D. Effective Deuteron Optical Potential in (p,d;d,n) Processes. 110

E. Macroscopic Analysis of (p,n) Reactions. 114

F. Computer Code Developments 116

IV. PUBLICATIONS AND REPORTS 117

A. Published Articles 117

B. Articles Submitted for Publication 118

C. Published Abstracts and Conference Presentations . . . 119

D. Theses 121

V. PERSONNEL. 122

I. INTRODUCTION

This report summarizes the work carried out at the Nuclear Physics Laboratory of the University of Colorado during the period November 1, 1972, to November 1, 1973, under Contract AT(11-1)-535 between the University of Colorado and the United States Atomic Energy Commission.

This year has seen both the energy-loss spectrograph and the rotating-beam neutron time-of-flight spectrometer come into routine use. These facilities share the beam preparation system known as the beam swinger and have operated in adjacent weeks with almost no loss of running time for change-over. The energy-loss design of the spectrograph has fulfilled expectations. As an example, an unanalyzed 10 microampere proton beam has been used in (p,d) studies with an overall excitation energy resolution of 9 keV. Our 30-meter flight path facility for neutron time-of-flight measurements has been utilized for a study of the anti-analog state in ^{56}Co. This state is extremely weak at large angles and the 50 keV resolution obtainable for neutrons was essential.

The flexibility of the cyclotron as a research tool still manages to impress us all. It produces very intense beams over its full energy range and these beams are naturally pulsed as required for time-of-flight work. The energy range of the machine has never been fully studied, but in this past year it has been used for experiments requiring 10 μa of protons at energies ranging from 267 keV to 28 MeV.

The theoretical group has continued to study the effects of two-step processes in nuclear reactions. This work has often complemented that of the experimental group. Present indications are that features of the macroscopic model of nucleon-nucleus interactions may well be understood in terms of a microscopic one-step plus two-step model. This has been shown by a detailed analysis of the (p,n) measurements made here. Theoretical studies of pion-nucleus interactions are being continued by both the theoretical group and the LAMPF users group.

The trace element analysis program at the laboratory has continued and some very useful results have been forthcoming in both environmental and medical problems. A neutron beam for cancer therapy is being developed with a high-pressure deuterium target giving a spectrum that looks very useful.

II. EXPERIMENTAL PROGRAM

A. Nuclear Physics

1. Charged Particle Experiments

a. Single-Nucleon Transfer Reactions

14853

i. $^{107}Ag(p,d)^{106}Ag$ and $^{106}Pd(p,d)^{105}Pd$ Reactions - R. J. Peterson, J. J. Kraushaar, B. W. Ridley, and R. A. Ristinen

These reactions were studied with the energy loss spectrometer over an angular range from 1° to 70°; an excitation range of 0-1.5 MeV in the final nucleus; and with an energy resolution of ~ 10 keV. (See Fig. A1-1.) The original purpose was to aid the assignment of excitation energies to the ^{106}Ag levels from the gamma ray spectrum observed in the $^{103}Rh(\alpha,n\gamma)$ reaction.[1] The spin $1/2^-$ of the ^{107}Ag ground state allows close limits on the final spin to be placed by observation of the shapes of the angular distribution populating the state. To calibrate these shapes, the $^{106}Pd(p,d)$ reaction was studied to observe the population of states of known spin.[2]

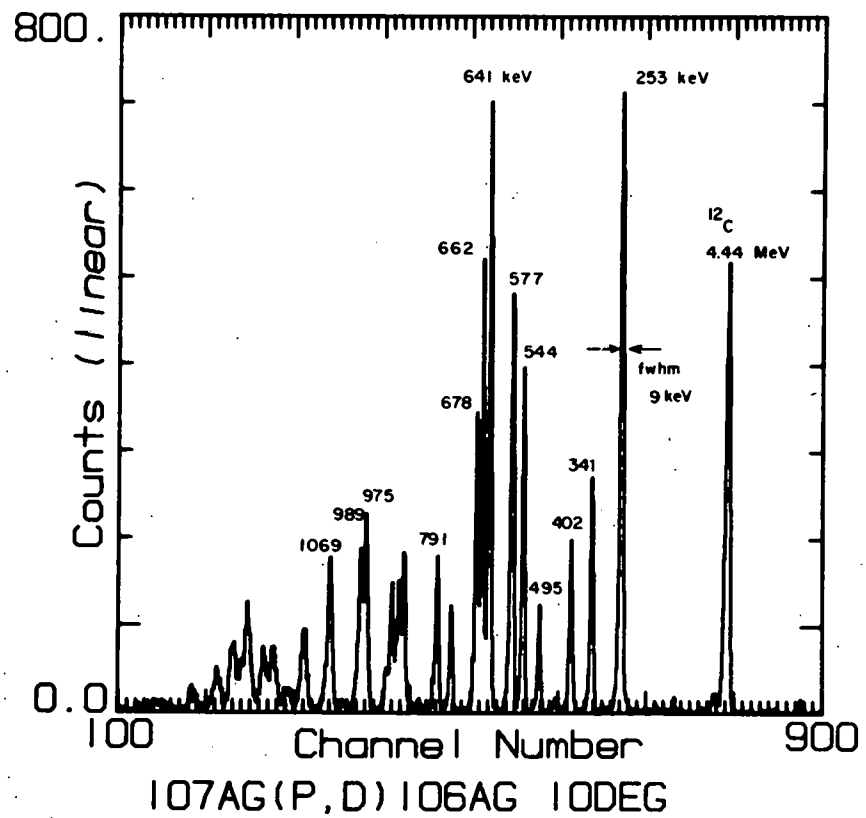

Fig. A1-1 The levels of ^{106}Ag as populated by the (p,d) reaction. The ground state is not seen, so a constant offset of a few keV for the excitation energies may result from our final analysis.

The ground state of ^{106}Ag is very weakly populated, and obscured by a state in ^{108}Ag from an isotopic target impurity. A very weak $\ell=0$ excitation to a state near 95 keV constrains that state to spin 0^- or 1^- spin. This state is seen in the gamma ray decay scheme. A number of $\ell=2$ (final $J^{\pi}=1^-, 2^-, 3^-$) patterns are seen, as shown in Fig. A1-2 where the ground state data from ^{105}Pd are also shown. More than a score of angular distributions have been measured for ^{106}Ag, and will provide much information on this hitherto unexplored nucleus. Several new levels also appear in the spectrum of ^{105}Pd.

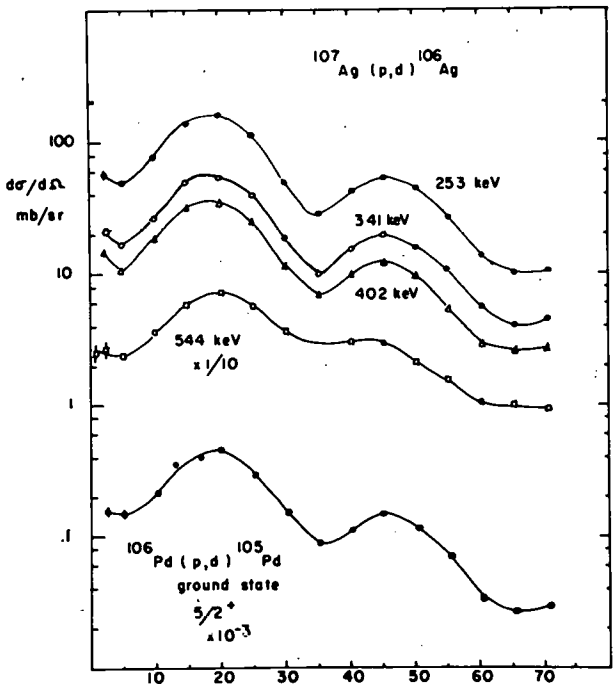

Fig. A1-2 Differential cross sections from ^{107}Ag and ^{106}Pd are compared for representative levels. The absolute yield has not been determined well, but the normalization between the two targets is good to within ±10%. The lines serve only to guide the eye.

---

[1] R. L. Bunting and J. J. Kraushaar, this report, sect. II-A-2-g.
[2] C. M. Lederer, J. M. Hollander, and I. Perlman, Table of Isotopes, UCRL, (1966).

ii. Comparison of (α,τ) and (α,t) Reactions on ^{24}Mg - P. D. Ingalls, L. D. Rickertsen, and H. Rudolph

The reaction-mechanism study of these mirror reactions which was begun last year continues. The large (~ 300%) enhancement of (α,τ) over the equality of (α,τ) and (α,t) cross sections predicted by naive charge symmetry emerges naturally from the Coulomb differences between these two reactions even in a simple one-step distorted-wave treatment. Observed differences in angular distributions for excited states, however, are not predicted without a more realistic

treatment. It is known that multistep processes through inelastic channels are important in this mass region[1] and it was considered important to include these effects explicitly in Coupled Channel Born Approximation (CCBA) calculations.[2] Preliminary calculations indicate that transitions through inelastic channels in both initial and final nuclei are as strong as the direct term we considered in the DWBA analysis. Further calculations are in progress.

---

[1] R. O. Nelson and N. R. Roberson, Phys. Rev. C 6 (1972) 2153.
T. Udagawa, preprint, Univ. of Texas, (1973).

[2] T. Tamura, Oak Ridge National Laboratory Report ORNL-4152.
R. J. Ascuitto and N. K. Glendenning, Phys. Rev. C 2 (1970) 415, 1260.

24,854

iii. The (d,d*) and (d,p) Reactions on ^{12}C at 17.3 MeV - M. L. Munger and R. J. Peterson

Using a 200 μg/cm^2 natural carbon foil, angular distributions corresponding to the first four energy levels of ^{12}C and excitations of ^{13}C--up to 9.9 MeV (excluding 7.68 MeV), 10.75 MeV, and 11.08 MeV--were obtained with a solid state counter telescope. (See Fig. A1-3.)

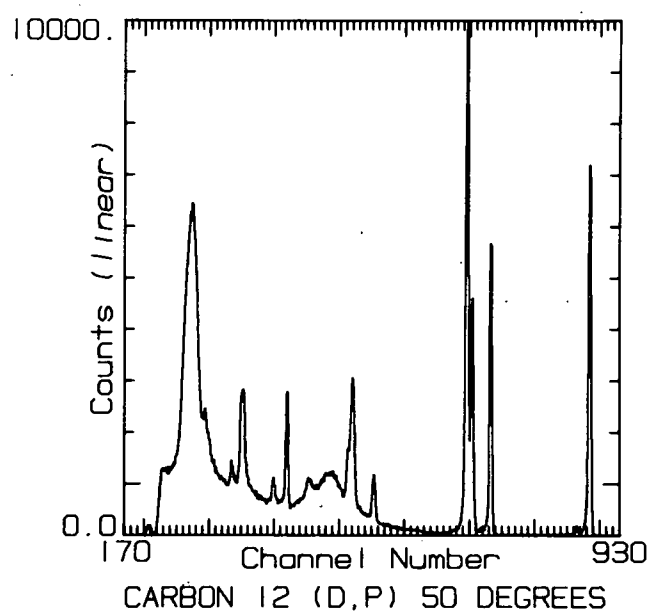

Fig. A1-3 A proton spectrum from the $^{12}C(d,p)$ reaction. The three states near 3 MeV are near channel 700, the ground state near channel 880.

Standard DWBA calculations were carried out using various optical model parameters. For inelastic scattering to the 2^+ state, HD, ref. 1), SA ref. 2) parameters, as well as Coupled Channels, ref. 3) calculations were used to fit the data (Fig. A1-4). The shape depends on the parameter set used with a slight improvement on SA parameters using coupled channels. These parameters (SA) were used in CC calculations in a spinless form. Spectroscopic factors for

excitation of ^{13}C levels were found which are in reasonable agreement to the corresponding work of Darden et al. (ref. 1). Additional levels are included and the results summarized in Table A1-I.

Additional coupled channel calculations are underway for the (d,p) reaction and will be presented at the Bloomington meeting of the American Physical Society, Nov., 1973.

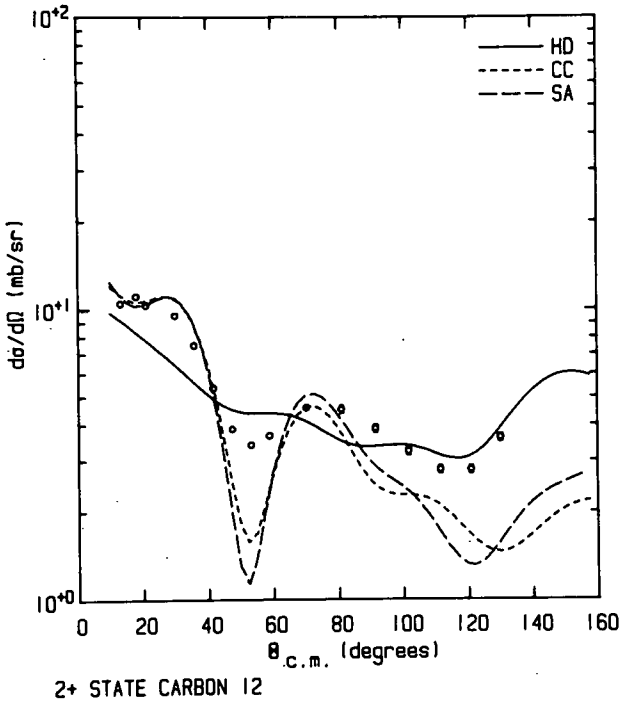

Fig. A1-4 Three sets of optical model parameters are used to generate the curves shown for the inelastic deuteron scattering from ^{12}C.

TABLE A1-I

Results on states in ^{13}C

Excitation Energy (MeV)	J^{π}	Spectroscopic Factors Ref. 1) @ 13.3 MeV	present
Ground	$1/2^-$	1.1	1.0
3.086	$1/2^+$	1.1	1.0
3.684	$3/2^-$	0.1	0.15
3.854	$5/2^+$	1.1	1.05
6.864	$5/2^+$	0.04	0.07
7.492	$(3/2^-)$		0.27
7.549	$5/2^-$		0.07
8.25	$3/2^+$	1.0	1.0
8.858	$1/2^-$	0.5	0.37
9.504	$3/2^-$		0.63
9.896	$3/2^-$	0.1	0.09
10.748	$7/2^+$		0.17
11.078	$1/2^-$		0.17

[1] S. E. Darden, S. Sen, H. R. Hiddleston, J. A. Aymar, and W. A. Yoh, Nucl. Phys. A208 (1973) 77.
[2] G. R. Satchler, Nucl. Phys. 85 (1966) 273.
[3] P. D. Kunz, code CHUCK, private communication.

b. Two or More Nucleon Transfer Reactions

i. Violation of Isospin Conservation in Two-Nucleon Pickup Reactions - P. D. Ingalls

Last year it was reported that the cross section ratio for the analog reactions $^{16}O(p,\tau)^{14}N$(2.31 MeV, T=1) and $^{16}O(p,t)^{14}O$(g.s.) at 27.0 MeV shows agreement with the value $k_\tau/2k_t$ predicted by isospin conservation only at small angles ($\theta_{LAB} < 25°$). At larger angles the experimental ratio rises to a value 300% above the expected value, in marked contrast to a large number of $(p,\tau)/(p,t)$ comparisons at higher energies. Standard local, zero-range DWBA calculations were performed with several sets of distorted wave parameters, (including those from successful higher-energy calculations), to see if known Coulomb effects account for the violation of isospin conservation. These calculations were too sensitive to the parameter choices to be useful. In addition, large deviations from the ratio predicted by isospin conservation were predicted, even at forward angles, where experiment shows precise agreement. We conclude that at present we lack a useful way to treat Coulomb effects (and the associated Q-value effects) in (p,τ) and (p,t) reactions at this relatively low energy.

This work was recently reported.[1]

---

[1] P. D. Ingalls, Phys. Rev. Letters 31 (1973) 605.

24,855

ii. The $^{90,92,94,96}Zr(p,\alpha)^{87,89,91,93}Y$ Reactions - R. J. Peterson and H. Rudolph

The data and analyses for these reactions are complete and being prepared for publication. The reaction was demonstrated to proceed by a direct, pickup mechanism. States of spins $1/2^-$, $3/2^-$, and $5/2^-$ in the yttrium isotopes were readily identified. Cluster pickup predictions with the DWBA were successful in reproducing the shapes for the population of known spin states. One observation of interest is the population of states of ^{87}Y at 2.627 and 2.569 MeV, with angular distributions expected for spins $13/2^-$ and $15/2^-$, as shown in Fig. A1- 5. These are evidently due to the coupling of a $p_{1/2}$ proton hole to a 6^+ state of ^{88}Zr, the latter formed by two holes in double-magic ^{90}Zr.

7-8

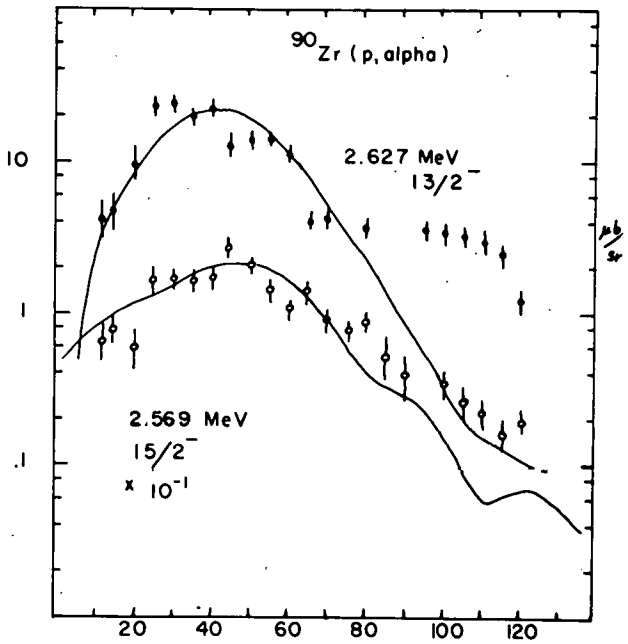

Fig. A1-5 Angular distribution (points) and DWBA calculations (solid curves) for the 2.569 and 2.627 MeV levels of ^{87}Y. These levels probably represent the coupling of a $p_{1/2}$ proton to a 6+ state in ^{88}Zr.

iii. <u>Preliminary Studies of (^3He, ^7Be) Using the Magnetic Spectrometer</u> - R. A. Emigh, C. D. Zafiratos, and C. S. Zaidins

We are currently preparing to study the (^3He, ^7Be) reaction in the tin-tellurium mass region. The outgoing ^7Be ejectile is somewhat hindered by the Coulomb barrier at energies obtainable with our cyclotron. Preliminary counter telescope studies indicated forward angle cross-sections of approximately 1 μb/sterad. We now plan to carry out the measurements with the new magnetic spectrograph. The present multi-wire proportional chamber (MWPC) detector cannot detect Be ions because of excessive energy losses in the windows and chamber gas. A new MWPC is being constructed to operate at lower gas pressures and with thinner entrance windows for heavy ion detection.

c. Charge Exchange Reactions

i. Charge Exchange Reactions on ^{91}Zr - P. D. Ingalls and H. Rudolph

We have measured the $^{91}Zr(\tau,t)^{91}Nb$ (IAS) angular distribution, and have observed the subsequent proton decay $^{91}Nb(IAS) \rightarrow \tilde{p} + {}^{90}Zr$ at 24.5 ± 0.2 MeV, in both singles and coincidence $(\tau,t\tilde{p})$ experiments. By directly measuring the total cross section (~130 μb) and observing the decay protons in the same experiment, it is possible to check the delayed-proton method of measuring charge-exchange cross sections. This method has often been used in $(p,n\tilde{p})$ studies to avoid the need to detect neutrons. Our check is of current interest because some $(p,n\tilde{p})$ cross section measurements exceed integrated (p,n) angular distribution yields by 300%.

The kinematic broadening (~560 keV) and shape expected for the singles $(\tau,t\tilde{p})$ spectrum were calculated from the (τ,t) angular distribution, and the proton energy scale was unambiguously determined in a subsidiary $(p,n\tilde{p})$ experiment. When a quadratic background determined for channels immediately above and below the calculated $(\tau,t\tilde{p})$ group was subtracted, a yield of 4670 ± 2300 counts remained, to be compared with 4150 counts expected from the measured total cross section. The agreement is satisfactory, but one cannot strongly rule out an enhancement of 150%-200% on the basis of the singles experiment.

The coincidence experiment provides a more satisfactory check. A 32-hour run (θ_t=35.3°, θ_p=90°) produced 26 ± 7 t-$\tilde{p}$ coincidences above background, in agreement with the number 35 ± 7 expected from the (τ,t) cross section.

This work is complete and will shortly be submitted for publication in Nuclear Physics.

d. Elastic and Inelastic Scattering

(24,856) i. Scattering of 27-MeV Protons by Polarized ^{3}He - R. H. Ware, P. D. Ingalls, and W. R. Smythe

Measurements of the analyzing power of protons for polarized ^{3}He (p_3) previously obtained at 4-11 MeV[1] and 19.4 MeV[2] proved useful in determining phase shift parameters describing p-^{3}He scattering. We have extended these measurements to a higher energy, which tests a prediction of a phase shift analysis at 27 MeV.[3]

We have measured p_3 at 13 lab angles from 30° to 150° using a ^{3}He target polarized by optical pumping.[4] (Fig. A1-6) Left and right scatterings from the 10% to 15% polarized target were measured simultaneously. Geometrical asymmetries were cancelled by reversing the helicity of the circularly polarized optical pumping light, which reverses the target polarization.

Target innovations include thin Havar foil windows for beam entrance and exit as well as wide angle (30°) scattering windows which allow observation of recoil ^{3}He and scattered protons. p_3 was measured for 19.4 MeV protons at a single angle to compare our polarization calibration with the results of Baker et al.[2] In addition, the elastic scattering cross section for ^{3}He(p,p)^{3}He was also measured at 26.7 MeV for 36 lab angles from 15° to 165° for use in conjunction with the p_3 data. (Fig. A1-7 .)

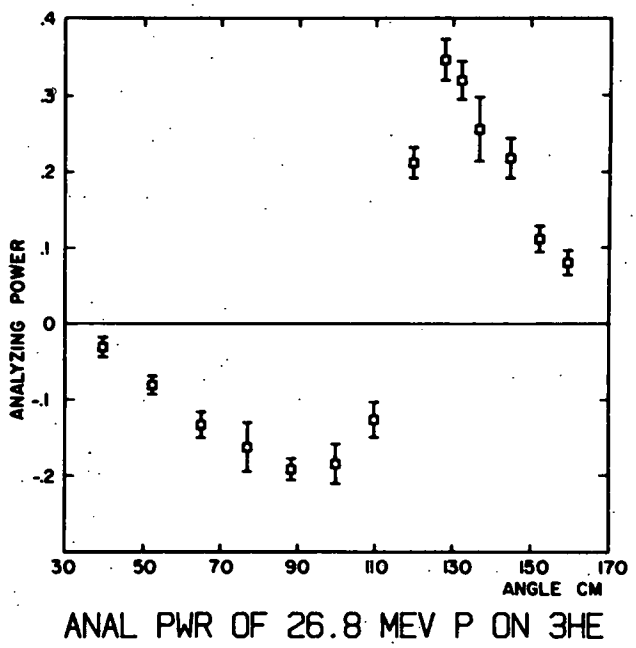

Fig. A1-6 The analyzing power, p_3, for 26.8 MeV protons on ^{3}He as determined by left-right scattering measurements from a polarized ^{3}He target.

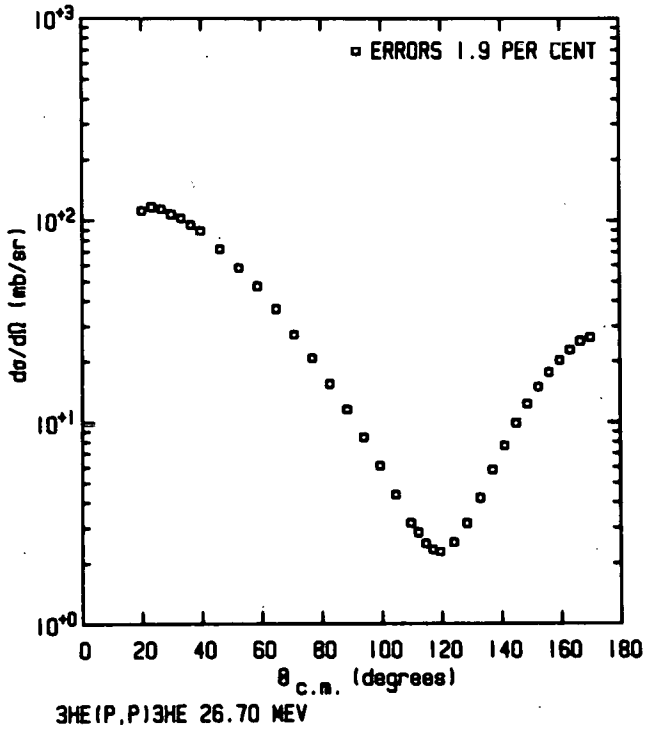

Fig. A1-7 Angular distribution for protons elastically scattered by ^{3}He.

An attempt to obtain an absolute calibration of the ^{3}He target polarization is in progress. It involves observation of ^{4}He scattering at angles and energies where the analyzing power of ^{4}He is predicted to be unity by a theorem of Plattner and Bacher.[5]

---

[1] S. D. Baker, D. H. McSherry, and D. O. Findley, Phys. Rev. 178 (1969) 1616.
[2] S. D. Baker, T. A. Cahill, P. Catillon, J. Durand, and D. Garreta, Nucl. Phys. A160 (1971) 428.
[3] J. R. Morales, Ph.D. Thesis, Univ. of Calif. at Davis (1970).
[4] F. D. Colgrove, L. D. Schearer, and G. K. Walters, Phys. Rev. 132 (1963) 2561.
[5] G. R. Plattner and A. D. Bacher, Phys. Lett. 36B (1971) 211.

ii. ^{89}Y(α,α') at 35.60 MeV - R. J. Peterson

In anticipation of future studies of pion scattering from ^{89}Y at LAMPF,[1] we will study the inelastic scattering of alpha particles using our high-resolution spectrometer. A thorough understanding of the spectroscopy of ^{89}Y is needed, and many questions remain concerning its level structure.[2] As a check of the normalization of the soon-to-be-taken spectrometer data, we have used solid-state counters for a preliminary survey, with known efficiency and 80 keV resolution. Fig. A1-8 shows the observed elastic scattering and

the optical model parameters used for the fit shown. The inelastic data indicate L=3 transitions to states at 2.22, 2.53, 2.89, and 3.75 MeV, and L=2 transitions to states at 1.51, 1.75, 3.15, 4.02, and 4.20 MeV. These results will be supplemented soon with spectrometer data.

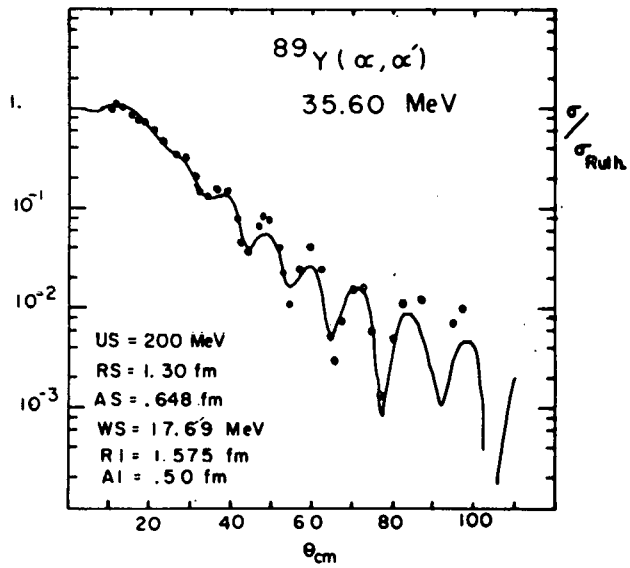

Fig. A1-8 Angular distribution of 35.6 MeV alpha particles elastically scattered by ^{89}Y. The solid curve is an optical model calculation with the parameters shown in the figure.

---

[1] LAMPF proposal number 49, R. J. Peterson, spokesman.
[2] M. W. Johns, et al., Nucl. Data 8 (1970) 373.

iii. Strong Absorption Radii of ^{70}Ge and ^{72}Ge - R. J. Peterson and R. Graetzer

The elastic scattering cross sections of 35.563 MeV alpha particles from ^{70}Ge and ^{72}Ge was measured carefully over an angular range 10-70 degrees. The data were fitted with the optical model, and several schemes for extracting the strong absorption radius were used. The real partial wave coefficients computed from the optical model pass through one-half at $\ell_{\frac{1}{2}}$, with $\ell_{\frac{1}{2}}$ equal to 16.40±.02 and 16.71±.03 for ^{70}Ge and ^{72}Ge, respectively. By the methods of Ref. 1 these give R_{sa}=8.329 and 8.448 fm. The absorption coefficients crossing through one-half give R_{sa}=8.580 and 8.669 fm. The use of the partial total cross sections gives 8.649 and 8.767 fm. The mean of the ratios of these values for $^{72}Ge/^{70}Ge$ is 1.013±.002. If the dependence were as $A^{1/3}$, the ratio would be 1.0095. Thus, the strong absorption radius for ^{72}Ge is very slightly larger than expected from the $A^{1/3}$ dependence, and the shell closure at N=40 has not caused this nucleus to become smaller.

---

[1] B. Fernandez and J. S. Blair, Phys. Rev. C1 (1970) 523.

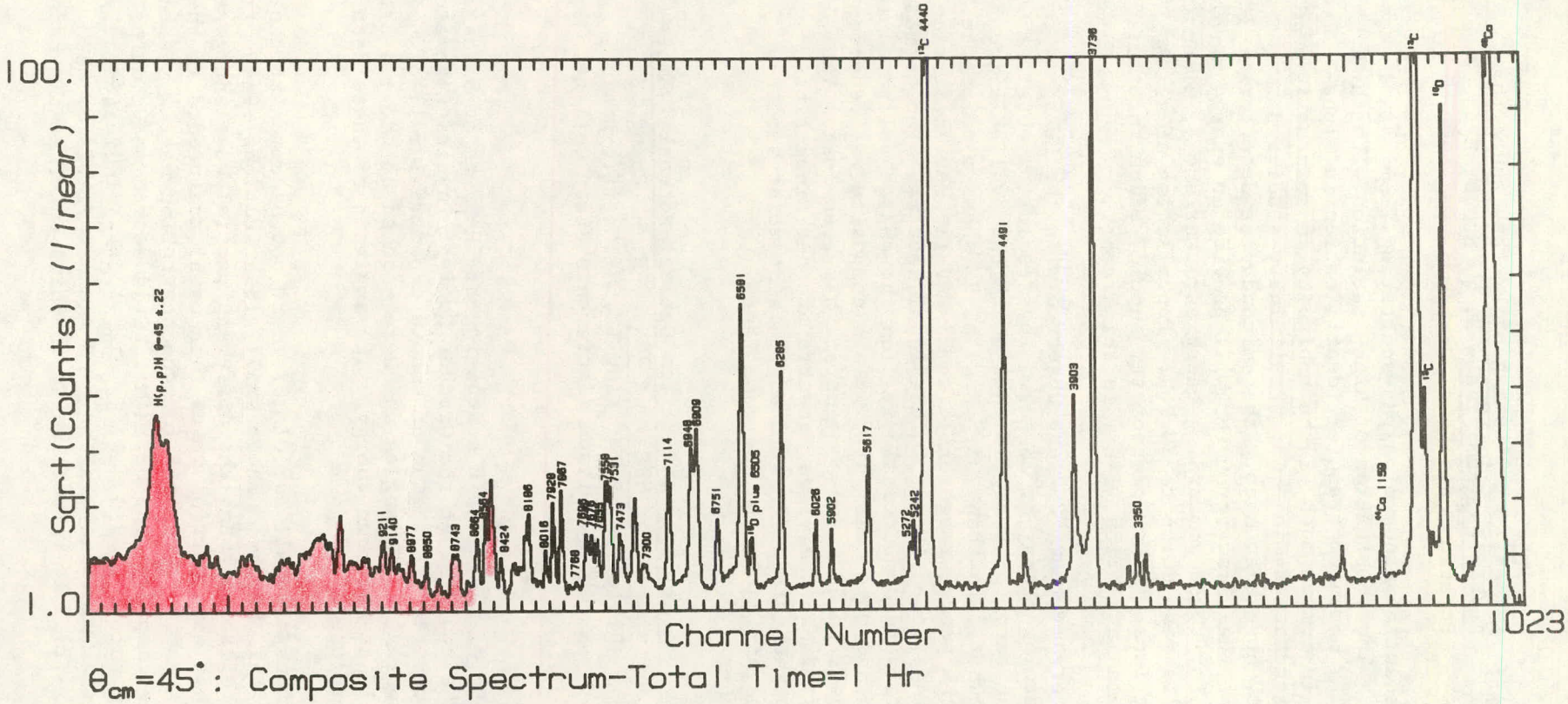

Fig. A1-9 Spectrum of protons scattered by ^{40}Ca at E_p=23 MeV. This is a composite position spectrum from the multi-wire proportional counter focal plane detector of the CU energy-loss spectrograph. It was obtained in less than one hour of total running time though five different settings of the spectrometer were required for the 12 MeV of excitation energy it covers.

iv. Inelastic Scattering of Protons and Alpha Particles from ^{40}Ca - E. W. Stoub, R. J. Peterson, and R. A. Ristinen

A high-resolution study of alpha-scattering from ^{40}Ca is in preparation. The combination of high resolution with the clear-cut angular momentum transfer identification in alpha-scattering should remove much of the ambiguity in spin assignments for highly excited states in ^{40}Ca. Preliminary studies at E_α=28 and 35 MeV have been made with semiconductor detectors. It is expected that the CU spectrometer will provide an energy resolution of 15 keV for these bombarding energies. Currently, kinematic broadening limits resolution to 30 keV. Installation of slits within the zoom lens of the spectrometer should reduce this to 15 keV, as described in section II-C-1 in this report.

Protons scattered from ^{40}Ca were observed with the CU spectrometer at a bombarding energy of 23 MeV. The resolution obtained was 15 keV. The range of energies that covers the available focal surface is somewhat less than 20%. Fig. A1-9 shows a composite spectrum with the energy range of 11 to 23 MeV (12 MeV excitation). This spectrum is a composite of 5 individual spectra. The normalization constants were computed simply from the charge collected in the Faraday cup and were near unity. This composite was reduced from 4000 channels to 1024 and some detail has been lost. The matching points of the individual spectra are not discernible indicating that the effective solid angle is at worst smoothly changing with magnification in the zoom lens.

v. A Study of the Helion Optical Potential Ambiguities for ^{40}Ca and ^{58}Ni - H. H. Chang, B. W. Ridley, N. S. P. King (U. of Calif., Davis), and E. F. Gibson (Sacramento State College)

Measurements of the elastic scattering of ^{3}He ions at 83.5 MeV were done on ^{40}Ca and ^{58}Ni at the Crocker Nuclear Physics Laboratory. These new data covered the region of smooth exponential fall-off of the cross sections at large angles and were matched to the old data taken at Harwell[1] at the same energy. The analysis of these data has now been completed.

Cross sections as small as .01 μb/sr are not uncommon at the large angles at this energy. These small cross sections result from destructive cancellation among the different partial wave scattering amplitudes so that more partial waves than usual are needed in the calculations. A variable cut-off for the scattering matrix elements was added to the computer code OPTIM(M). Grid search on V_o using a fixed spin orbit term (V_{so}=2.0 MeV, $R_{so}=R_R$, $A_{so}=A_R$) indicated only one acceptable minimum valley in the χ^2/N against V_o plane, as shown in Fig. A1- 10. It is worthwhile to point out that the rate

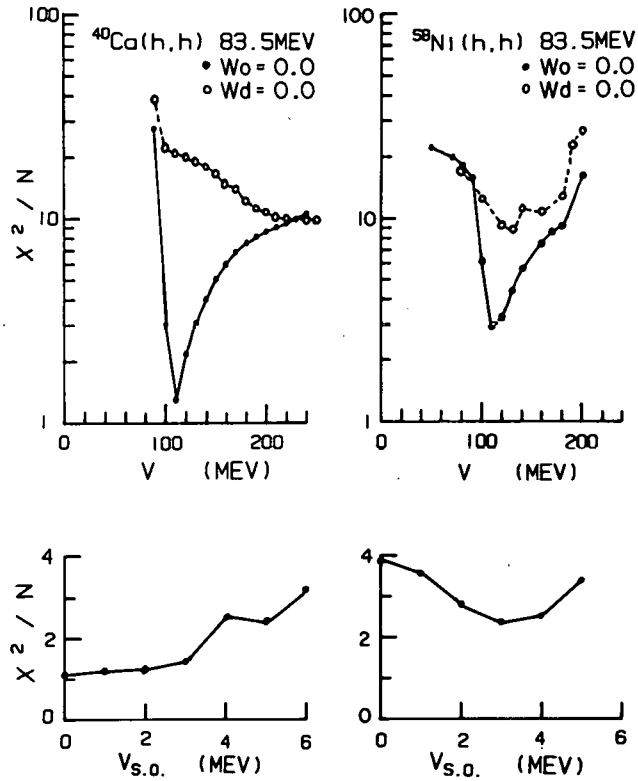

Fig. A1-10 χ^2/N vs. V or V_{so} for 83.5 MeV helion elastic scattering from ^{40}Ca and ^{58}Ni for potentials with either surface (solid line) or volume absorption (dashed line). In the upper portion of the figure V_{so} was fixed at 2.0 MeV. $R_{so}=R_R$, $A_{so}=A_R$ were assumed in all the searches.

of the exponential fall-off of the cross sections at large angle plays an important role in distinguishing between a volume or a surface imaginary potential used. In general, these results are in agreement with other reports,[2] except a much better choice can be made here.

The spin-orbit potential plays a similar role in damping the oscillation of the calculated cross section at small angles. However, it predicts either larger or smaller cross sections at large angles depending whether a large or small spin-orbit interaction was used. Unfortunately the small cross sections are difficult to measure and make the distinction between a large or small spin-orbit interaction a difficult task. The χ^2/N's against different V_{so} are shown in the lower half of Fig. A1-10.

In conclusion, we found the V_o~110 MeV with a surface absorption family give an excellent fit to the elastic scattering cross section

extended far into the region where structureless exponential fall-off of the cross section was observed. In addition, only very minor changes in the optical parameters are required when the large angle data are added in the search.

Serious ambiguities in the optical parameters are observed in the lower energy data of helion elastic scattering due to the strong absorption of the helion particle inside the nucleus. Previous studies[3] to extract energy dependent helion optical potentials over a large collection of elastic scattering data at several different energies did not give a very consistent set of optimum potentials even for the family now considered to be the correct one. It appeared that different energy dependent terms were required for different targets. To investigate this peculiar phenomena, we now start from the optical potential parameters obtained by simultaneously fitting the 83.5 MeV data on ^{40}Ca and ^{58}Ni. The optical calculations are shown as the solid line in Fig. A1-11 . By fixing the geometry parameter R_R, A_R, R_I, A_I, we

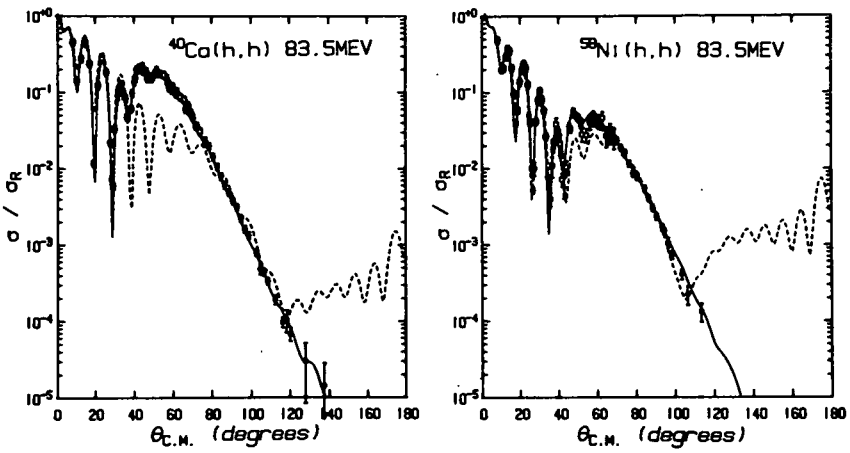

Fig. A1-11 Optical model predictions compared with 83.5 MeV helion elastic scattering from ^{40}Ca and ^{58}Ni. Solid line, V=110 MeV; dashed line, V=170 MeV. Surface absorption was used in these calculations. The values of χ^2/N for the dashed line are larger than those displayed in Fig. A1-10 in which most of the solid points belong to the V_o=100 MeV family (continuous ambiguities of this family).

performed a two-parameter (V_o, W_d) search on each set of data at fixed bombarding energy with the results shown in Fig. A1-12 . Both V_o and W_d change linearly with energy from 83.5 MeV down to 35 MeV. A sudden departure from the linear dependence is obvious for the ^{58}Ni(h,h) below 35 MeV. In fact, the optical parameters obtained from the two-parameter search did not belong to the original family. Similar energy dependent terms of the optical potentials are expected on different targets. Care must be exercised over the range of

energy considered if a linear term is assumed.

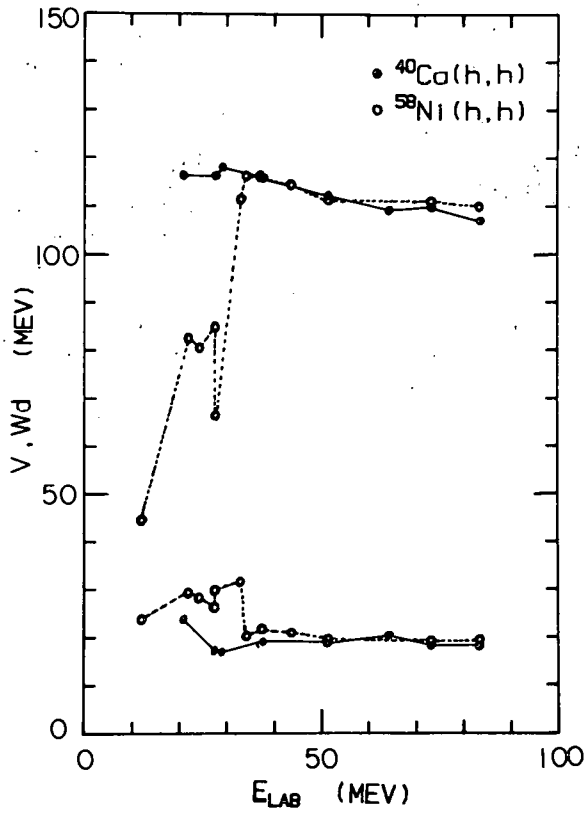

Fig. A1-12 Final values of V and W_d resulting from two-parameter search on ^{40}Ca and ^{58}Ni at several different energies. The geometry parameters are obtained from a simultaneous fit to the 83.5 MeV helion scattering data on ^{40}Ca and ^{58}Ni.

---

[1] B. W. Ridley, T. H. Braid, T. W. Conlon, Bull. Amer. Phys. Soc. 14 (1969) 1219.
[2] C. B. Fulmer and J. C. Hafele, Phys. Rev. C5 (1972) 1969.
[3] H. H. Chang, B. W. Ridley, Univ. of Colo. Nuclear Physics Laboratory Technical Progress Report, (1971) 55.

Colo. vi. ^{40}Ca(α,α) and ^{58}Ni(α,α) at 82.0 and 85.6 MeV - H. H. Chang, B. W. Ridley, N. S. P. King (U. of Calif., Davis), and E. F. Gibson (Sacramento State College)

24,858

The α particles were accelerated to an energy of 82 MeV by the cyclotron of the Crocker Nuclear Laboratory. The elastic scattering data up to 166° on ^{40}Ca and ^{58}Ni were normalized to the optical

17-20

model predictions at small angles. The optical parameters were obtained from the 85.6 MeV data[1] on the same nuclei. Various optical model fits to each data set are displayed in Fig. A1-13. The solid lines represent typical fits of six-parameter Woods-Saxon potentials with $V_o \sim 125$ MeV. For the dashed line $V_o \sim 180$ MeV. Volume imaginary potentials were used in both cases.

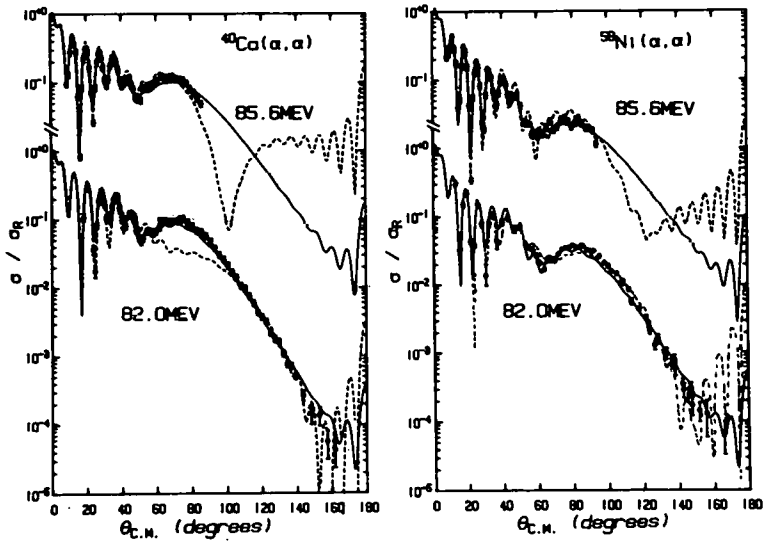

Fig. A1-13 Cross sections for the elastic scattering of α particles from ^{40}Ca and ^{58}Ni. The curves indicate cross sections generated from (a) six-parameter Woods-Saxon potentials given in Table A1-II (first four rows), solid line; (b) another optical parameter family with $V_o \sim 180.0$ MeV, dashed line, volume imaginary being used in each case.

Five-parameter searches were performed by fixing V at a number of different values. These searches were made on the 82.0 MeV data for each target. The results of the searches are presented in Fig. A1-14. For ^{40}Ca only a single family was found. Serious ambiguities were observed in the ^{58}Ni case. The difficulty encountered here is expected due to the larger size of ^{58}Ni.[2] A large portion of χ^2/N for $V_o \sim 130$ MeV comes from the small angle region where the cross sections showed a rapid oscillation. The optical model predictions give much larger magnitudes than the experimental cross sections. The angles subtended by the detector in these runs are only 0.5°, but the cross section minima still tend to be washed out. This difficulty is not observed when only a limited range of data was involved in the search as in the 85.6 MeV data shown in Fig. A1-13. The present data for ^{58}Ni did not resolve the ambiguities in the optical parameter family. Higher energy experiments on ^{58}Ni did indeed prove that the shallow family gave a much smaller χ^2/N than others. For this reason, we list the best fit optical parameters of this family for both targets in Table A1-II. Simultaneous fits to both targets at fixed energy using the same set of

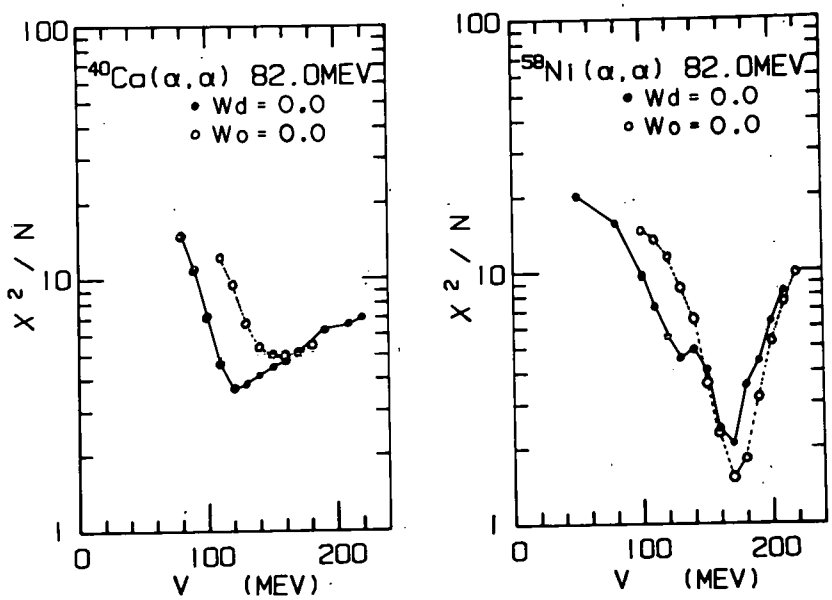

Fig. A1-14 χ^2/N vs V for 82.0 MeV α particle elastic scattering from ^{40}Ca and ^{58}Ni for potentials with either volume (solid line) or surface absorption (dashed line).

TABLE A1-II

Optical potential parameters for 82.0 and 85.6 MeV α particle scattering from ^{40}Ca and ^{58}Ni. The last four rows are the results of simultaneous fits to two sets of data using a single set of parameters. R_c=1.4 fm.

Target	E_{lab}	V	R_R	A_R	W_o	R_I	A_I	χ^2/N
^{40}Ca	82.0	123.6	1.276	.795	18.68	1.691	.588	3.7
^{40}Ca	85.6	125.6	1.249	.802	22.84	1.522	.820	3.8
^{58}Ni	82.0	130.7	1.220	.814	17.51	1.618	.510	4.5
^{58}Ni	85.6	125.1	1.260	.763	19.71	1.589	.596	2.1
^{40}Ca	82.0 & 85.6	128.0	1.239	.821	19.48	1.646	.663	4.4
^{58}Ni	82.0 & 85.6	122.3	1.264	.766	19.01	1.610	.550	6.5
^{40}Ca & ^{58}Ni	82.0	126.8	1.145	.883	37.94	1.106	1.188	11.6
^{40}Ca & ^{58}Ni	85.6	118.8	1.273	.739	29.63	1.359	.903	6.4

optical parameters were not very encouraging, as can be seen from a larger χ^2/N and large deviations from the best fit parameters listed in Table A1-II. The much wider angular range covered in the 82.0 MeV scattering data did not help to improve this situation. The difficulty encountered might be due to a special α scattering mechanism with these two nuclei. Data covering a wider range of targets could resolve this question. Development of an energy dependent set of optical potentials for ^{40}Ca and ^{58}Ni will be tried in the near future.

---

[1] T. W. Conlon, B. W. Ridley, T. H. Braid, Bull. Amer. Phys. Soc. 13 (1968) 650.

[2] D. A. Goldberg and S. M. Smith, Phys. Rev. Lett. 29 (1972) 500. D. A. Goldberg, S. M. Smith, H. G. Pugh, P. G. Roos, and N. S. Wall, Bull. Phys. Rev. C 7 (1973) 1938.

2. Gamma Ray Experiments and Beta Decay

a. The Decay of ^{36}K - M. J. Fritts

The delayed γ's from the positron decay of ^{36}K were studied following the $^{36}Ar(p,n)^{36}K$ reaction at 18 MeV. The measurements used a high pressure (4 atm) gas rabbit (see sect. II-C-4) filled with 99.94% ^{36}Ar, in the standard pneumatic shuttle system. Running times were typically 50 hours for 2 μa currents.

The data collected using the high pressure gas rabbit exhibit statistics almost a factor of 100 better than previous work. Several new levels in ^{36}Ar are found to be populated through the ^{36}K decay, indicating transitions up to 9220 keV. All previously reported transitions and the 4643 keV transition were observed.

To determine the half-life of the ^{36}K decay, the rabbit system was used to accumulate four sequential 1024 channel spectra at 320 msec intervals. The summed spectra from all four bins is shown in Fig. A2-1. The spectrum labeled "background" in the figure is

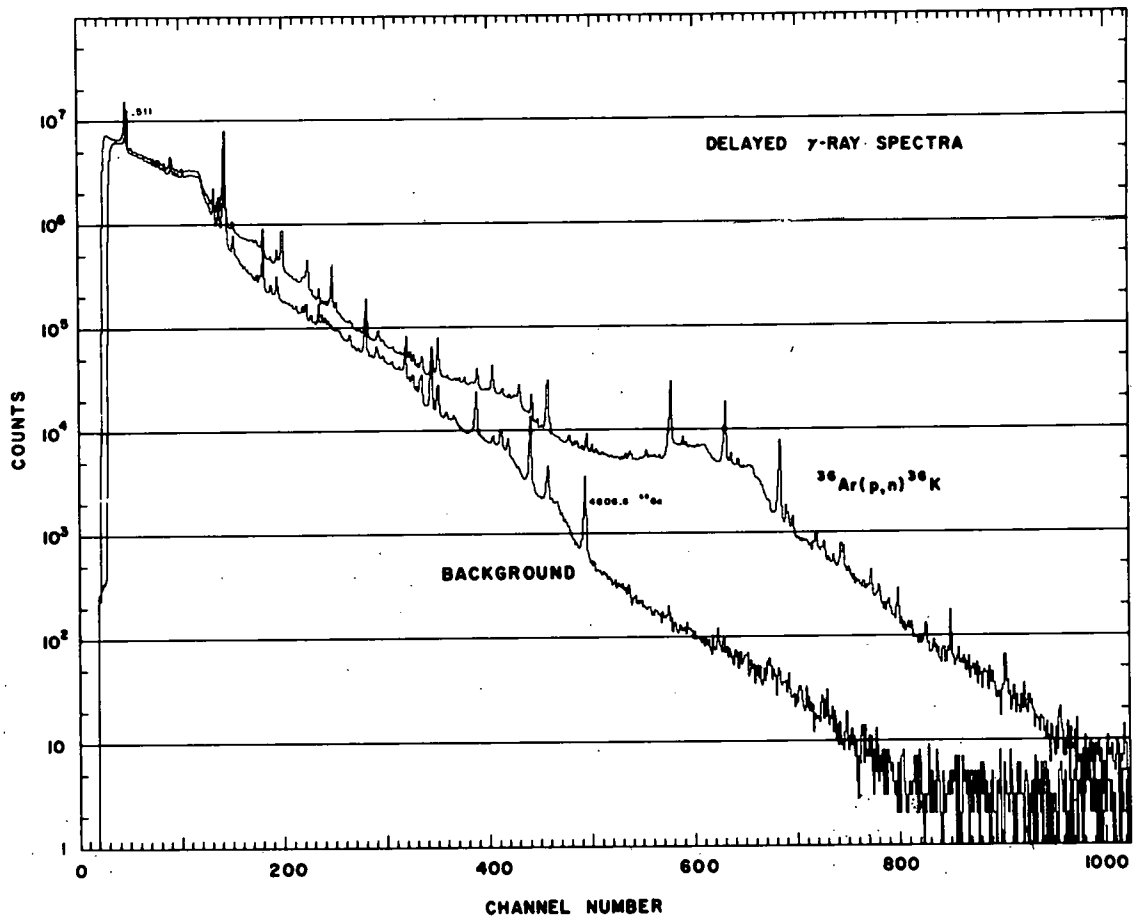

Fig. A2-1 Comparison of spectra obtained using a 4 atm gas rabbit filled with 99.94% ^{36}Ar to determine the decay scheme of ^{36}K subsequent to the $^{36}Ar(p,n)^{36}K$ reaction, and with ^{4}He to establish the background. There is a slight difference in the energy calibrations of the two spectra.

summed data collected using the same gas target and rabbit timing, but changing the gas from ^{36}Ar to ^{4}He and running for the same amount of integrated current. The difference in relative heights of contaminant peaks in the two spectra arises from the different half-lives of the contaminant nuclei involved. It can be seen from the figure that virtually all activity above 4807 MeV is due to ^{36}K.

Additional 4096 spectra were taken to facilitate a more precise energy determination of the previously unreported transitions. At present the data are being analyzed to extract energies, intensities and log ft values for the expanded decay scheme, as well as an improved value for the half-life of ^{36}K.

24,859

b. <u>(^{3}He,2n) Reaction Cross Sections on Several Light Nuclei</u> - C. E. Moss and C. S. Zaidins

In order to pursue the program of measuring β-delayed γ's from proton rich nuclei, one must have information on the magnitude of the (^{3}He,2n) and (^{3}He,3n) cross sections. This data is especially useful in deciding whether the delayed γ's can be detected without chemical and/or mass separation. Although the (^{3}He,2n) mechanism is well understood in the region of heavier nuclei where Coulomb effects are important in hindering charged particle emission from compound nuclei, there seems to be a scarcity of data below Z=20. We have measured the cross sections for the reactions $^{9}Be(^{3}He,2n)^{10}C$, $^{24}Mg(^{3}He,2n)^{25}Si$, and $^{27}Al(^{3}He,2n)^{28}P$. The preliminary results are shown in Fig. A2-2. In addition, we attempted to see the reaction $^{9}Be(^{3}He,3n)^{9}C$ at a lab energy of 41 MeV. All we could establish

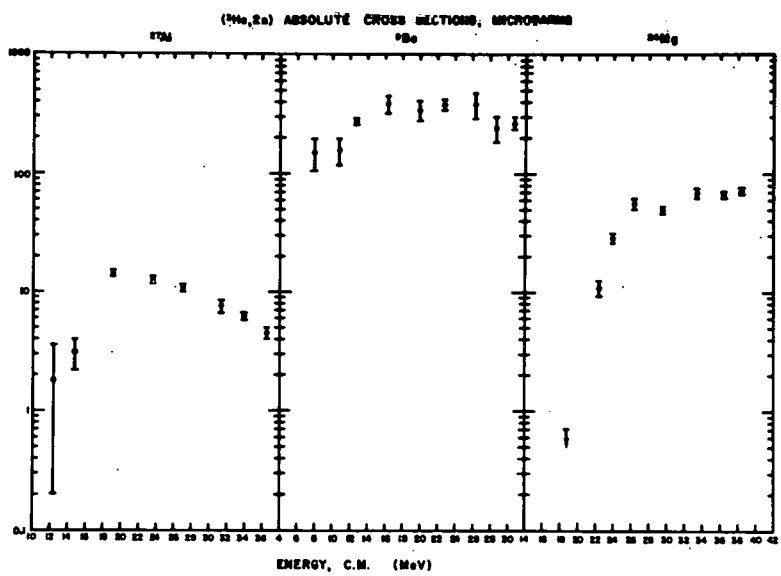

Fig. A2-2 The total cross section versus energy for the reactions $^{9}Be(^{3}He,2n)^{10}C$, $^{27}Al(^{3}He,2n)^{28}P$, and $^{24}Mg(^{3}He,2n)^{25}Si$. The ^{27}Al cross sections should be multiplied by 100. The cross section units are microbarns.

was that the (^{3}He,3n) cross section is at least two orders of magnitude smaller than the (^{3}He,2n) cross sections.

The technique used for the measurement of these cross sections involved many cycles of the University of Colorado pneumatic shuttle "fast rabbit" system. In the case of the ^{9}Be(^{3}He,2n)^{10}C and ^{27}Al(^{3}He,2n)^{28}P measurements, the standard γ-detector set-up was used and the delayed γ's from ^{10}C($T_{\frac{1}{2}}$=19.4 sec) and from ^{28}P($T_{\frac{1}{2}}$=0.27 sec) were detected. For the ^{24}Mg(^{3}He,2n)^{25}Si measurements, a new set-up was needed as the delayed protons, following the β-decay of ^{25}Si, were detected. When ^{25}Si decays, states in ^{25}Al are populated which decay to ^{24}Mg + p. The measurements were taken in the scattering chamber, and a plunger carrying the detector was removed from the beam during irradiation and returned to the target location for proton detection at the end of the irradiate cycle. The motion of the plunger was controlled by the standard rabbit electronics. In both the delayed γ and delayed proton measurements, four successive groups of counts were taken. This allowed a check for the appropriate half-life and a best fit to the counts that should appear in the first of the four groups C_1, with a counting time ΔT. The cross section can then be extracted by use of the formula

$$\sigma = K \cdot \frac{C_1}{Q} \cdot \frac{(1-e^{-\lambda T_2})}{(1-e^{-\lambda T_1})} \; \frac{e^{+\lambda (TT_2)}}{(1-e^{-\lambda \Delta T})}$$

where λ is the decay constant, T_2 is the total time per cycle, T_1 is the irradiation time, TT2 is the time delay from the end of the irradiation to the beginning of the count (the transit time for the rabbit or plunger), Q is the charge in microcoulomb accumulated during the entire run, and

$$K = \frac{\lambda \cdot T_i \cdot (3.2 \times 10^{-13})}{TM \cdot EFF}$$

where TM is the target thickness in atoms/cm^2 and EFF is the detection efficiency, including λ and proton branching ratios.

The ^{9}Be and ^{27}Al results plotted in Fig. A2-2 show the general rise that occurs for xn reactions from threshold to the (x+1)n threshold where a gradual decline occurs. The ^{24}Mg results have not yet peaked out at the energies available from our accelerator. We have not completed the final analysis of the results, nor do we understand the theoretical implications of these results as yet. We shall attempt to find an adequate model to fit all the data including the very low yield from the ^{27}Al(^{3}He,2n) reaction. Such efforts are currently underway.

c. The Level Structure of ^{88}Y and ^{90}Y from a Study of the $(\alpha,n\gamma)$ Reaction - R. L. Bunting and J. J. Kraushaar

The usefulness of the $(\alpha,n\gamma)$ reaction as a spectroscopic tool is enhanced by the fact that it proceeds primarily through the formation of a compound nucleus and hence tends to populate levels without regard to their spin, parity, or nucleon configuration. This of course is in contrast to the usual particle transfer reactions.

Study of these particular nuclei was begun several years ago and the preliminary results were reported in the Progress Report for 1970. Efforts were made this past year to obtain additional data to clarify several areas where questions remained. One of the major difficulties with the earlier data resulted from the use of a natural rubidium target for the $^{85}Rb(\alpha,n\gamma)^{88}Y$ reaction. Highly enriched $^{85}Rb_2CO_3$ was purchased and γ-ray data were obtained at an alpha particle energy of 12.2 MeV. The new data not only did not contain γ-rays from reactions on ^{87}Rb, but the quality of the data and the accuracy of the calibration procedures were considerably improved over the earlier results. The resulting spectrum is shown in Fig. A2-3. Because of some uncertainties in

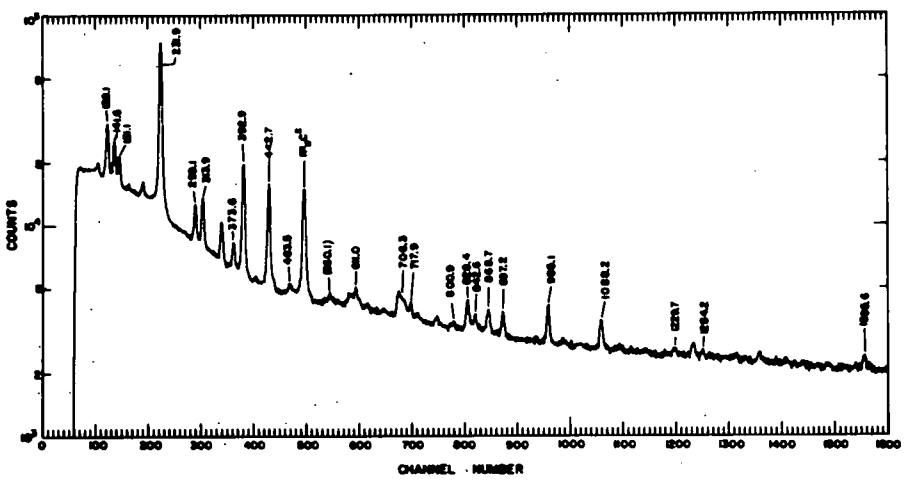

Fig. A2-3 γ-ray spectrum recorded at E_α=12.2 MeV for the $^{85}RbCO_3(\alpha,n\gamma)^{88}Y$ reaction.

the identification of several γ-rays, targets of both $^{85}RbCl$ and $^{87}RbCl$ were fabricated and data obtained at 12.2 MeV. In this fashion it was determined that a line at 141.6 keV should be assigned to both ^{88}Y and ^{90}Y and that the 151.1 keV line belonged to neither ^{88}Y nor ^{90}Y.

The γ-ray data on these two nuclei complemented a number of

recent charged particle reaction studies and permitted the construction of a rather complete level scheme up to 1700 keV for ^{88}Y and 1400 keV for ^{90}Y. Spin and parity assignments could not be made on the basis of the γ-ray data. Taken in combination with the other information available, however, a number of assignments could be made. The level schemes that summarize the present information on these two nuclei are shown in Figs. A2-4 and A2-5.

The work on these nuclei has now been completed and has been submitted for publication.

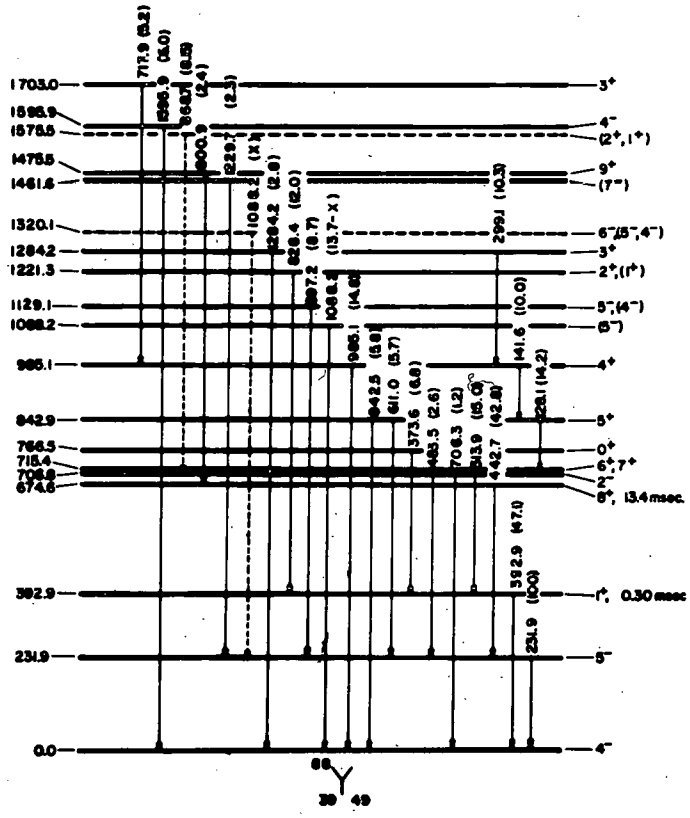

Fig. A2-4 Level structure of ^{88}Y from $^{85}Rb(\alpha,n\gamma)$. γ-ray intensities obtained from E_α=12.2 MeV data.

Fig. A2-5 Level structure of ^{90}Y from $^{87}Rb(\alpha,n\gamma)$.

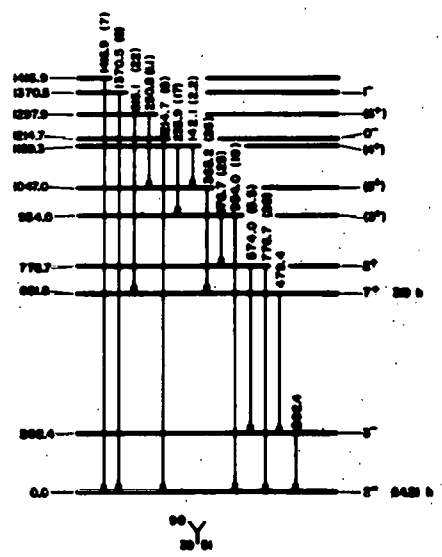

d. Ge(Li) Detector Efficiency Calibration Using Resonant Proton-Capture Gamma Rays - P. D. Ingalls and M. J. Fritts

In connection with experiments (see sects. a and c) measuring relative intensities of high-energy beta-delayed gamma rays following ^{20}Na and ^{36}K $\beta+$ decays, it was necessary to determine the relative efficiency for the 34-cm^3 Nuclear Diodes Ge(Li) detector. The 1318 keV and 1417 keV resonances in the reaction $^{23}Na(p,\gamma)^{24}Mg$ give equal-intensity gamma ray cascades (±2%)[1]

12.957 → 1.369 → 0
and 13.052 → 4.123 → 1.369,

and so measure the detection efficiency at 11.6 MeV and 8.9 MeV relative to that at low energies, where the energy dependence is well determined using radioactive sources. Evaporated NaCl targets of ~ 10 keV thickness on Ta backings were used, and the cyclotron was tuned to energies ~ 5 keV above resonance. Gamma rays were observed at 55° with respect to the beam, where the dominant anisotropy vanishes. Apart from small corrections (~ 2%) for absorption in the Ta backings, the counting rate ratios give the relative efficiencies exactly as needed for the $\beta+$ decay experiments, because the same collimator, attenuators, and geometry were used in the present experiments.

The help of C. E. Moss in a preliminary experiment is appreciated.

---

[1] B. P. Singh and H. C. Evans, Nucl. Instr. and Meth. 97 (1971) 475.

e. Sodium-20 Beta Decay - P. D. Ingalls

The positron decay of ^{20}Na to ^{20}Ne is of interest for several important questions (including the comparison of mirror $\beta+$ decay ft values, the CVC theory of weak interactions, the comparison of analog M1-gamma and Gamow-Teller beta decays and isospin mixing of nuclear states), as well as for testing model wave functions. Last year's preliminary data in the search for high-energy beta-delayed ^{20}Ne gamma rays following the $^{20}Ne(p,n)^{20}Na$ production reaction have been considerably improved. The final gamma-ray spectrum contains approximately 10 times the number of counts of the recent Texas A & M study.[1] Only two high energy transitions were strong enough for meaningful half-life measurements, and these were in agreement with the half-life of the well known strong 1.63 MeV transition. Weaker high-energy lines were also observed, and it was checked that they are not present in the beam-associated background during empty-target runs. An 8.65 MeV transition (previously observed[1]) arises from the M1 gamma decay of the 10.28 MeV, T=1 state, in significant competition with its isospin-forbidden α-decay. A new 11.25 MeV transition of comparable intensity indicates a very fast beta decay (log ft ≈ 3.8) to a known 1^+ state at that energy. This appears to to be the highest energy beta-delayed gamma ray known.

---

[1] D. F. Torgerson, K. Wien, Y. Fares, N. S. Oakey, R. D. Macfarlane, and W. A. Lanford, Phys. Rev. C 8 (1973) 161.

f. The $^{133}Cs(\alpha,n\gamma)$ Reaction - R. L. Bunting and J. J. Kraushaar

In the course of compiling the nuclear data currently available on mass number 136, it became evident that there was essentially no level structure information available on ^{136}La. The only levels known were at 100±5 keV and about ~170 keV from the studies of V. T. Gritsyna et al.[1]) The 170 keV state is thought to be a 110 μsec isomer and decays to the 100 keV state by an M2 transition.

We have endeavored to obtain much more complete level structure information for ^{136}La by observing the γ-rays following the $^{133}Cs(\alpha,n)$ reaction. Figure A2-6 shows the γ-ray spectra observed at bombarding energies of 12.4, 14.2, and 17.2 MeV. The data at 12.4, and to some

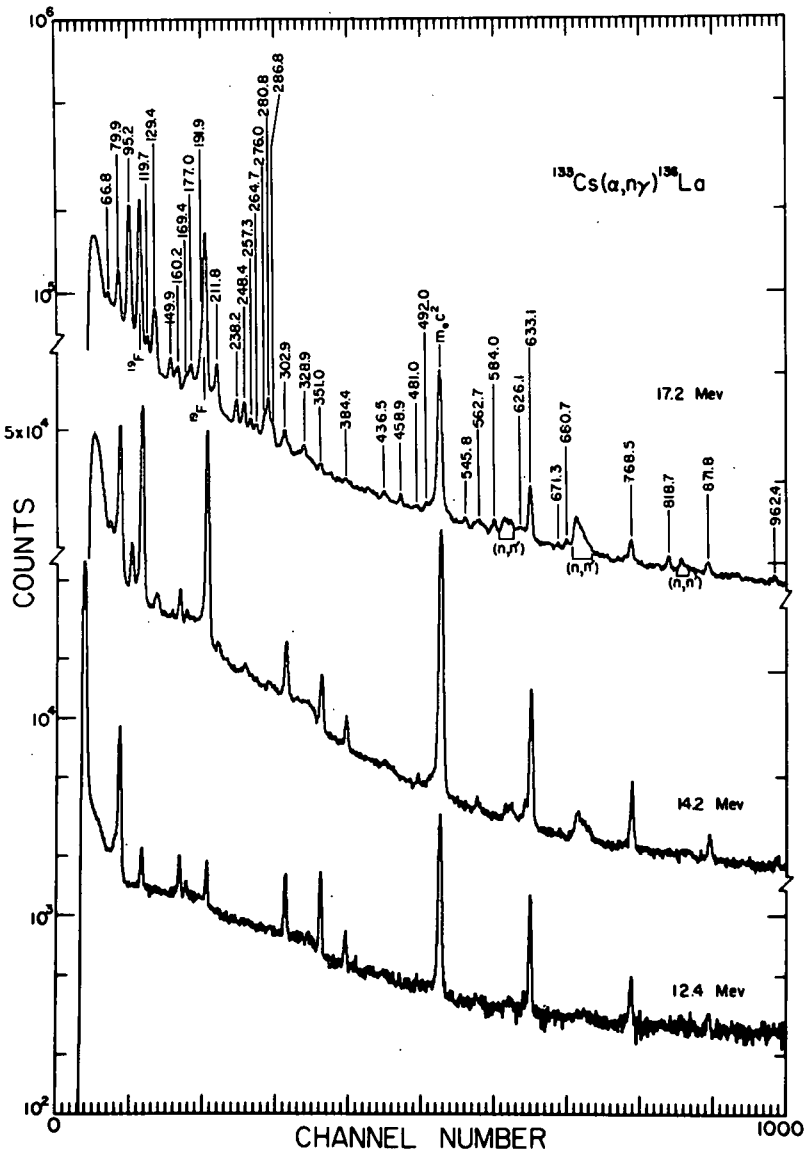

Fig. A2-6 Gamma-ray spectra resulting from alpha particle bombardment of ^{133}Cs at 12.4, 14.2, and 17.2 MeV.

extent 14.2 MeV, are dominated by γ-rays from Coulomb excitation of ^{133}Cs. Lines that are definitely in this category can be seen at 79.9, 160.2, 302.9, 384.4, 633.1, 785.5, and 871.8 keV. It is most likely also that the lines at 264.7 and 818.7 keV are transitions in ^{135}La and ^{136}Ba respectively. The remaining lines are, with one or two exceptions, from the (α,nγ) reaction. The strong line at 95.2 keV is no doubt from the first excited state of ^{136}La and 66.8 keV from the 110 μsec isomer. Efforts are being made at the present time to accommodate the other transitions into a level scheme. To aid in this effort, the $^{136}Ba(^{3}He,t)^{136}La$ and the $^{135}Ba(^{3}He,d)^{136}La$ reactions will be studied using the new energy loss spectrometer.

---

[1] V. T. Gritsyna, A. P. Klyucharev, and V. V. Remaev, J. Nucl. Phys. (U.S.S.R.) 3 (1966) 993.

(24,861) g. The Level Structure of ^{106}Ag by the $^{103}Rh(\alpha,n\gamma)$ Reaction - R. L. Bunting, S. Chinn, J. J. Kraushaar

28-7

The level structure of ^{106}Ag was completely unknown prior to this investigation. A variety of reactions have been used here to obtain information on this nucleus. The results of the $^{107}Ag(p,d)^{106}Ag$ studies are discussed elsewhere in this report. The γ-ray spectra resulting from a 12.4, 14.2, and 17.2 MeV alpha bombardment of a ^{103}Rh target are shown in fig. A2-7. There are only two lines that can be clearly ascribed to Coulomb excitation of ^{103}Rh, namely the lines at 294.5 and 357.0 keV and these were used in addition to the γ-rays from ^{56}Co and ^{137}Cs radioactive sources in obtaining the energy calibration.

It is difficult to use only γ-ray data in constructing an energy level diagram. The only existing information on ^{106}Ag is that the 8.3 d isomer (6+) is at around 300 keV. A number of decay scheme studies of this 8.3 d radioactivity have observed a 110 keV transition and assigned it to the levels of ^{106}Pd. It is believed that the strong 110 keV transition in fig. A2-7 is indeed the same line as the one seen in the radioactivity and represents a level at 110.3 keV in ^{106}Ag.

A number of possible levels are suggested from the γ-ray data and seven of these are consistent with the energies derived from the (p,d) experiment. It is clear that there are many more levels seen in the (α,nγ) experiment than in the rather selective (p,d) reaction. A detailed level scheme is being worked out at the present time and should be completed shortly.

The $^{106}Pd(^{3}He,t)^{106}Ag$ reaction was also studied using the new energy-loss spectrograph. Unfortunately, the thickness of the target was so small that it was difficult to obtain good quality data. The

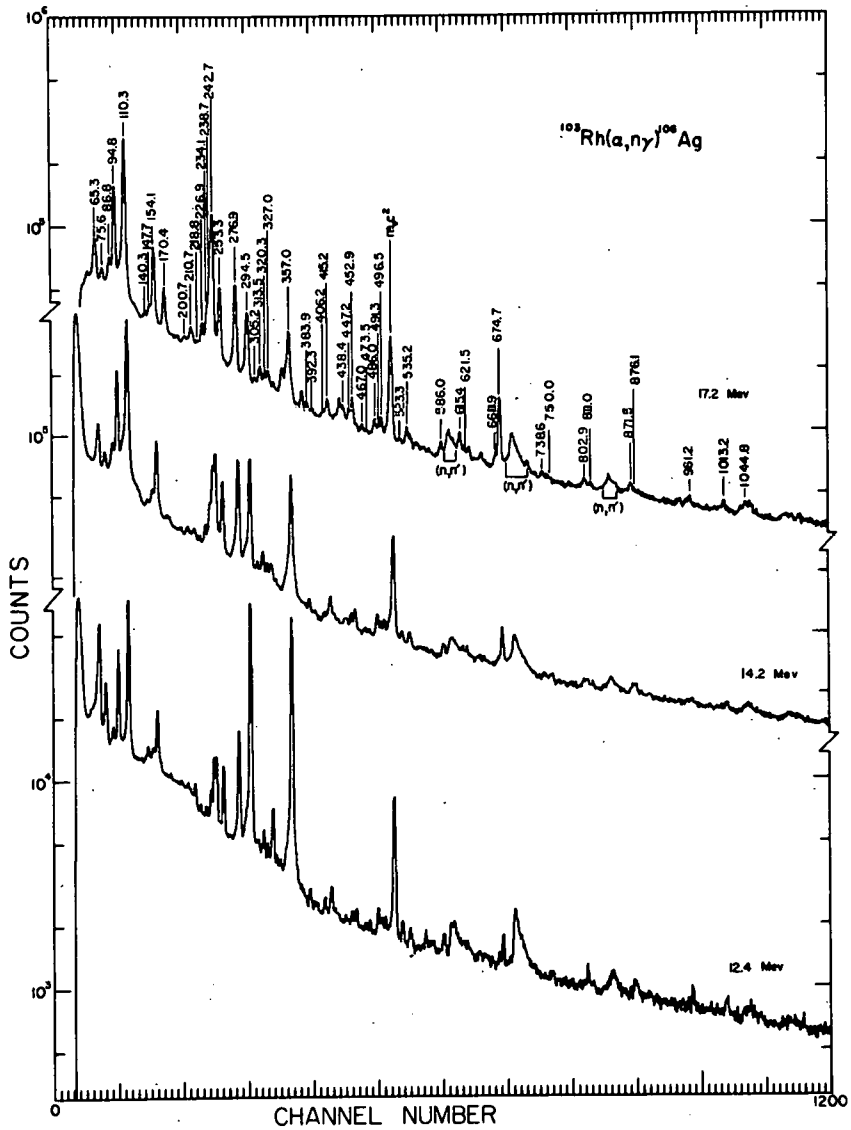

Fig. A2-7 Gamma-ray spectra following the ^{103}Rh(α,n) reaction at 17.2, 14.2, and 12.4 MeV bombarding energies. A 25 cc Ge(Li) detector at 90° to the beam was used in obtaining the data.

results so far are compatible with the (p,d) and (α,nγ) reactions. The (^{3}He,d) reaction will also be utilized in the next few weeks to obtain further information on the ^{106}Ag level structure.

h. Search for Delayed Gamma Rays from the $^{91}Zr(p,\alpha)^{88}Y$ Reaction - C. D. Goodman, R. J. Peterson, and R. L. Bunting

It has been suggested that a low spin state of ^{88}Y is unresolvably close to the known high spin state near 706 keV.[1] A study of the $^{85}Rb(\alpha,n\gamma)^{88}Y$ reaction[2] (elsewhere in this report) did not detect such a gamma ray, implying that if it exists it must be very near indeed to the known state. Such a low spin state has a characteristic signature, in that it must decay to the 1^+ state at 393 keV, which has a half-life of 0.3 msec. The expected state has largely a hole configuration, and we might expect it to be populated by the $^{91}Zr(p,\alpha)$ reaction.

A 22.8 MeV proton beam was used to bombard a 0.8 mg/cm^2 target of enriched ^{91}Zr. A detector just thick enough to stop the expected alpha particles was used to detect the correct region in the ^{88}Y spectrum. Upon sensing a valid α event in the 706 keV region, the cyclotron was pulsed off, by the remote RF control used for the rabbit system, and a multiscaled gamma ray spectrum was taken with a Ge(Li) counter. The multiscaling rate was 0.1 or 0.2 msec per bin. We expect to see the 393 keV gamma decaying with a half-life of 0.3 msec. We have determined that the proton beam does decay within 0.1 msec of the circuit being triggered.

No clear 393 keV peak was seen in the gamma spectrum. For 10^4 alpha gates in a twelve-hour run, we expected 4 counts in the 393 keV peak, and because of the background can only place an upper limit of 10 counts. The reaction count rate is already as large as possible without degrading the resolution of the alpha spectrum to the point of including in the gate some counts from the 766 keV state (0^+), known to decay by the delayed gamma. Several reorganizations of the beam line have already been tried, which have dropped the background in the gamma spectrum by an appreciable amount. It appears that much longer runs are required for this experiment.

---

[1] F. Gabbard, G. Chenevert, K. K. Sekharan, Phys. Rev. C6 (1972) 2167.

[2] R. L. Bunting and J. J. Kraushaar, this report, II-A-2-c.

24,862

i. Total Cross Sections and Excitation Functions for ^1H, ^2H, ^3He, and ^4He on Targets of Natural Mg, Al, and Si - C. S. Zaidins in collaboration with D. J. Frantsvog, R. L. Wilson, and A. R. Kunselman (Univ. of Wyoming)

30-2

Thin targets of natural Mg, Al, and Si were irradiated with ^1H, ^2H, ^3He, and ^4He beams of various energies. The rabbit system was used to transport the irradiated targets from the target box to a

well shielded counting area. A Ge(Li) detector and the ND 50/50 were used to gather and store the spectra. By use of the decay schemes and the half lives of the isotopes involved and by employing the beam current information provided by use of the Faraday cup, it was possible to calculate the total cross sections and excitation functions for some of the reactions which occur.

The collection of data has been completed and the analysis of the data is well underway. The target isotopes and the beam energies used in this experiment are listed in Tables A2-I and A2-II.

TABLE A2-I

Beam	Energy (MeV)
protons	14.5, 18.8, 22.8, 27
deuterons	8.7, 14, 18
^{3}He	18.9, 20.9, 25.4, 37.5, 41
^{4}He	20, 24.7, 28, 33, 37

TABLE A2-II

Isotopes present in natural Mg, Al, and Si	
Mg-24	Si-28
Mg-25	Si-29
Mg-26	Si-30
Al-27	

Fig. A2-8 shows comparisons of preliminary results obtained and measurements by J. F. Lamb[1] et al. The agreement is good.

Results to date indicate that the Faraday cup which was constructed to overcome the non-reproducibility of beam current measurements by flag 2 is functioning well and giving consistent results.

[1] J. F. Lamb, D. M. Lee, and S. S. Markowitz, Lawrence Radiation Laboratory, Nuclear Chemistry Annual Report (1968).

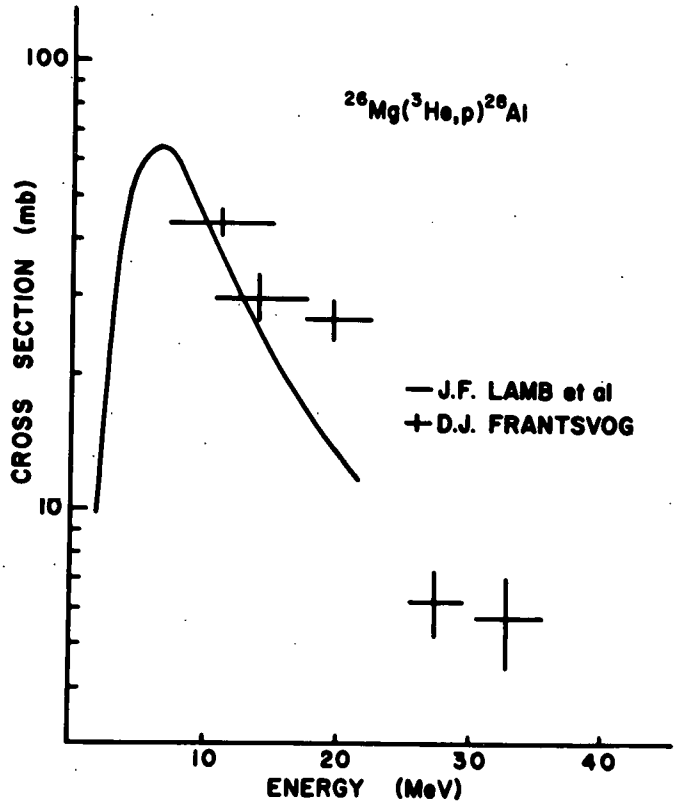

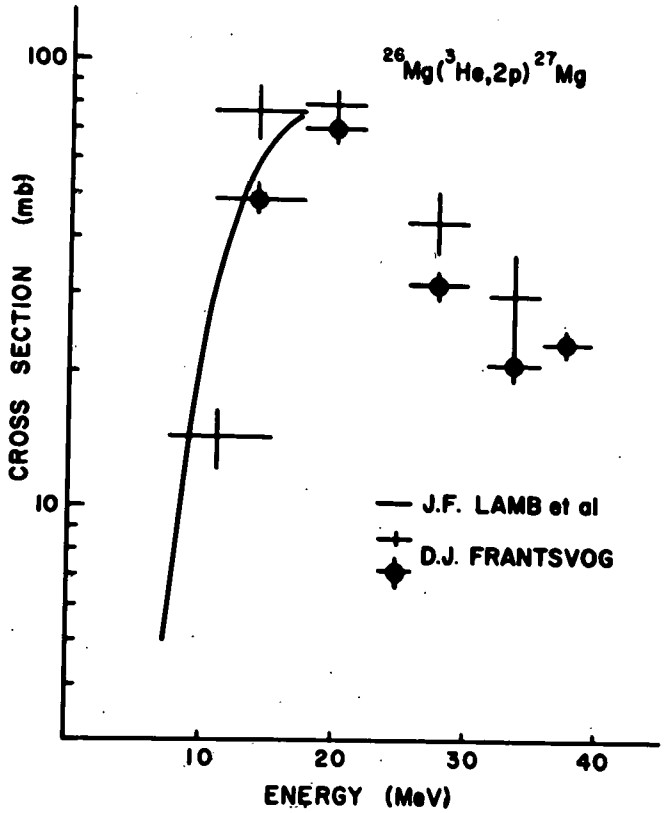

Fig. A2-8 Excitation functions for the reactions $^{26}Mg(^{3}He,p)^{28}Al$ and $^{26}Mg(^{3}He,2p)^{27}Mg$ as reported by J. F. Lamb et al. and some cross sections measured in the present work.

24,863

j. Measurements of Gamma Ray Branching Ratios in ^{28}Al - C. E. Moss

The branching ratios were determined by means of the $^{27}Al(d,p\gamma)^{28}Al$ reaction. The protons were detected in a ΔE-E telescope at 90°. The γ-rays were detected in a 22 cm.^{3} Ge-Li detector, also at 90°, but perpendicular to the reaction plane. The coincident events were stored on magnetic tape using a PDP-9 computer. A gamma ray spectrum was generated for each proton group corresponding to a level in ^{28}Al by playing back the tape with appropriate windows. From these spectra the branching ratios shown in Fig. A2-9 were determined.

33-4

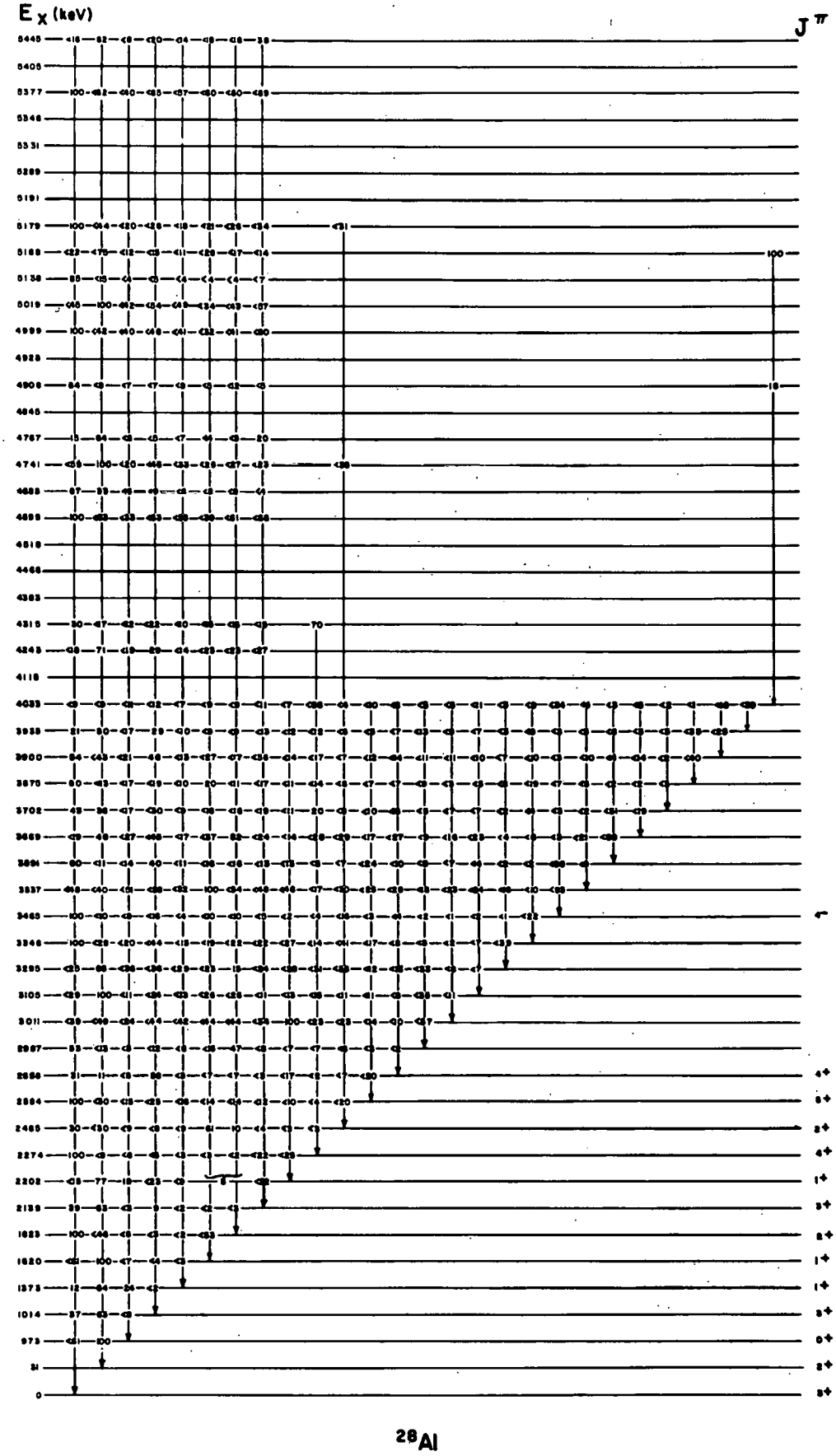

Fig. A2-9 Summary of gamma-ray branching ratios determined in present study.

24,864

3. Neutron Time-of-Flight Experiments

a. The (p,n) Reaction on High Z Elements - S. D. Schery, H. Fielding, C. D. Goodman, D. A. Lind, and C. D. Zafiratos

Measurements of the angular distributions of the (p,n) reaction neutrons on ^{197}Au, $^{206,207,208}Pb$, ^{209}Bi, and ^{232}Th were made at E_p=25.8 MeV using the rotating beam time-of-flight system. A typical spectrum is shown in Fig. A3-1. In general, only the IAS state was prominent above the distribution of evaporation neutrons.

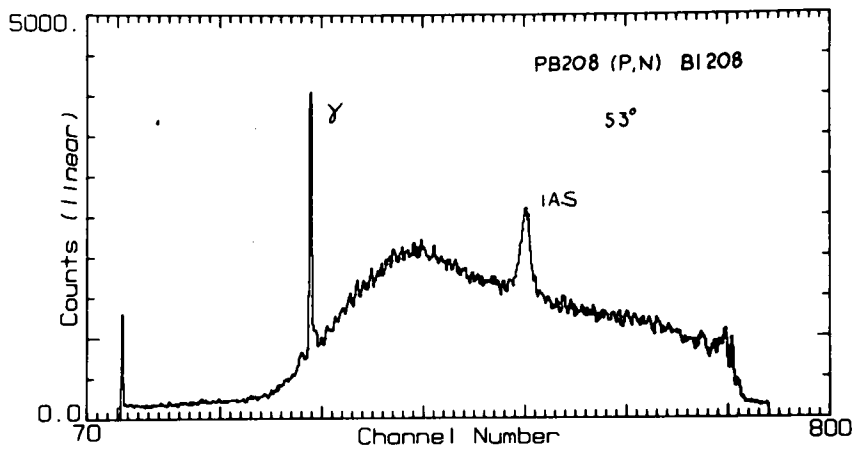

Fig. A3-1 Time-of-flight spectrum of neutrons for ^{208}Pb + p at E_p=25.8 MeV. The width and strength of the analog state is typical of heavy elements.

A macroscopic optical model analysis of the data was used. The Becchetti-Greenlees[1] global parameters were used as a starting point. The procedure suggested by Carlson[2] to generate a set self-consistent within the Lane model did not yield suitable neutron optical model fits so a recent set of potentials derived by Fu and Perey[3] was used for neutrons as the starting point in the DWBA calculations to generate the distorted waves. Because it was necessary to reduce the variable set over which searches were made for a variety of reasons the following set was used:

V_{IV}, R_{RV}, a_{RV}	searched
V_{IS}=0	fixed
W_{IS}/V_{IS}=0.5	fixed
R_{IS}=1.32, a_{IS}=0.66	fixed

Generally with these heavy elements the effect of the imaginary I-spin dependent potential on the calculated (p,n) cross section was small, in contrast to the experience of Carlson[2]. A search on ^{197}Au, ^{208}Pb and ^{232}Th yielded a best fit form factor with:

V_{IV}=20.2 MeV

R_{RV}=1.1 a_{RV}=1.0

V_{IS}=0

W_{IS}=10.1

R_{IS}=1.32 a_{IS}=0.66

There is a slight improvement in shape of the calculated angular distribution but the major improvement is in the strength relative to that obtained utilizing Becchetti-Greenlees parameters. Fig. A3-2 shows the distributions and the resultant best fits. The important conclusion is that the fits are insensitive to the imaginary part of the potential contrary to the experience with lower mass nuclei.

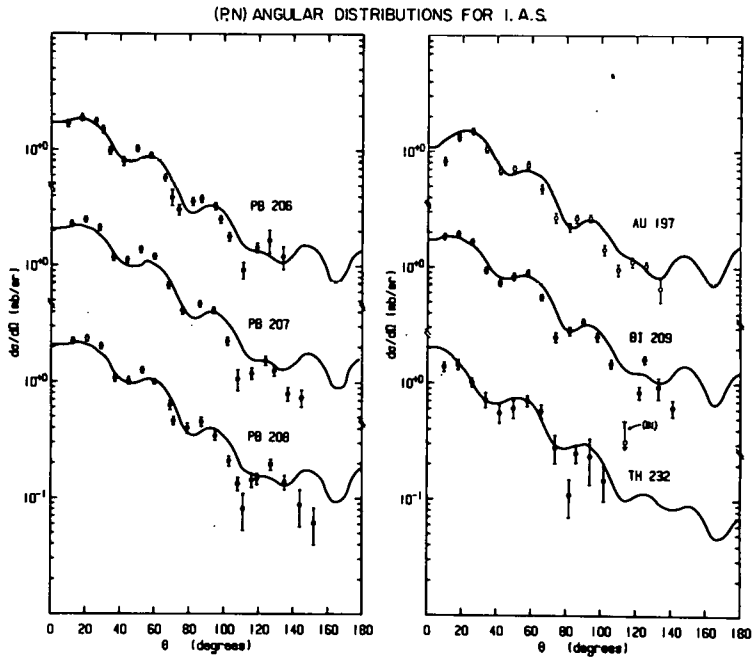

Fig. A3-2 Comparisons of calculations with (p,n) data using the improved form factor derived by a search starting with Becchetti-Greenlees proton parameters. All data points are for 25.8 MeV energy.

The initial optical potentials were not consistent with the Lane model for the $\vec{\tau} \cdot \vec{T}$ interaction but an attempt was made to generate neutron scattering potentials using the best values of the I-spin term starting with the known proton potentials. Fig. A3-3 shows the results. The data points are experimental results. The solid curve A resulted from applying the Lane model to the Becchetti-Greenlees values using the best-fit form factor. Curve B was generated by an energy only (no isospin) correction to the Becchetti-Greenlees parameters. Since the (p,n) scattering was

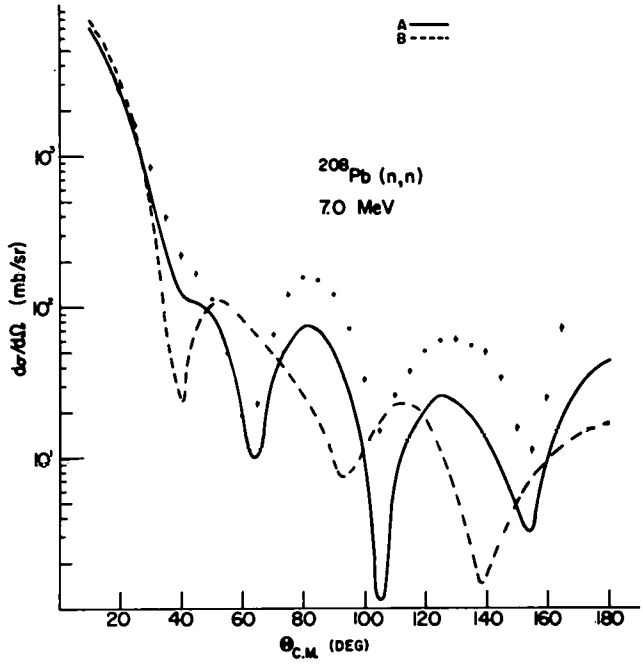

Fig. A3-3 Comparisons of optical model predictions with data for neutron elastic scattering. Curve A was generated from B-G proton parameters and a best fit I-spin term using the Lane model. Curve B results from turning the I-spin term off but correcting for energy.

insensitive to the imaginary part of the form factor, an attempt was made to fit (p,p), (p,n), and (n,n) data using the Lane prescription by varying the term W_{IS}. For this purpose the only essential change from the best fit parameters tabulated earlier is that W_{IS} is increased from 10.1 to 17 MeV. Fig. A3-4 shows the marked improvement in the (n,n) fit.

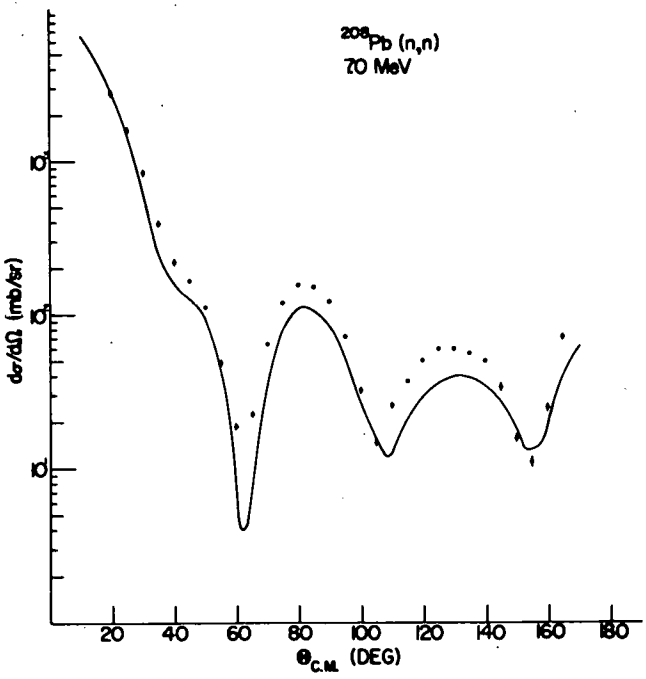

Fig. A3-4 The curve in this case was generated by changing W_{IS} from 10.1 to 17 MeV with B-G parameters leaving the other parameters unchanged.

[1] F. D. Becchetti, Jr. and G. W. Greenlees, Phys. Rev. 182 (1969) 1190.
[2] J. D. Carlson et al., Phys. Rev. Lett. 30 (1973) 99.
[3] C. Y. Fu and F. G. Perey, Oak Ridge National Laboratory Report, ORNL-4765 (1972) p. 30.

b. Widths of Analog States in Heavy Elements - H. Fielding, S. D. Schery, C. D. Goodman, D. A. Lind, and C. D. Zafiratos

The discrepancy in the widths of isobaric analog states (IAS) in heavy nuclei as obtained from (p,$\widetilde{n}$p) and (p,p') resonance experiments led to measurements of the (p,n) reaction directly.[1] The study of Au, Pb, Bi, and Th with the (p,n) reaction by Schery for his thesis yielded information on these discrepancies in the width of IAS states as well as on the cross section discrepancies.

Measurements were made at 25.8 MeV with a flight path of 9.5 meters. Targets of ^{12}C, as well as of the heavy elements, were fabricated to yield energy losses of 20-30 keV. Since the Q-value of $^{12}C(p,n)^{12}N$ is comparable to that for ^{208}Pb it could be used to obtain an accurate Q-value determination as well as IAS state width measurement. Fig. A3-5 shows a composite of $^{12}C(p,n)^{12}N$ and $^{207}Pb(p,n)$ spectra. The ^{12}C line was used as the instrumental line width needed in the unfolding procedure to obtain the true IAS state width.

Fig. A3-6 shows the results of an analysis of line width as a function of the background. At the energy used, the IAS state lies near the peak of the evaporation neutron spectrum. As a larger range of the adjacent background is used to fit the background the extracted width of the peak changes consistently. (C.P.D. represents chi square per degree of freedom.) Serious errors in width will result if the background is not properly determined. Table A3-I summarizes the results on Q-values and widths for the cases observed. In each case several independent measurements were made. A discussion of the separate measurements and comments on the total reaction cross sections is contained in a paper submitted for publication.[2]

[1] G. M. Crawley, P. S. Miller, A. Balonsky, T. Amos, and R. Doering, Phys. Rev. C 6 (1972) 1890.
[2] H. Fielding, S. D. Schery, D. A. Lind, C. D. Zafiratos, and C. D. Goodman, submitted to Phys. Rev. (1973).

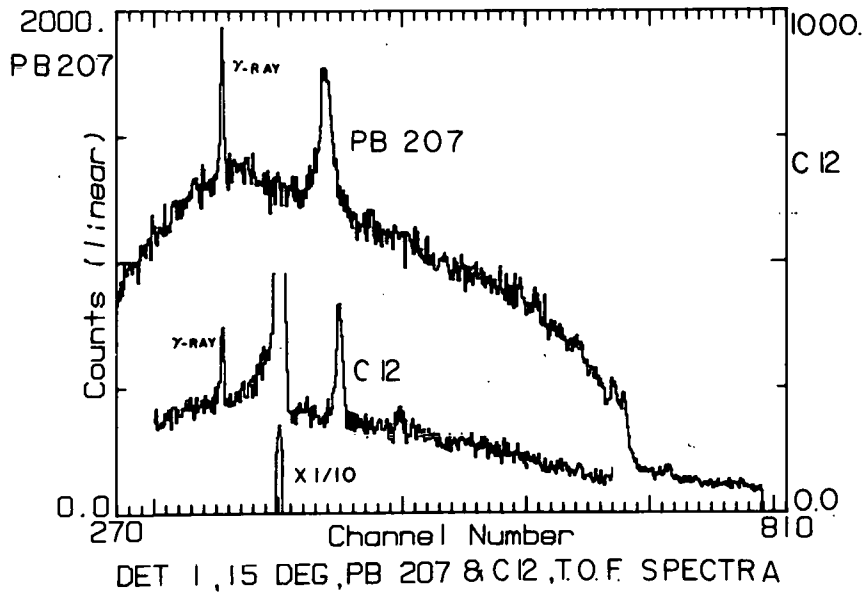

Fig. A3-5 Composite of time-of-flight spectra for the targets ^{207}Pb and ^{12}C. The ^{12}N ground state is below and slightly to the right of the analog peak.

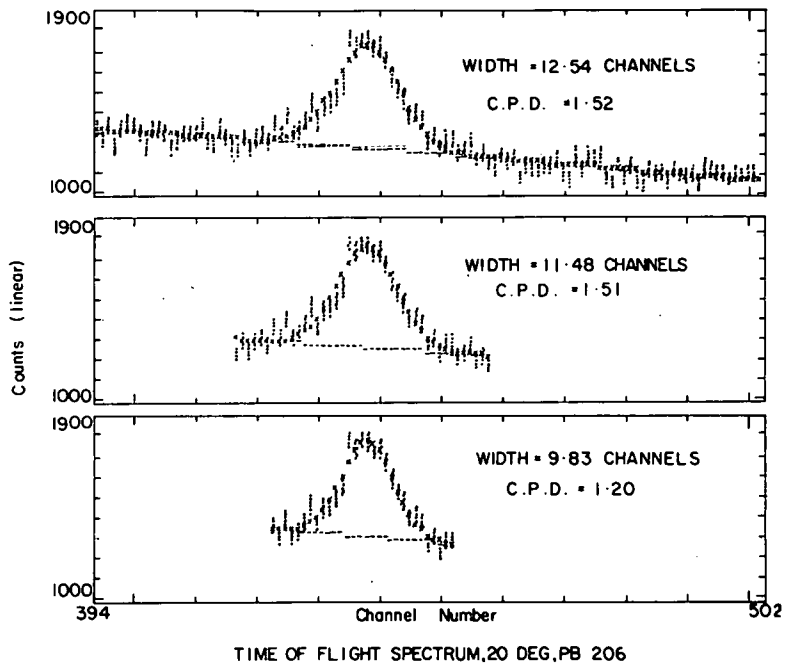

Fig. A3-6 Effect of background on the width of the analog peak for the target ^{206}Pb. In each case the same data points are fit with a Gaussian line shape but with a different width background. C.P.D. is chi squared per degree of freedom (χ^2/ν) of the resulting agreement with data.

TABLE A3-I

Widths and Q-values for isobaric analog states.

Isotope (Parent)	Q-value (MeV)			Width (keV)		
	(p,n)	(p,n)[a]	(p,n$\bar{p}$)[a]	(p,n)	(p,n)[a]	(p,n$\bar{p}$)[a]
^{197}Au	-18.555±.020			158±35		
^{206}Pb	-18.944±.020	-18.911±.034	-18.899±.024	220±25	196±26	230±38
^{207}Pb	-18.919±.020	-18.888±.034	-18.875±.028	236±25	203±32	540
^{208}Pb	-18.850±.020	-18.831±.034	-18.816±.013	277±35	202±34	317±24
^{209}Bi	-19.030±.025	-19.011±.021	-18.991±.012	299±35	151±34	327±31
^{232}Th	-19.846±.025			315±30		

[a] Results in these columns taken from Ref. 1.

c. Neutron-Proton Density Distributions - S. D. Schery, D. A. Lind, C. D. Zafiratos

An analysis of the (p,n) scattering by ^{208}Pb may be carried out by a microscopic analysis in which neutron and proton density distributions, $\rho_p(r)$ and $\rho_n(r)$, are folded with an appropriate nucleon-nucleon interaction V_i. The coefficient of the $\vec{\tau} \cdot \vec{T}$ term in the optical potential is

$$U_1(\vec{r}) = \frac{A}{2T_3} \int V_\beta(\vec{r} - \vec{r}')[\rho_n(\vec{r}') - \rho_p(\vec{r}')]\, d^3r'$$

where V_β is the I-spin dependent part of the two-body interaction. Greenlees et al.[1] deduced this relation and applied it to proton and neutron optical potentials to deduce the value of ρ_n; given ρ_p as measured by electron scattering. Since the (p,n) reaction is much more sensitive than elastic scattering to the shape and strength of $U_1(\vec{r})$, it should provide a means to determine ρ_n also.

Data for the ^{208}Pb(p,n)^{208}Bi reaction were used with the assumption of a Woods-Saxon distribution for $\rho_n(r)$ and $\rho_p(r)$. We used the proton distribution parameters summarized by Uberall[2] and Gaussian form for $V_\beta(r)$

$$V_\beta(r) = 7.51e^{-\left(\frac{r}{1.69}\right)^2} \text{ MeV}$$

with r given in Fermis. A search for best fit in terms of the parameters R_r and a_n, the radius and diffuseness respectively, yielded the fit shown in Fig. A3-7 with $R_rA^{1/3}$=7.02 fm and a_n=0.44 fm. The condition

$$\int[\rho_n(r) - \rho_p(r)]\, d^3r = N-Z$$ was maintained.

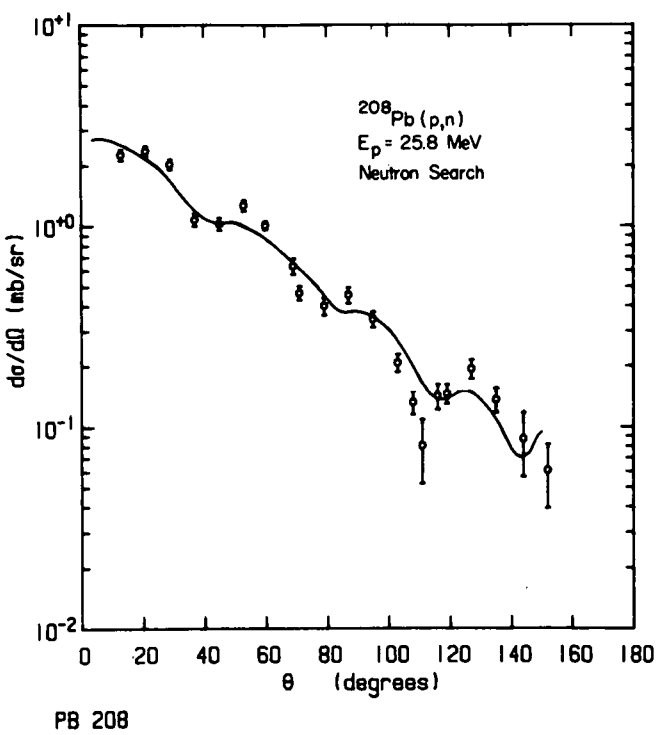

Fig. A3-7 Comparison of calculated distribution for ^{208}Pb(p,n) using a_n=0.44 fm and $R_nA^{1/3}$=7.02 fm with experimental data after a χ^2 best fit search.

The value of the ratio of the RMS radii of neutrons to protons was $\langle r_n^2\rangle^{\frac{1}{2}}/\langle r_p^2\rangle^{\frac{1}{2}} = 1.07\pm0.03$. This value agrees within the limits of error to values deduced from (p,p) optical potentials, (α,α) scattering, and with Hartree-Fock calculations. Pion scattering results consistently yield values near 1.00.

---

[1] G. W. Greenlees et al., Phys. Rev. C 1 (1970) 1145.
[2] H. Uberall, Electron Scattering from Complex Nuclei (Academic Press, New York, 1971).

24,865

d. Comparison of (p,n) Reaction Cross Section with Activity Measurement for ^{13}C - D. A. Lind, R. J. Peterson, and H. Fielding

Measurement of the $^{13}C(\pi^+,\pi^\circ)^{13}N$ cross section by the measurement of ^{13}N activity has led to a serious discrepancy with theoretical predictions. As a function of pion energy, between 100 and 350 MeV, the cross section increased slightly and is significantly larger than any reasonable theoretical estimate. A discussion of this point at the July, 1973, LAMPF Meson Summer School led to the suggestion by E. Rost that the equivalent charge exchange reaction, $^{13}C(p,n)^{13}N$ to the ground state, should be compared with ^{13}N activity produced at the same time.

A target of ^{13}C was prepared by charring in an argon atmosphere fructose having 80 atomic percent ^{13}C. The resultant hard carbon deposit was ground and deposited in an alcohol slurry on a 0.8 mg/cm^2 ^{58}Ni backing and then bonded with a small amount of polystyrene. The resultant target was 6.5 mg/cm^2 average density. A similar target of normal fructose was used as a comparison. The reaction was studied for E_p=23 MeV and a 10 M flight path. Fig. A3-8 shows the neutron spectrum and Fig. A3-9 the relative angular distribution. The analysis of the ^{13}N activity is shown in Fig. A3-10.

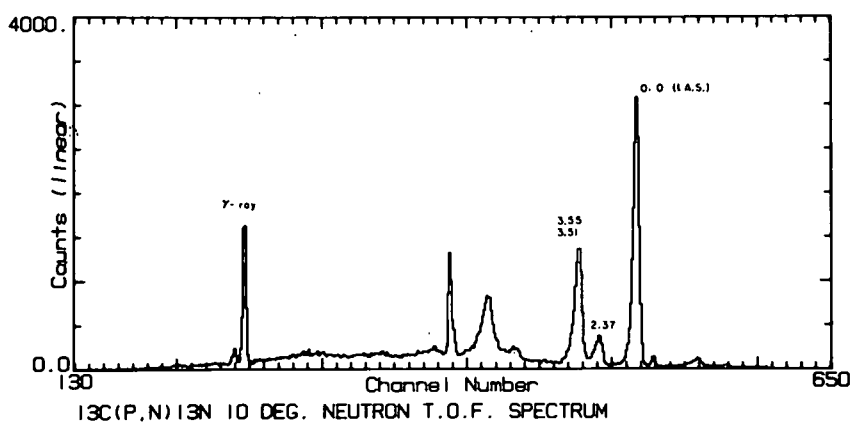

Fig. A3-8 $^{13}C(p,n)^{13}N$ time-of-flight neutron spectrum for E_p=23 MeV.

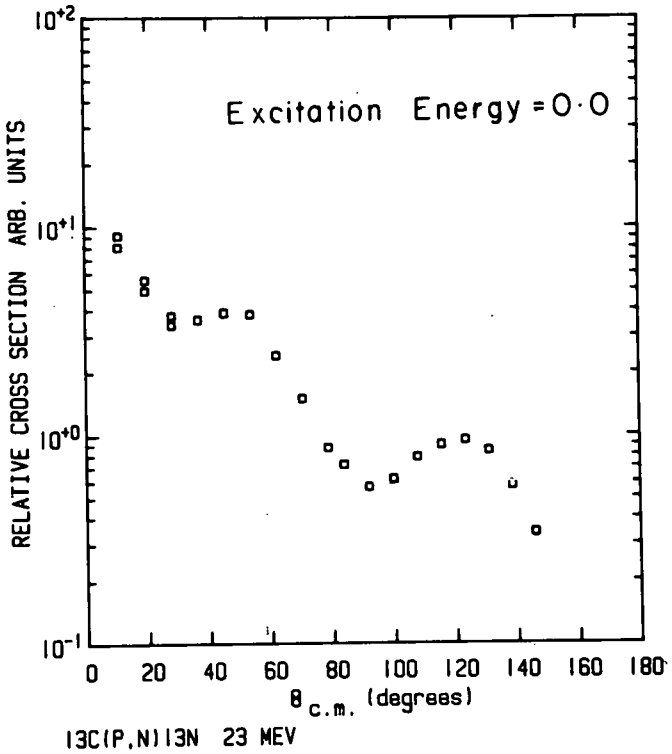

Fig. A3-9 The relative angular distribution observed for the $^{13}C(p,n)^{13}N$ (IAS) at E_p=23 MeV.

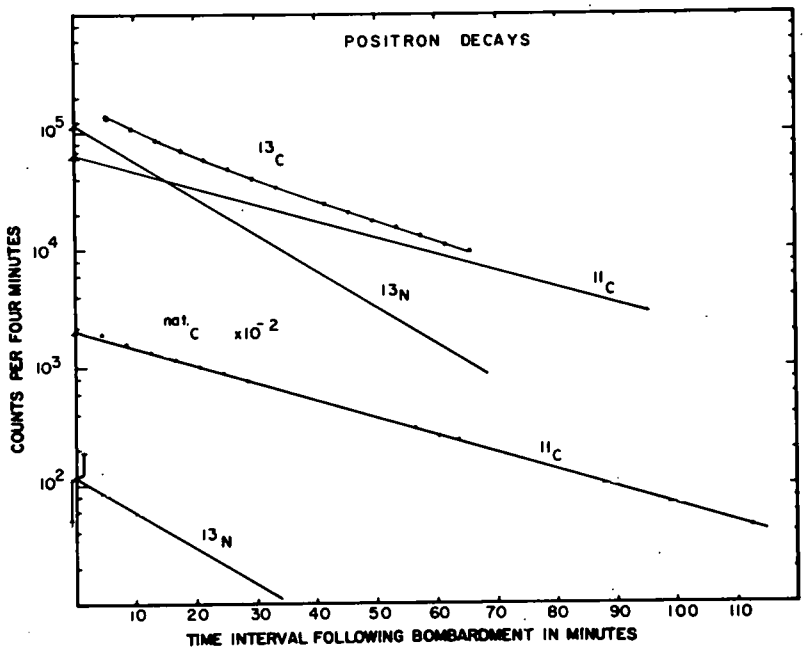

Fig. A3-10 The observed ^{13}N and ^{11}C activities for the enriched (80 atomic percent) C target and for a normal target. Annihilation radiation was counted for four minutes.

The same target was bombarded two minutes using a monitor counter at 55° to integrate the effective yield. The sample was counted over four-minute intervals. The resultant activity was decomposed into the 10 min ^{13}N and 20 min ^{11}C components. A separate run with a normal ^{12}C target was used to correct for the effects of the 20 atomic percent ^{12}C in the sample. The predominant reaction for ^{12}C is $^{12}C(p,d)^{11}C$ while the $^{12}C(p,\gamma)^{13}N$ is sufficiently small to present no problems.

The activity was counted with a Ge(Li) detector looking at the positron annihilation radiation. The yield measurement is accurate to about 6%. The neutron measurements involved the calibration of the detectors wh h were checked by measurements of $^{9}Be(p,n)^{9}B$ reaction and are believed known to 10 percent. The ratio found was $Y^{13}N/Y_{(p,n)}=1.52\pm0.18$. A correction for ^{13}N yield from the ^{12}C target due to the 1 percent ^{13}C, due to $^{12}C(p,\gamma)$ and possible activity of comparable lifetime from the ^{58}Ni will reduce the ratio accordingly. The ratio measurement is being repeated.

Since the ground state of ^{13}C is the only one which is particle stable, it has been assumed that none of the excited states decay by gamma ray emission before dissociating. This preliminary result indicates that this is not true. Theoretical estimates of the gamma ray feeding of the ground state have not yet been made.

24,866

e. Differential Cross Sections for $^{10}B(p,n)^{10}C$ and $^{11}B(p,n)^{11}C$ and Some Macroscopic Reaction Relationships - C. D. Goodman, H. W. Fielding, and D. A. Lind

1/4-7

The reactions $^{10}B(p,n)^{10}C$ and $^{11}B(p,n)^{11}C$ are examples of cases for which simple macroscopic relationships impose restrictions on the reaction cross sections. In addition, a body of data including calculated microscopic wave functions already exist in the literature.[1] Thus, these reactions provide interesting testing ground for nuclear reaction theory.

Simple arguments of isospin symmetry can be used to relate the differential cross sections for $^{10}B(p,n)^{10}C$ and $^{10}B(p,p')^{10}B^*$ (where $^{10}B^*$ signifies the state that is the analog of ^{10}C). The (p,n) cross section should be a factor of two larger but should match the (p,p') cross section in angular shape and in its energy fluctuations until the Coulomb effects spoil the simple symmetry.

For $^{11}B(p,n)^{11}C$ the macroscopic Lane model provides a description of the transition to the $3/2^-$ ground state of ^{11}C as the result of a $(\tau\cdot T)$ interaction potential. One can use a simple orthogonality argument to show that the matrix element for that interaction leading to any other state, in particular to the $3/2^-$ state at 4.79 MeV, must be equal to zero. Thus we can compare a transition in which the Lane

potential is operative to a transition in which it is inoperative even though the other macroscopic quantum numbers are the same.

Previous measurements of $^{11}B(p,n)^{11}C$ did not resolve the 4.79 MeV $3/2^-$ state[2,3] and the angular distributions for both $^{10}B(p,n)^{10}C$ and $^{11}B(p,n)^{11}C$ have very few data points, due to the general difficulty of performing time-of-flight measurements.

We have been able to take advantage of the ease of operation and good energy resolution of the University of Colorado time-of-flight system to obtain time spectra with more than adequate energy resolution at eighteen laboratory angles between 6° and 143°. So far we have made measurements using 16 MeV and 23 MeV protons. The targets were self supporting evaporated films of enriched ^{10}B and ^{11}B.

Sample spectra are shown in Figs. A3-11 and A3-12. Fig. A3-13 shows the angular distribution for the two $3/2^-$ states in the $^{11}B(p,n)^{11}C$ reaction at 16 MeV and Fig. A3-14 shows the same comparison at 23 MeV. Significant differences in shape and magnitude are apparent between the two states. Fig. A3-15 shows the angular distributions for $^{10}B(p,n)^{10}C$ at 16 and 23 MeV.

The experiment is being continued to obtain the relevant (p,p') data for comparison.

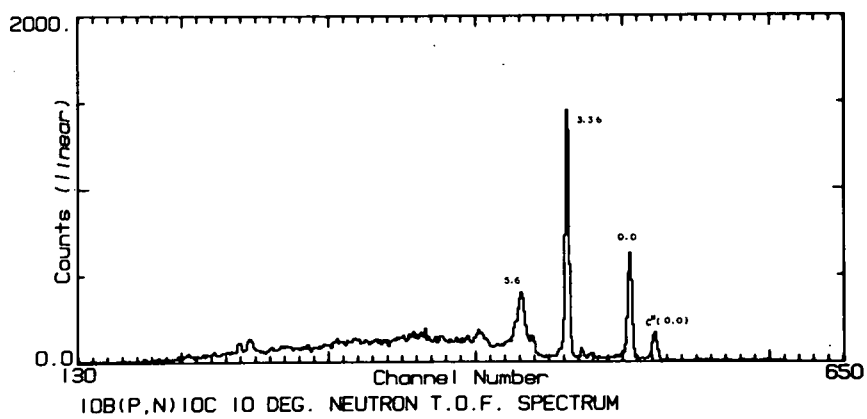

Fig. A3-11 Time-of-flight spectrum for $^{10}B(p,n)^{10}C$.

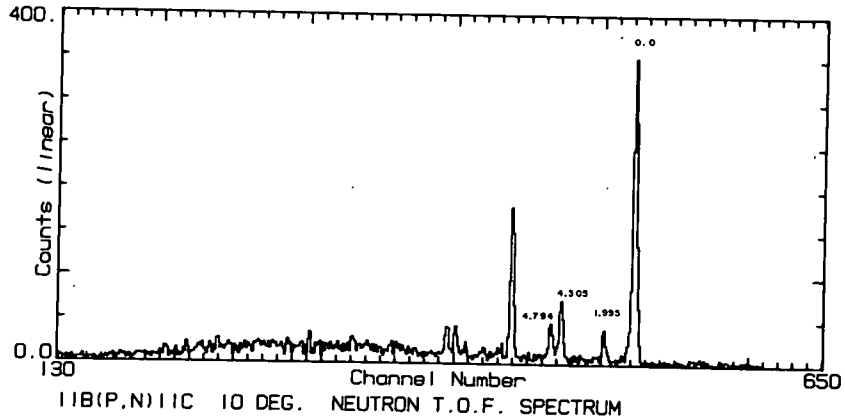

Fig. A3-12 Time-of-flight spectrum for $^{11}B(p,n)^{11}C$.

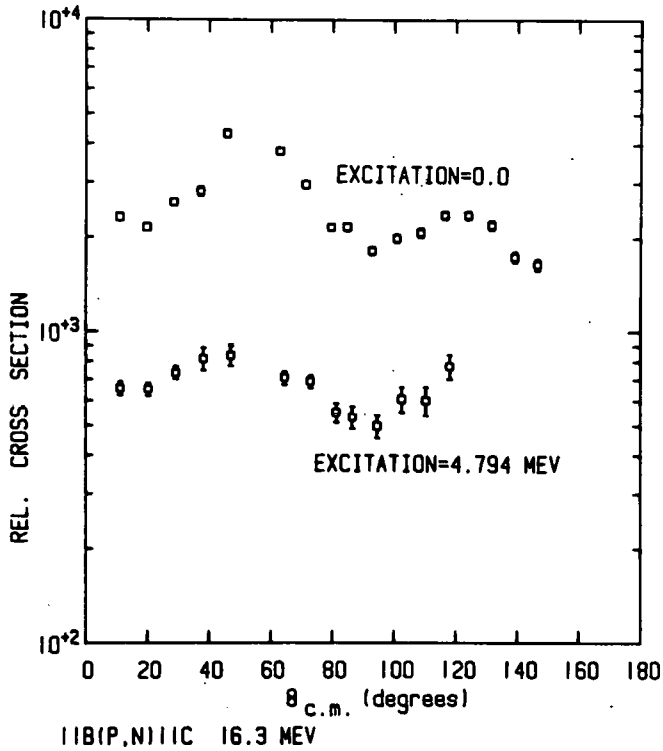

Fig. A3-13 Angular distribution for $^{11}B(p,n)^{11}C$ ground state and 4.79 MeV state at 16 MeV.

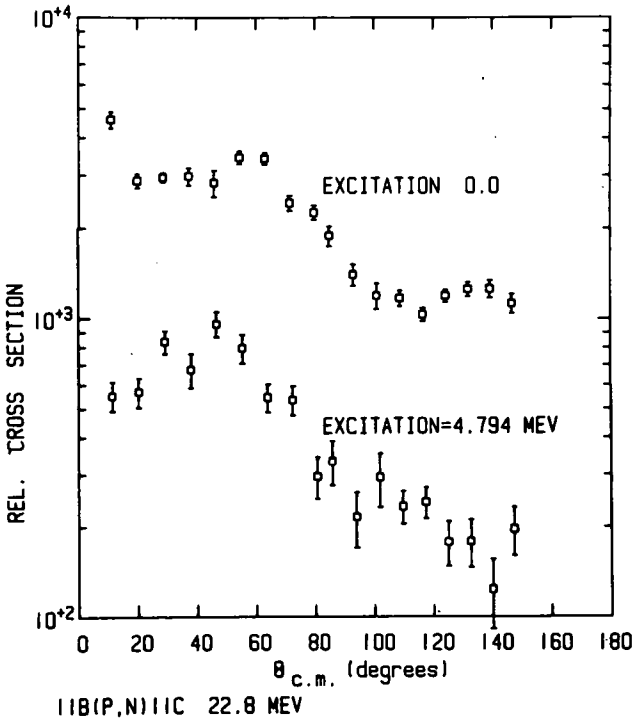

Fig. A3-14 Angular distribution for $^{11}B(p,n)^{11}C$ ground state and 4.79 MeV state at 23 MeV.

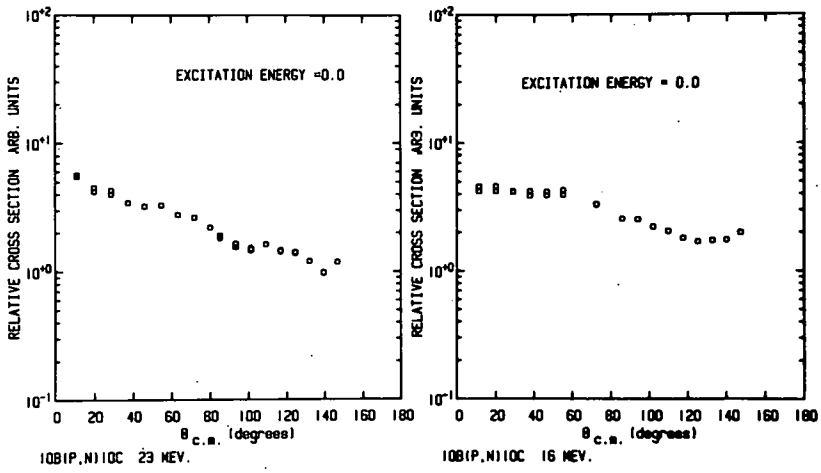

Fig. A3-15 Angular distribution for $^{10}B(p,n)^{10}C$ at 16 and 23 MeV.

---

1 S. Cohen and D. Kurath, Nucl. Phys. 73 (1965) 1.

2 J. D. Anderson, C. Wong, J. W. McClure, B. D. Walker, Phys. Rev. 136 (1964) B118.

3 A. S. Clough, C. J. Batty, B. E. Bonner, L. E. Williams, Nucl. Phys. A143 (1970) 385.

f. The Anti-Analog State Transition $^{56}Fe(p,n)^{56}Co(0^{+}AAS)$ -

L. D. Rickertsen and H. Fielding

Data for (p,n) transitions to isobaric analog states (IAS) over a wide range of nuclei and proton energies have been obtained recently.[1] However, (p,n) transitions to anti-analog states (AAS) have not as yet been measured accurately. Microscopic calculations of the (p,n) reaction, taking into account the two-step process through intermediate deuteron channels as well as the usual charge-exchange, have provided satisfactory fits to the shapes and magnitudes of the IAS angular distributions with little sensitivity to the precise configurations which provide the transition.[2] This is true because the phase and angular dependence of the combined one- and two-step amplitudes for a particular transition turn out to be similar to those for any other and the sum of these amplitudes are, then, not very sensitive to the combination of orbitals which make up the total IAS transition. On the other hand, the calculations for the AAS cross sections require differences between similar amplitudes and the sensitivity to the configurations contributing should be more acute. Hence it was thought to be of some interest to investigate the simultaneous transitions to the 0^{+} IAS and AAS obtained in the $^{56}Fe(p,n)$ reaction.

The experiment was performed on the rotating beam neutron time-of-flight facility using 22.8 MeV protons. The angular distributions shown in Fig. A3-16 were obtained at a 9-meter flight path with three detectors so that data could be obtained at three angles for each setting of the beam angle. At all but extremely forward angles the anti-analog state was not resolved as a

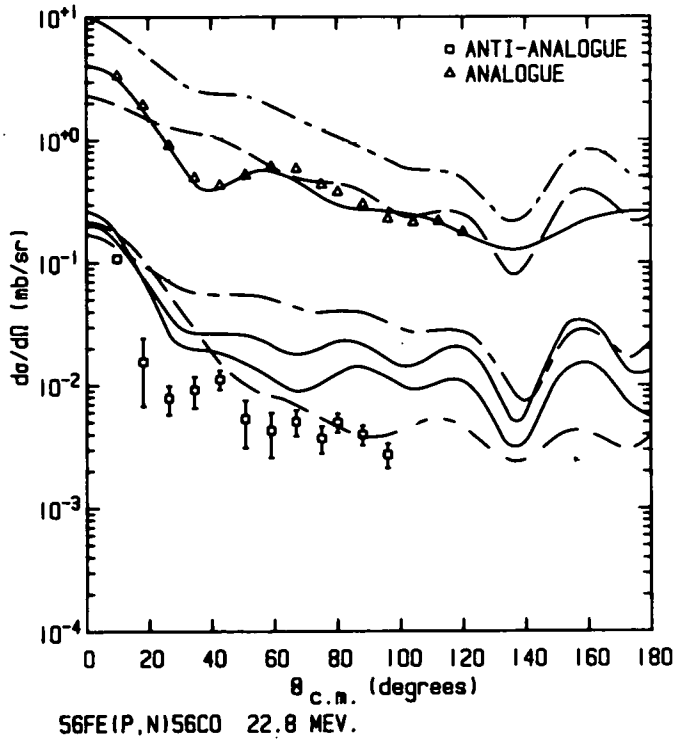

Fig. A3-16 Analog (IAS) and anti-analog (AAS) data obtained with the 9-meter flight path facility. The dash-dot curves are one-step calculations while the long dashed curves are two-step calculations. The solid curves are the coherent sums of both processes. Two choices of spectroscopic factors led to the two solid curves for the AAS but were undistinguishable for the IAS.

separate peak but was unfolded from the tail of the 1.72 MeV level with the program SPECTR. The measurements have since been repeated with the 29-meter flight path so that the AAS was clearly resolved, as indicated in Fig. A3-17. The beam was pulsed to

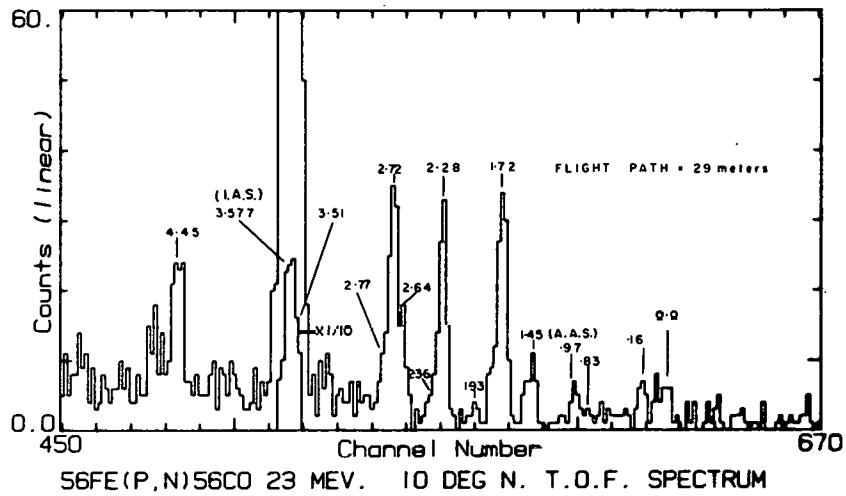

Fig. A3-17 Time-of-flight spectrum for $^{56}Fe(p,n)^{56}Co$ taken with one 1" x 8" detector at the 29-meter station.

allow 1 out of every 10 beam bursts to be accelerated in order to prevent neutron overlap while using the 29-meter flight path arrangement. Only two of the proposed seven detectors were used in obtaining the angular distribution. The detectors were 8" diameter by 1" thick cells of NE224 liquid scintillator. The angular distribution was obtained from 10° to 90° and was in excellent agreement with that shown in Fig. A3-16. The target was a 6 mg/cm^2 natural iron target. The ^{54}Fe component of natural iron cannot lead to neutron groups near the anti-analog state. Spectra were taken with a ^{57}Fe target and no sharp groups were seen in the vicinity of the ^{56}Co AAS.

The results of the calculations and the experimental angular distribution are compared in Fig. A3-16. The calculations have been made assuming the same charge-exchange strength as for other nuclei at this energy[2] and the result of these direct transitions in both the IAS and AAS cases are shown as the dot-dashed curves. The dashed curves are the result of two-step transitions calculated using published spectroscopic factors for the $^{56}Fe(p,d)$ reaction.[3] The full curves give the result of the coherent sums of the two processes. In the AAS case the upper full curve corresponds to calculations using the published spectroscopic values with ratio

$$\frac{S_{5/2}}{S_{3/2}} = \frac{0.435}{0.500} = 0.87.$$

The lower curve has been calculated adjusting this ratio to decrease

the large-angle yield in somewhat better agreement with the data:

$$\frac{S_{5/2}}{S_{3/2}} = \frac{0.17 \pm .05}{0.65 \pm .05} = 0.26 \pm 0.20$$

There is no detectable corresponding change in the IAS results illustrating the relative sensitivity of the two calculations to the configuration mixing.

---

[1] J. D. Carlson et al., Phys. Rev. Lett. 30 (1973) 99.
R. F. Bentley, Ph.D. thesis (unpublished), Univ. of Colorado, 1972.
R. K. Jolly et al., Phys. Rev. C 7 (1973) 1903.
[2] L. D. Rickertsen and P. D. Kunz, to be published, Phys. Lett. 1973.
[3] R. L. Auble and J. Rapaport, Nuclear Data Sheets for A=55, 1970.

4. Other Activities

24,868

a. Thick Target Measurement of Stellar Reaction Rates - N. A. Roughton, M. J. Fritts, R. J. Peterson, C. J. Hansen, and C. S. Zaidins

51-3

The thick target measurement technique described in last year's Progress Report has been used to measure the (p,γ) reaction rate on a number of targets where the product nucleus is radioactive and decays by β-emission or e-capture. We have completed the reactions $^{12}C(p,\gamma)^{13}N$, $^{29}Si(p,\gamma)^{30}P$, $^{46}Ti(p,\gamma)^{47}V$, $^{47}Ti(p,\gamma)^{48}V$, and $^{56}Fe(p,\gamma)^{57}Co$ and the results have been submitted for publication. We have also partially measured the reactions $^{54}Fe(p,\gamma)^{55}Co$, $^{50}Cr(p,\gamma)^{51}Mn$, $^{28}Si(p,\gamma)^{29}P$, and $^{60}Ni(p,\alpha)^{61}Cu$, but the results are not yet final.

The thick target yields which have been measured are shown in Figs. A4-1 and A4-2. It is clear that these curves represent different combinations of resonant and continuum structure, and the analysis of each reaction involves an approach which depends on the

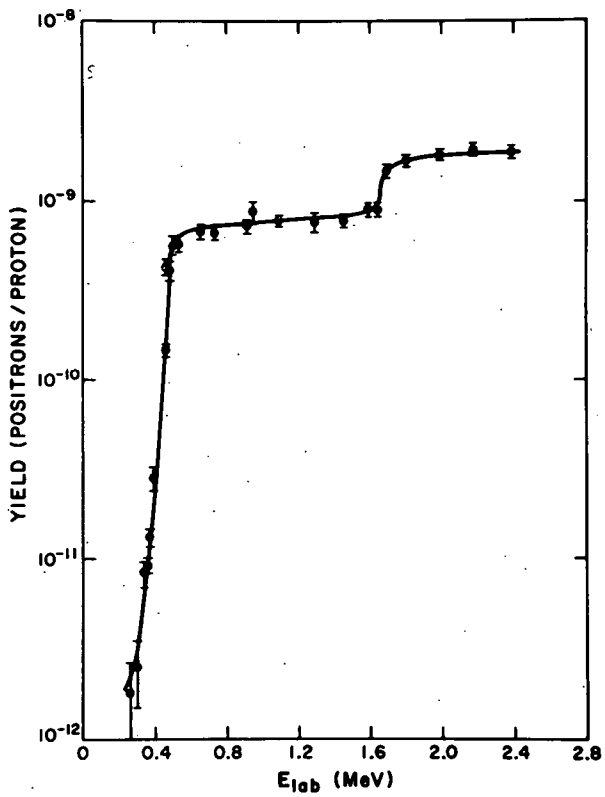

Fig. A4-1 The thick target yield in positrons/incident proton for the reaction $^{12}C(p,\gamma)^{13}N$. The solid curve is the fitted yield.

circumstances. In particular, the carbon yield curve (Fig. A4-1) is dominated by two resonance structures (the upper resonance is actually a doublet). Another very interesting case is the resonance in the $^{56}Fe(p,\gamma)$ curve at just above 1 MeV (Fig. A4-2). This strong

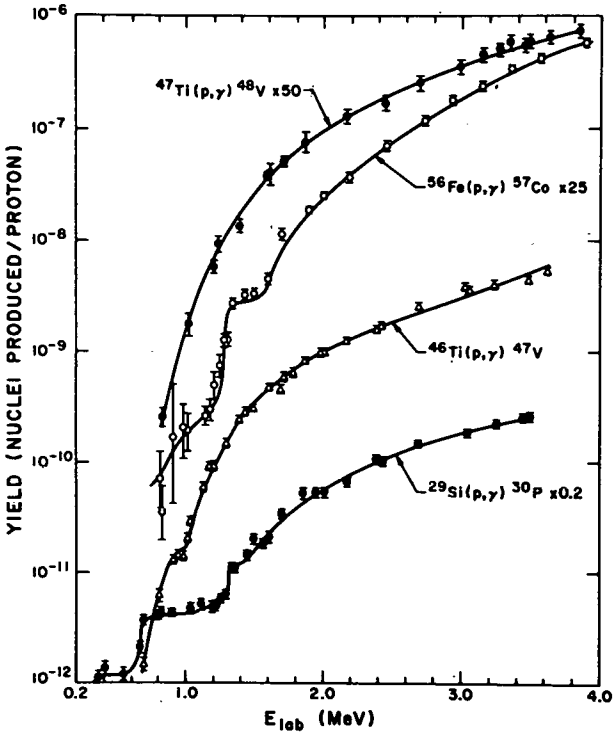

Fig. A4-2 The thick target yield in nuclei produced incident proton for the reactions $^{29}Si(p,\gamma)^{30}P$, $^{46}Ti(p,\gamma)^{47}V$, $^{47}Ti(p,\gamma)^{48}V$, and $^{56}Fe(p,\gamma)^{57}Co$. The solid curves are the fits to the data. Note that the yields have been multiplied by the indicated factors.

resonance is due to the isobaric analog to the ^{57}Fe ground state. The $^{29}Si(p,\gamma)$ and $^{46}Ti(p,\gamma)$ reactions are a mixture of continuum and resonance contributions, while the $^{47}Ti(p,\gamma)$ reaction can be analyzed entirely by a continuum technique. This last treatment is possible because there is a high density of states at the appropriate excitation in ^{48}V, and each contribution is small enough so that no single states dominate the cross section.

The final goal of the experiment is to find the temperature dependence of the Maxwellian averaged cross section times velocity $N_A \langle\sigma V\rangle$ in the approximate temperature range 1×10^9K to 5×10^9K ($1 \leq T_9 \leq 5$). These are in reasonable agreement with previous theoretical expressions, but should be more reliable as they are based on experimentally measured rates.

Two interesting by-products of this project are the development of a "short rabbit" or pneumatic shuttle which can be used in the vault for low energy beams, and the thick target energy loss expression, stopping power and range approximations. Both of these developments are discussed elsewhere in this report.

We are currently finishing some of the measurements mentioned above and bringing the "short rabbit" into a state where it can be used routinely. We have taken data on the short rabbit using both .511 annihilation coincidence measurements and single gamma detection. Both techniques appear to be usable. We also are investigating the reactions (p,n), (p,α), (α,p), (α,n), and (α,γ) for future measurements.

One interesting sidelight is the use of the lowest energy extracted beam to date, a 267 keV proton beam. If we consider the highest energy beam, a 45 MeV ^{3}He beam, as the other extreme, the C.U. cyclotron has a proven dynamic range of 160 to 1.

b. Trace Element Analysis

(24,869) i. Trace Amounts of Fluorine Determined by the $^{19}F(p,p'\gamma)$ Reaction - H. Rudolph, J. J. Kraushaar, R. A. Ristinen and R. R. Meglen 53-6

A wide variety of substances in nature contain traces of fluorine. Although this element is known to be useful when absorbed by organisms in trace amounts, (as in the formation of strong bones and teeth), large environmental burdens of fluorine can have serious effects. Some notable sources of environmental fluorine contamination are aluminum and phosphate production and the burning of fossil fuels. There are several currently used methods for fluorine determination, some of which are listed in Table A4-I. All of the most sensitive methods have severe limitations due to either long sample preparation times or inapplicability to a wide variety of samples. We have developed a technique for fluorine determination which does not suffer from either of these drawbacks.

The technique consists of the detection of prompt gamma rays following the inelastic scattering of low energy protons from ^{19}F nuclei. Gamma rays from the decay of the first (110 keV) and second (197 keV) excited states of ^{19}F were detected with a 20 cm^3 Ge(Li) detector of 1.8 keV resolution at the ^{19}F 197 keV line. An approximately uniform flux of protons was obtained by diffusing the beam by small angle Coulomb scattering in a 1 mg/cm^2 aluminum foil approximately 25 cm upstream from the target position. Calibration targets were manufactured by evaporating a thin film of CaF_2 onto the central 4 mm diameter circular area of 1/8 mil thick mylar film. The amount of fluorine was then inferred by an x-ray fluorescence measurement of the amount of calcium present. Targets were prepared by placing $\sim$ 500 μg of the powdered sample on a thin film of formvar. A dilute solution of polystyrene in toluene was used to bind the sample to the formvar, and an additional formvar cover was placed on top of this. The entire sample preparation requires 15 to 20 minutes.

The sensitivity of the method as a function of proton bombarding energy is shown in Fig. A4-3. The strong resonance in the yield of the 197 keV gamma ray at $E_p \approx 4.6$ MeV leads to a minimum detectable amount for fluorine of 10 ng for 15 minutes irradiation with a beam current density of 0.5 μA/cm^2. Since protons near this energy lose between 200 and 300 keV in a typical sample, the optimum proton energy is $\sim$ 4.7 MeV. It should be noted that the minimum detectable amount for fluorine is less than 50 ng for protons between 2.5 and 6.0 MeV.

TABLE A4-I

Comparison of Fluorine Detection Methods

Detection Method	Sample Preparation		Range[a]	Comments
	Decomposition	Separation	μg	
Gravimetric	Yes	(Yes)[b]	10 - up	Highly matrix dependent
Titrimetric	Yes	(Yes)	10 - up	
Turbidimetric	Yes	Yes	50 - up	
Colorimetric	Yes	Yes	5 - 4500	
Spectrographic	Yes	No	0.1 - 10	Highly matrix dependent
Fluorometric	Yes	Yes	0.03- 30	Many interferences
Enzymatic	Yes	Yes	0.02- 2	Many interferences, esoteric applications
Ion Selective Electrode	Yes	(Yes)	0.1 - up (0.006)	Aqueous samples only
Proton Inelastic Scattering	No	No	0.01- up	

[a] Ref. 1

[b] Some of the detection methods do not require prior sample treatment for some types of samples, but for best results a separation step is recommended.

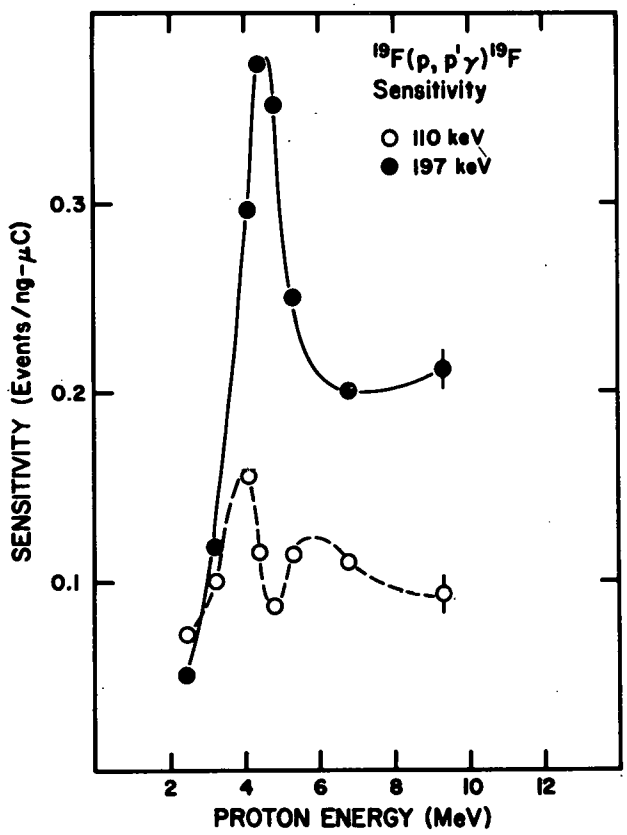

Fig. A4-3 Sensitivity of the $^{19}F(p,p'\gamma)$ reaction vs. incident proton energy using a 400 $\mu g/cm^2$ target of CaF_2. Note the resonance in the yield from the 197 keV gamma ray at 4.6 MeV bombarding energy.

The target preparation described is exactly the same as that used for x-ray fluorescence (XRF) analysis at this laboratory. Hence we are able to use the same target for both inelastic proton scattering and XRF. Fig. A4-4 shows a gamma ray spectrum obtained from one of fourteen coal samples from the Powder River basin in Montana. We have analyzed these samples by both methods in order to obtain baseline information which may be applied to the imminent use of coal from this deposit. As a point of information, the mean fluorine concentration in this coal is 80 ppM with a standard deviation of the mean of 30 ppM.

The technique for fluorine detection described above requires little sample preparation and in principle can be applied to any sample type. The absolute detectability obtained with the technique is better than any currently used method, with the exception of certain specific applications of the ion selective electrode. Further, obvious improvements in detector resolution and detection geometry could reduce the detectable limit to one or two nanograms.

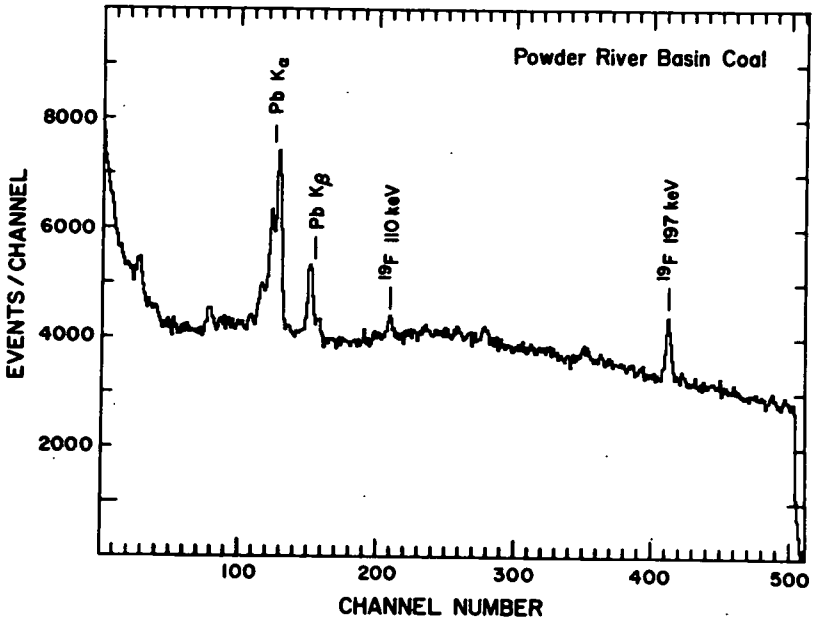

Fig. A4-4 Low energy gamma ray spectrum obtained during the irradiation of one of fourteen coal samples from the Powder River basin.

---

[1] C. A. Horton, Treatise on Analytical Chemistry, Vol. 7, Part 2, New York: Interscience (1961), pp. 207-334.

24,870

c. Neuron Damage by Alpha Particles - J. T. Lett (CSU), E. Powers (CSU), R. A. Ristinen, and W. R. Smythe

A group headed by Professor J. T. Lett of the Department of Radiology and Radiation Biology at Colorado State University at Fort Collins is embarked on a NASA-funded study of "Effect of Cosmic Radiation on the Brain: Consequence of DNA Damage". As a part of this effort, a collaborative project between the CSU group and the Nuclear Physics Laboratory has been initiated to investigate the damage to live neuron cells caused by alpha particle irradiation.

An accurate assessment of the rate of cosmic ray induced brain damage to astronauts on prolonged space flight is of obvious importance when the fact that neurons are non-dividing cells (and therefore do not replace themselves) is considered. Because neurons are non-dividing cells, the usual method of assessing radiation damage by observing the growth rate of a cell colony is not applicable. Professor Lett's group has developed a technique for measuring radiation damage by observing strand breaks in the DNA from the

cell's nuclei. This is accomplished by a complex procedure, involving extracting the neurons, separating the DNA, untwisting the DNA strands, and sorting the DNA fragments according to molecular weight by use of a zonal-rotor ultracentrifuge.

The system used to irradiate rabbit retinas is shown in Fig. A4-5. After removal from the rabbit, the retinas are spread

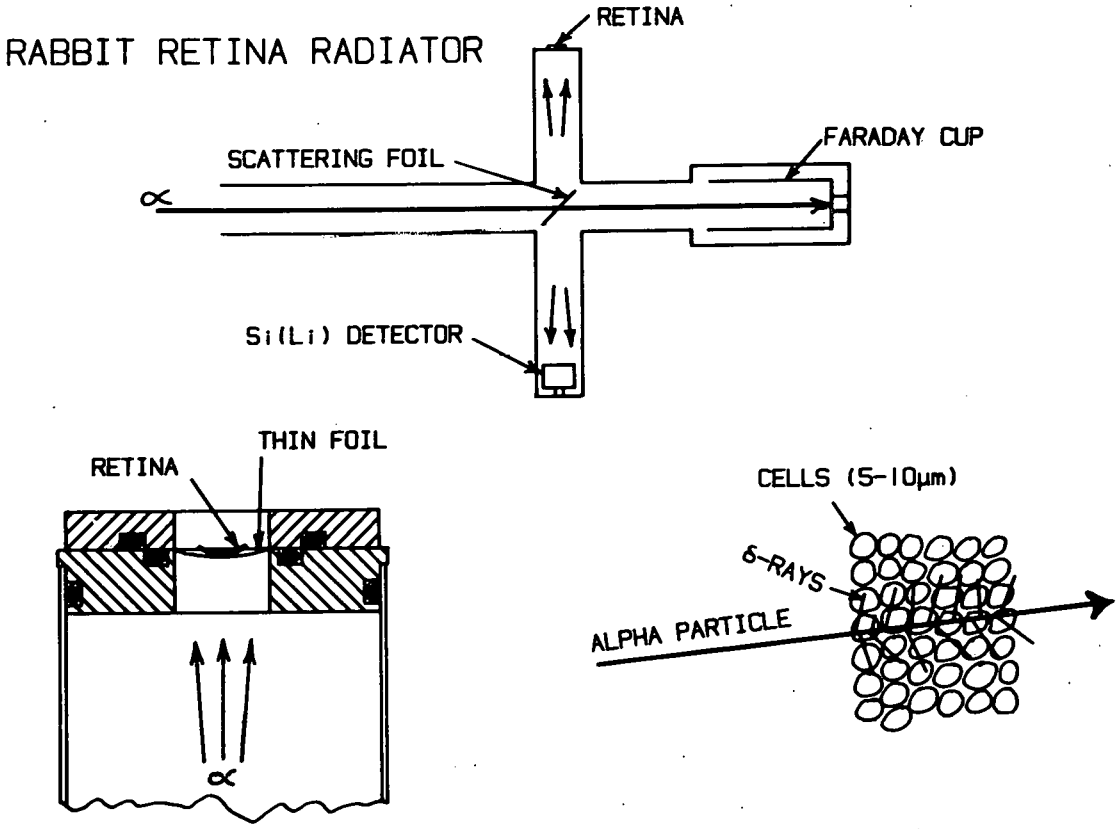

Fig. A4-5 Top. Geometry of the alpha irradiation facility, which permits live tissue to be bombarded by a nearly uniform flux of charged particles. Left. A close-up of the facility. Right. An illustration of one of the questions this experiment hopes to answer. It is believed that all of the cells through which the alpha particle passes are damaged. Are the neighboring cells which are struck by delta rays also damaged? If so, then the number of cells damaged will be significantly increased.

out flat on a thin mylar surface which is placed on a thin, horizontal Havar film through which the alpha particles leave the vacuum. The alphas then pass vertically upwards through the retina. In order to obtain a nearly uniform flux over the area

of the retina (2 cm diameter), alphas scattered out of the cyclotron alpha beam by a foil are utilized. A solid state detector located symmetrically opposite to the retina is used to control the exposure. Exposures of 10^5 to 10^8 particles/square centimeter have been used with radiation times between 20 and 600 seconds.

Preliminary results indicate that neural damage is measurable at all dose levels and that it is significantly higher than was expected. Measurements with luminescent dosimeters have indicated that neutron and gamma ray dose is negligible and have confirmed the alpha dose measurements.

5. X-Ray Fluorescence Analysis - H. Rudolph, W. R. Smythe, J. Boyd, and R. A. Ristinen

24,871

59-

a. Introduction

The development and application of x-ray fluorescence as an analytical technique has continued, with emphasis on the elemental analysis of small (300 microgram) samples. The large amount of information which can be obtained from a small sample makes the technique particularly attractive for medical biopsy applications. The major effort* has been in support of an interdisciplinary study of molybdenum in the environment. In addition, a study of trace element abnormalities among uremic patients is being conducted with the Denver V. A. Hospital.

---

* Supported by NSF-RANN

b. Developmental Work

i. Automated Target Changer

A computer controlled target changer has been designed and constructed. It is designed so that a stack of 32 targets may be loaded in a hopper after which the system is evacuated. The targets are cycled to the irradiation position, rotated constantly during data taking and then displaced into the output hopper by the next target during the change cycle. Rotating the target during irradiation compensates for non-uniform spatial distribution of target material on the target backing.

Particular attention has been paid to maintaining close spacing between the x-ray tube anode and the target and between the target and detector. The mechanical construction of the target changer is complete and the interface to the computer is sufficiently complete to allow the target change cycle to be initiated by a push-button.

ii. Computer System

The basic computer system on which the automated XRF analysis system is based has been delivered. The computer is a Digital Equipment Corporation (DEC) PDP-8/E with 8092 12-bit words of memory. The associated peripheral devices are a dual magnetic tape (DEC tape) transport system, Hewlett-Packard variable persistance display scope and high speed DEC writer terminal. Interfacing for the sample changer, x-ray set, and a Northern Scientific NS-621 ADC is provided using standard 12-bit I/O interface cards purchased from DEC. The interface construction is nearly complete, and much of the software for the system has been written. The automated system should be in operation before the end of the year. At that time we will be capable of routinely processing 25 samples per day.

iii. Data Analysis

Although the samples analyzed by XRF in this laboratory are usually fairly thin, the data for elements with characteristic x-rays less than ~10 keV must be corrected for self-absorption of the x-rays in the sample material. We have developed a computer program which accounts for self-absorption quite accurately. An average background matrix is assumed for the sample, usually with an atomic number Z=12 which is a good assumption for ashed plants, ashed animal tissue and power plant residues. The sample mass absorption coefficients are then revised appropriately for the abundant elements in the sample. The abundant elemental concentrations are calculated iteratively until convergence occurs, and the final mass absorption coefficients are used to calculate the remainder of the elemental concentrations. Convergence usually is attained within five iterations. The method has reproduced elemental concentrations in fly ash over a range of sample mass 100-600 μg where the sample contained 12% Ca and 7% Fe.

c. The Molybdenum Project

Most of the samples analyzed by XRF are from the Molybdenum in the Environment project. Over 2400 samples have been analyzed for this project with approximately 15,000 elemental determinations requested over the past year. Several interesting results are being obtained in this work and are described in detail elsewhere.[1] One particular result which could only have been obtained through a broad range analysis tool such as XRF is exemplified in Fig. A5-1.

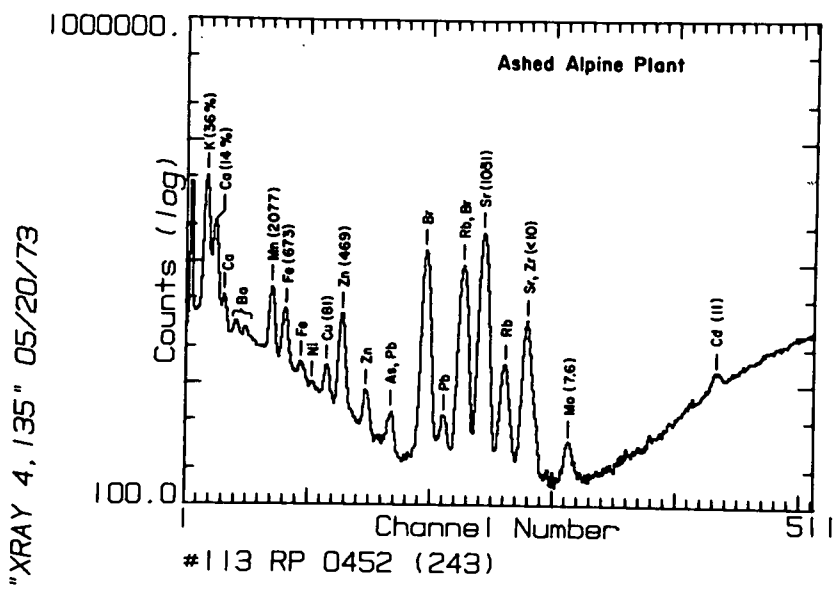

Fig. A5-1 X-ray spectrum from an ashed alpine plant. The concentrations indicated are in ppm ash except for K and Ca.

In certain alpine environments we have observed high levels of cadmium in many plants and animals. There is no concrete explanation of this as yet. We feel, however, that it is highly likely for this environmental cadmium contamination to have been caused by drainage from old abandoned zinc mines in the area.

d. Trace Element Imbalance in Uremia

The NPL trace element group has been collaborating with Dr. Allen Alfrey of the Denver V. A. Hospital and the C. U. Medical School in an effort to correlate certain medical disorders with trace element imbalances. Trace element imbalance problems would seem likely among patients with chronic kidney failure who must have waste products removed from their blood by hemodialysis, the use of an artificial kidney machine.

There are two mechanisms for creating the imbalances. First, the kidney is known to play an essential role in determining the levels of several elements in the body, notably potassium and cadmium. The loss of kidney function could then cause imbalances in the profile of these elements in the body. Second, the dialysis procedure (see Fig. A5-2) is capable of introducing or extracting

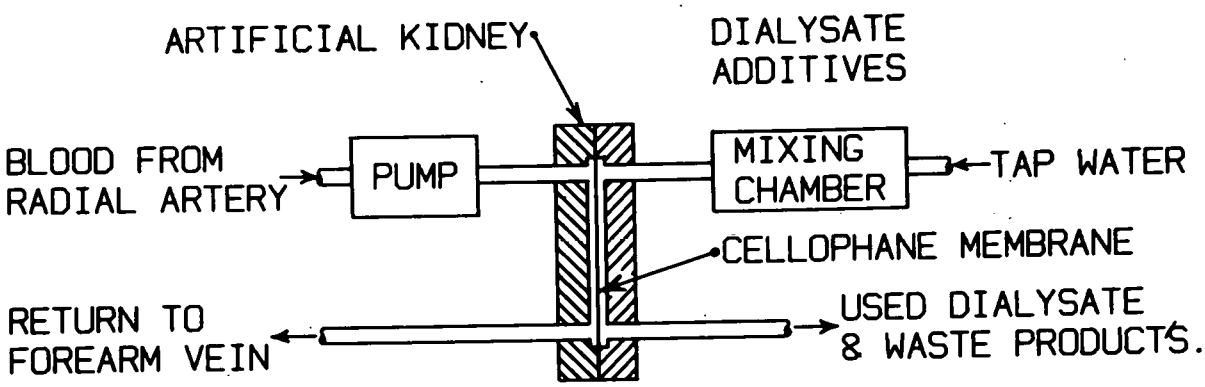

Processes Occurring in Hemodialysis

1. Water is removed.
2. Metabolic end products are removed. (urea, creatinine, and urate)
3. Electrolytes are equilibrated. (Na^+, K^+, Ca^{++}, Mg^{++}, Cl^-, HCO_3^-)

Fig. A5-2 Schematic diagram of the hemodialysis procedure.

trace elements from the patient's blood and hence creating imbalances. An example of the latter is seen in Fig. A5-3 where there is an obvious depletion of bromine from a single dialysis treatment. Evidence also suggests that rubidium is depleted by dialysis.

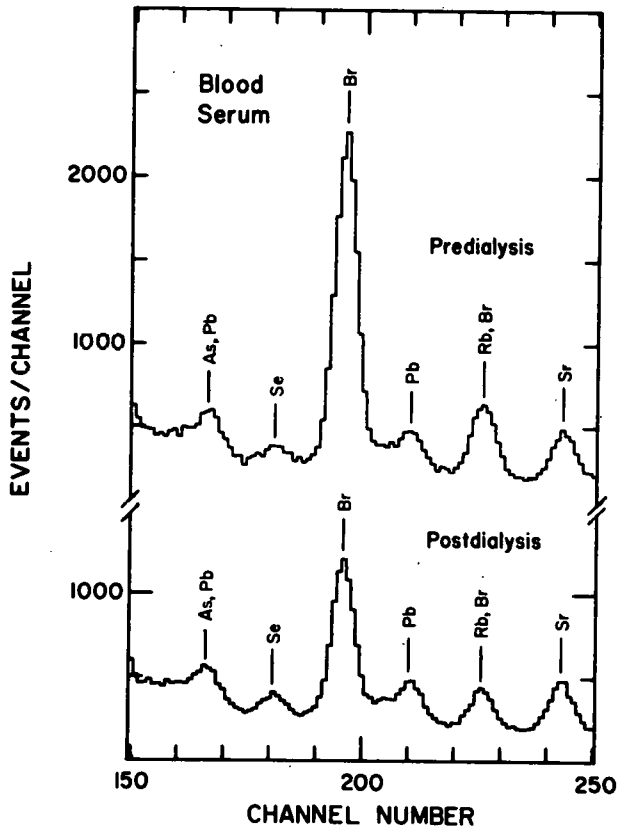

Fig. A5-3 Preliminary direct evidence for bromine depletion by hemodialysis. The spectra shown are averages of three pre- and post-dialysis serum trace element profiles. The serum bromine decrease ranged from 20% to 60% with an average depletion of 50±10%. This correlates well with the low serum bromine levels found in dialysis patients. These data also suggest that serum rubidium levels are lowered by dialysis.

Preliminary studies have begun on tissue samples as well. These include bone, muscle, liver, and brain samples. In general, autopsy samples have been used for the comparison of control, dialyzed uremic and undialyzed uremic groups. The data for muscle is reasonably complete[2] and is illustrated by the spectra in Fig. A5-4. Table A5-I shows the elements for which discrepancies were found between the controls and one or both of the uremic groups. The excess calcium in the uremics had been observed previously, but the other elements shown had not been known to be out of balance. It is possible that one or more of these discrepancies might be

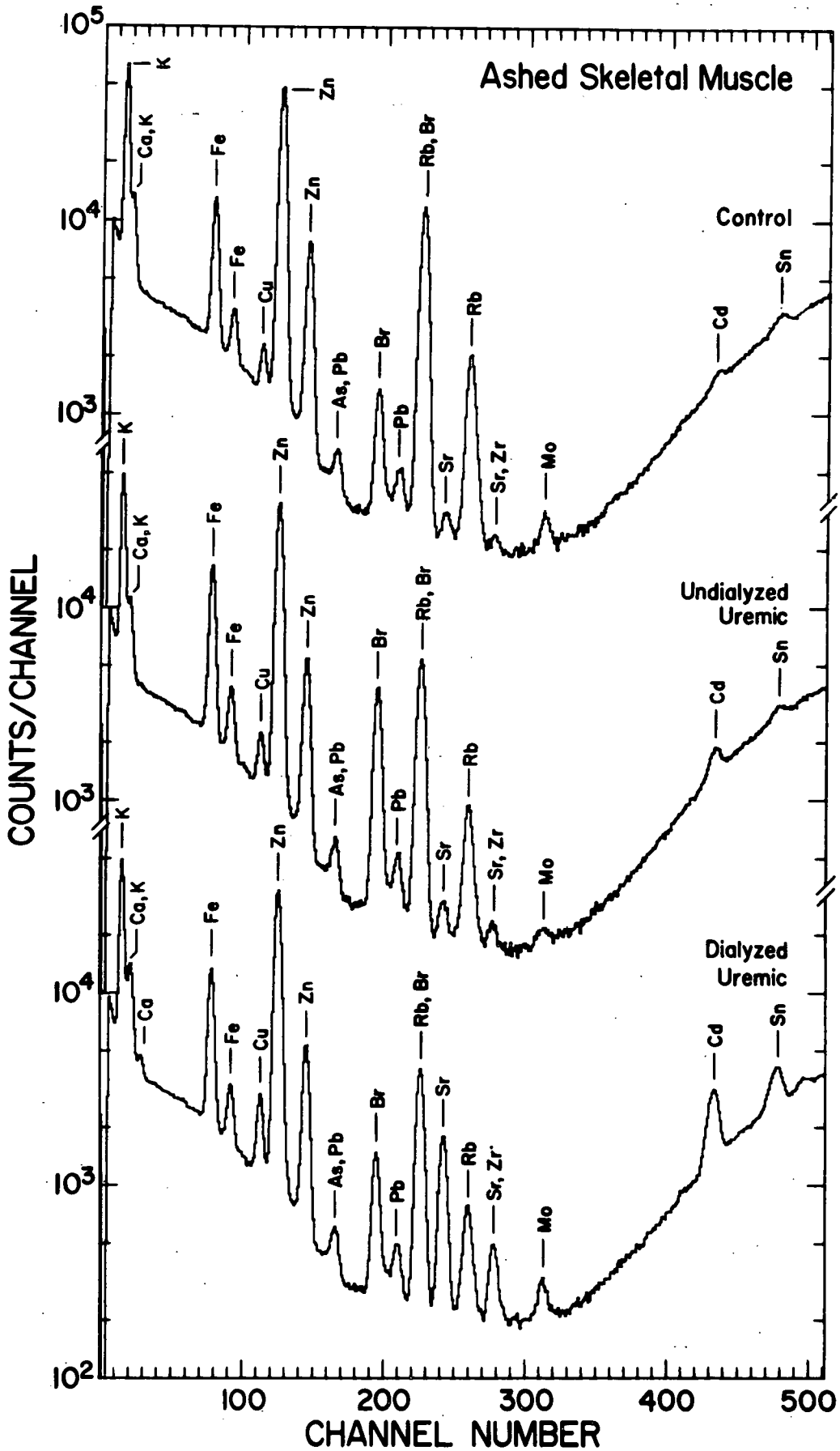

Fig. A5-4 Fluorescent x-ray spectra illustrating the trace elements, observed in skeletal muscle for the three patient groups. Each spectrum represents an average of the results for three subjects.

TABLE A5-I

Abnormal Trace Elements in Muscle (ppM Ash)

Element	Controls[a] (8)	Undialyzed Uremics[a] (6)	Dialyzed Uremics[a] (20)
Ca (% Ash)	0.89±0.48	2.46±1.27	2.85±1.59
Cu	108±30	140±66	154±112[b]
Rb	351±126	220±45[b]	141±59[b,c]
Sr	6.1±3.9	10.1±9.6	41.4±34.7[b,c]
Mo	1.7±0.8	2.3±1.3	2.8±1.6[b]
Cd	5.6±2.3	23.5±12.6[b]	32.5±41.9[b]
Sn	12.7±4.9	22.7±24.9	36.0±18.4[b,c]

[a] Mean ± standard deviation.
[b] $p < 0.05$ controls vs. uremic groups.
[c] $p < 0.05$ undialyzed uremic group vs. dialyzed uremic group.

implicated as a cause of a particular disorder, e.g. both strontium and cadmium have been associated with bone disease and might be involved in uremic osteomalacia.

We feel that the rubidium depletion may be significant. Little is known about the role of this element in body chemistry, however, it has been shown to be of aid in the treatment of depression and thus might be involved in neuronal function. Fig. A5-5 shows that although rubidium is deficient in dialyzed uremics the ratio of Rb

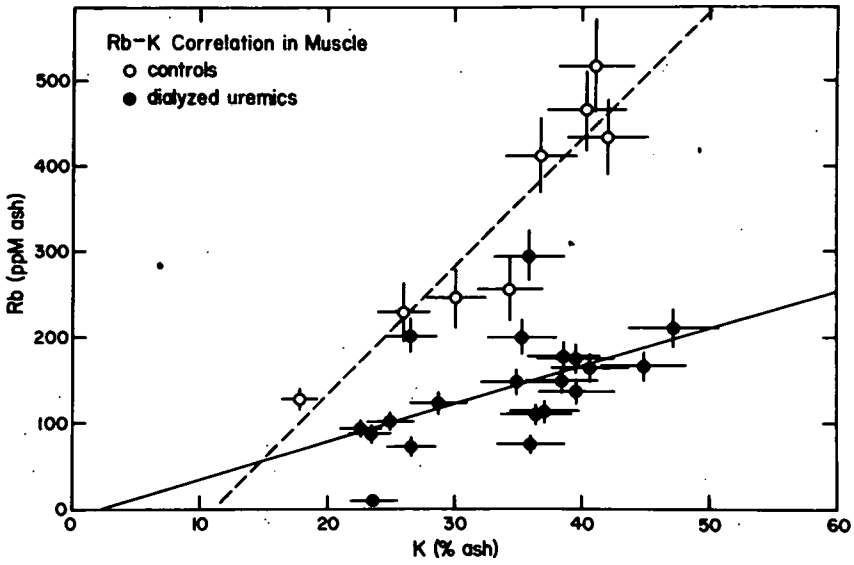

Fig. A5-5 Rb-K correlation for the control group (open circles) and dialyzed uremic group (solid circles). The straight lines are linear least square fits to the data.

to K in muscle is constant but different from normal. Because of the constancy of the Rb-K ratio in the controls, their chemical similarity and the depletion of Rb in undialyzed uremics, it is tempting to infer that loss of kidney function can disrupt the Rb-K balance. Dialysis might tend to accentuate this problem. Some long-term dialysis patients suffer from a neurological disorder[3] which might be due to rubidium deficiency. One rubidium deficient patient has been treated with RbCl, and very preliminary indications are that several clinical symptoms appear to be improved.

e. Outside Services

As a part of our activity, we have begun analyzing a small number of samples for various elements of the surrounding community. For the most part, these services are restricted to one or two samples which will aid in diagnosis of some medical or environmental problem.

As an example of the single sample type of service, the reader is referred to Fig. A5-6. A small portion (~100 μg) from a gum lesion was submitted to us by a local physician. The lesion would not heal, but was known to be benign. The large amount of silver

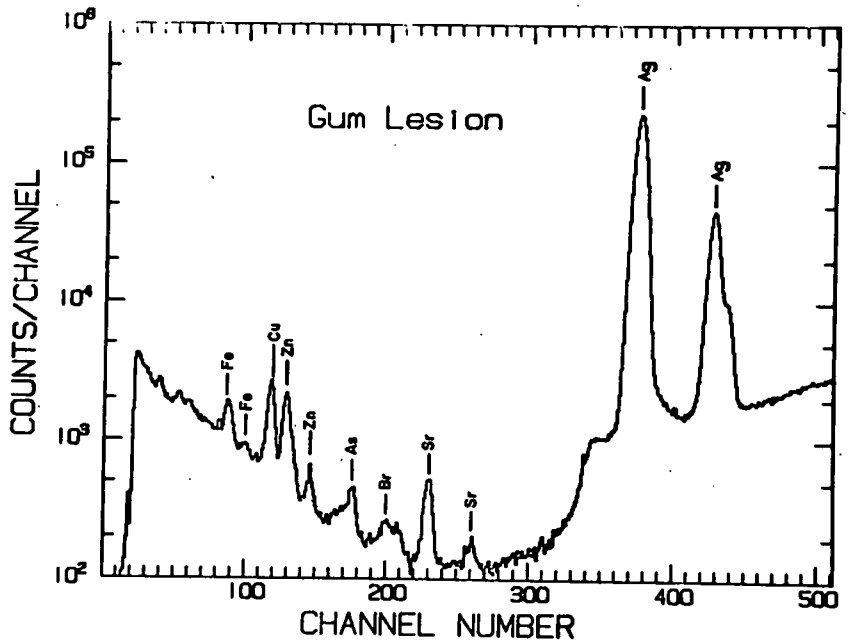

Fig. A5-6 X-ray spectrum from a portion of a periapical lesion. Note the large silver peaks.

found in the tissue sample implicated a recent root canal operation on the patient as the cause of the lesion. Simple surgery was used to correct the problem.

Another attempt at medical diagnosis was made with the submission of four urine samples by the Denver Poisons Laboratory. The woman from whom the samples were taken was suspected to have heavy metal poisoning. The analysis by this laboratory in conjunction with analysis by the Poisons Laboratory eliminated this possibility. The x-ray fluorescence analysis did show the interesting result, however, that the woman's urine contained 9 ppM iodine. After investigation, it was found that the patient was suffering from an incurable cancer and was taking an illicit cancer cure derived from thyroid extract. Although this result had no bearing on the original problem, this does exemplify the investigative possibilities of the x-ray fluorescence technique.

---

[1] "Transport and the Biological Effects of Molybdenum in the Environment", Progress Report, January 1971, NSF-RANN grant GI-34814X.

[2] Muscle and Serum Trace Element Profile in Uremia. H. Rudolph, A. C. Alfrey and W. R. Smythe, Trans. Amer. Soc. Artif. Int. Organs, XIX, (1973) 456.

[3] Syndrome of Dyspraxia and Multifocal Seizures Associated with Chronic Dialysis. A. C. Alfrey, J. M. Mishell, J. Burks, S. R. Contiguglia, H. Rudolph, E. Lewin and J. H. Holmes, Trans. Amer. Soc. Artif. Int. Organs, XVIII (1972) 257.

B. Intermediate Energy Physics

1. Proposal for the Study of Giant Multipole Resonances by Pion Scattering at LAMPF - R. J. Peterson, J. J. Kraushaar, D. A. Lind, R. A. Ristinen, B. W. Ridley, and N. Ensslin

A proposal for 180 hours of beam time on the EPICS system has been submitted to the LAMPF Program Advisory Committee. The virtues of the pion for inelastic scattering to giant multipoles (E1, $\Delta T=1$; E2, $\Delta T=0$ are the ones currently known) include the possibility of distinguishing neutron excitations from proton excitations by comparison of π^+ and π^- spectra, and the expected structure in the angular distributions. Fig. B1 shows a sample DWBA calculation, with a collective surface deformed form factor, and a strength exhausting the appropriate sum rule strength, using the same form factor to compute the electromagnetic strength. This form factor is not correct, but the calculation has the correct kinematics. The pion is a high energy, spin 0, particle with wave number such that the oscillations occur in a convenient angular range.

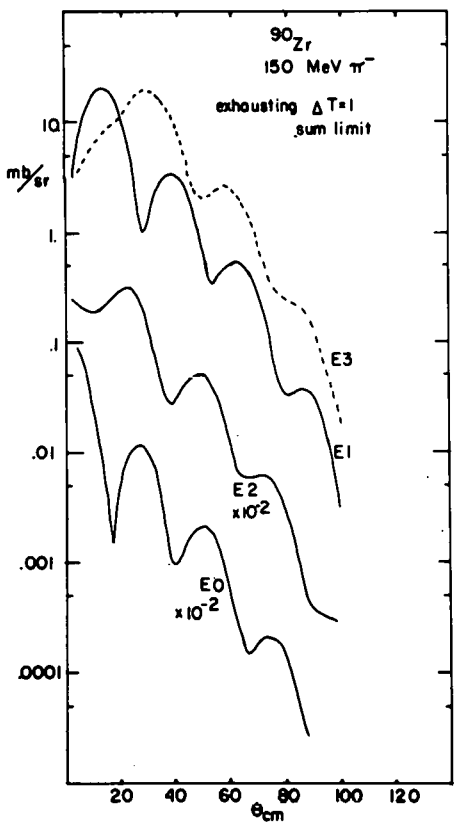

Fig. B1 The excitation of $\Delta T=1$, 0^+, 1^-, 2^+, and 3^- states of ^{90}Zr at an excitation of 20 MeV is assumed. The strengths B_L^2 used for the predictions exhaust the electromagnetic transition sum rule for each multipolarity. The $\Delta T=0$ predictions would be smaller by a factor near 0.8. The strong oscillations give a clear signature of each multipolarity.

2. Phase Shift Fits to Pion Elastic Scattering - W. J. Lynch and R. J. Peterson

A computer code has been written to search for best fits to pion elastic scattering data, using either the phase shifts

themselves, or parameters in a functional form for the phase shifts, as parameters. A global survey of data on ^{4}He, ^{12}C, and ^{16}O has been begun, in an attempt to find systematic trends with energy and mass. Much impetus for this project has been removed by the publication of similar work on ^{12}C.[1] This program will be used, however, in the analysis of the pion-deuteron data we will be taking at LAMPF.

---

[1] J. Beiner, Nucl. Phys. B53, (1973) 349.

3. Slit Scattering in the EPICS Beam Line - N. Ensslin

A computer program is being run at LAMPF to help design the collimating slits and apertures of the pion channel and spectrometer. The program traces randomly chosen pions through a series of slits, vacuum pipes, and magnets. The slits may be straight or curved in cross section, with rectangular or elliptical apertures. Muons produced by the decay of pions in flight are also carried through the system. When a particle strikes a slit, it is stepped through the material in intervals of 1 mm to 1 cm. At each step multiple scattering, energy loss by ionization, and collision loss by nuclear interactions are allowed for.

Initial tests with a single slit verified that the best collimation is obtained with slightly curved jaws of high Z material. Then the pion channel itself, which contains four bending magnets and ten pairs of uranium jaws, was simulated by thin lenses, as illustrated in Fig. B2. It was found that about 5% of the pions incident on the scattering target will have scattered from slits in the channel. Proton contaminations of about 5% and muon contaminations of about 25% are also predicted.

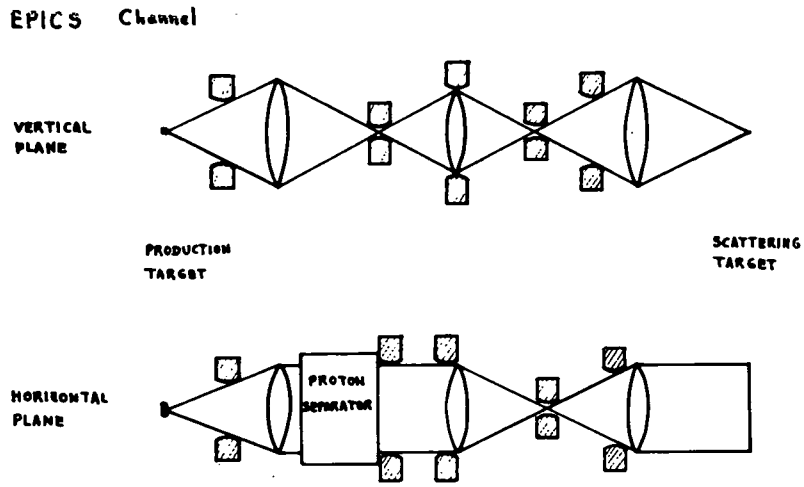

Fig. B2 A schematic sketch of the EPICS channel showing the apertures assumed for the slit scattering calculation. The extreme accepted pion rays are also shown.

A simulation of the entrance to the pion channel (Fig. B3) was used to study the design of the fixed slits. These slits shield the first uranium jaws from the intense flux of particles emanating from the production target. The program predicted that a low-Z liner on the fixed slits would reduce the number of particles scattered back into the opening between the uranium jaws.

The slit scattering program is now being used to study the backgrounds expected in the spectrometer. This instrument lacks collimating jaws of high Z material, but is equipped with detectors that should make it possible to project all particles back to their origin. The program is being used to predict the expected background and to determine the need for low-Z liners or veto counters.

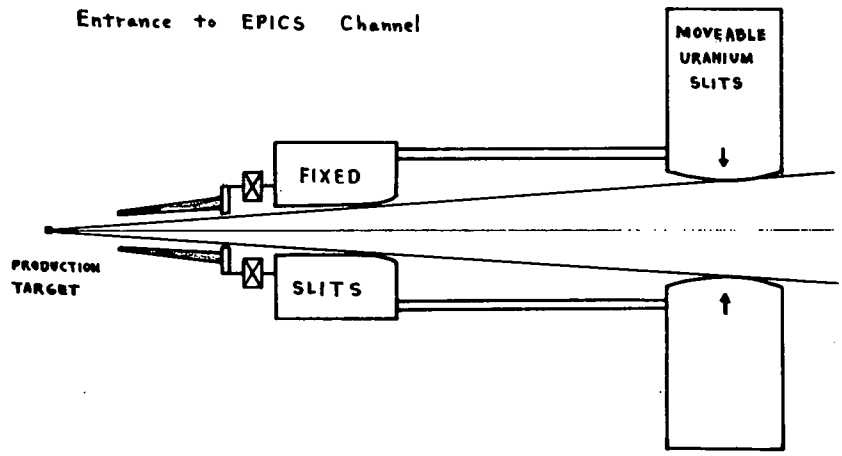

Fig. B3 Detail of the entrance slits to the EPICS channel. The slit scattering calculation is being used to determine the geometry and material for these slits to minimize the slit-scattered beam propagated to the scattering target.

24,872 4. Glauber Calculation of Pion-Deuteron Scattering - A. Rosenthal and R. J. Peterson 69-70

A computer program to calculate the elastic pion scattering from the deuteron in the Glauber approximation[1] has been completed. The pion-nucleon amplitudes are taken from the fit of Roper.[2] The first exercise has been to assume only an s-state deuteron, and to investigate the role of the spin-flip and charge exchange degrees of freedom. A Gaussian form factor with range parameter a=3.2 fm has been used. If the pion flips the spin of one nucleon in a scattering, one is led to the first (unbound) excited state. If both are flipped, the scattering is elastic. In Fig. B4 are shown the single and double scattering for a pion energy of 200 MeV, with and without the spin flip mode. The double-scattering spin flip

cross section is too small to show on this scale. Also shown is the double-scattering non-flip term without charge exchange as an allowed intermediate state.

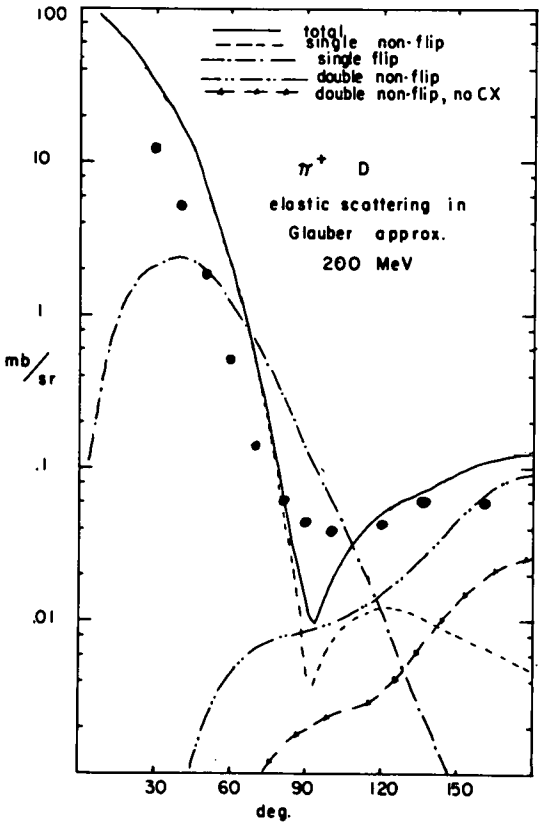

Fig. B4 The π^+-D Glauber prediction at 200 MeV is shown as its several parts. The single spin-flip is an inelastic term. The importance of including the charge exchange intermediate state in the double scattering is seen. Also plotted are some data points at 256 MeV (lab).

It is seen that the spin flip (inelastic) yield is not small, but the double flip is negligible. The double scattering is most important at back angles, as has been noted before,[1] and the inclusion of the charge exchange intermediate state is vital. Also shown are the data from a recent experiment at a lab energy of 256 MeV.[3]

Future work with this code will be to include the D-state of the deuteron, and a more realistic form factor for the deuteron. The sensitivity to several possible arcane components of the deuteron (such as an N* content) will also be tested.

---

[1] V. France and R. J. Glauber, Phys. Rev. 142 (1966) 1195.
[2] L. D. Roper et al., Phys. Rev. 138 (1965) B195.
[3] K. Gabathuler et al., Nuclear Phys. B55 (1973) 397.

C. Apparatus and Facility Development

1. The Magnetic Spectrograph System - D. E. Prull, E. W. Stoub, B. W. Ridley, R. A. Ristinen, R. J. Peterson, and R. A. Emigh

a. Introduction

The basic design features of the magnetic spectrograph system are described in previous reports.[1,2] In summary, the system consists of three parts, as shown schematically in Fig. C1-1. The

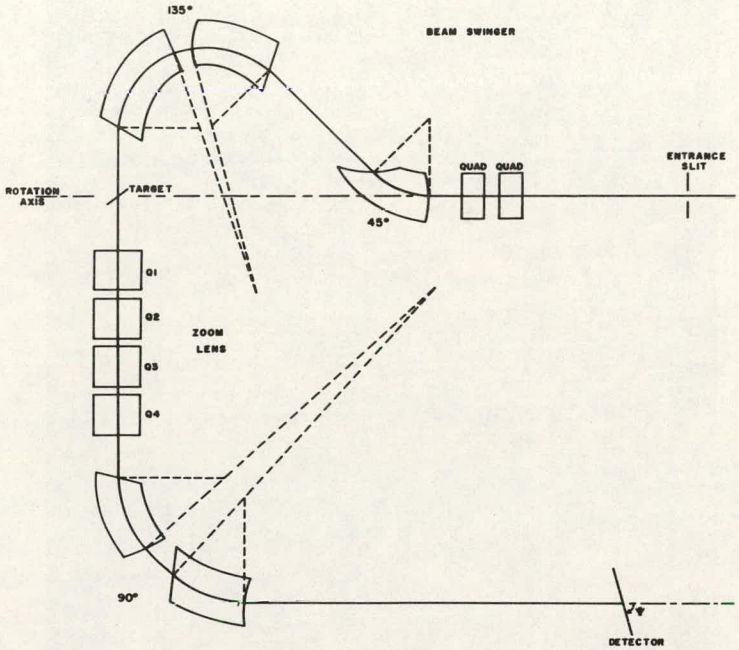

Fig. C1-1 Schematic of the magnetic spectrograph system described in the text.

first part, called the "beam swinger", is a beam preparation system consisting of a QQD(DD) magnet configuration mounted in a frame that rotates about a horizontal axis aligned with the input beam from the cyclotron. The second and third parts of the system, the "zoom lens" and charged particle spectrograph, are mounted in a fixed position beneath the target with their dispersion plane oriented vertically. The zoom lens is a QQQQ magnet configuration that provides the means for dispersion matching between the beam swinger and the charged particle spectrograph, a 90° dipole magnet in a (D,D) configuration. The scattering angle is varied by rotating the beam swinger within the range -90° to +135°.

The last elements of the system completed were the four

quadrupoles in the zoom lens and the multiwire proportional counter. The quadrupoles were tested with the field mapping technique described in a previous report.[2] Results of this field mapping and a discussion of the multiwire proportional chamber are described later in this section. The final construction of the system was completed in December, 1972. (See Fig. C1-2.)

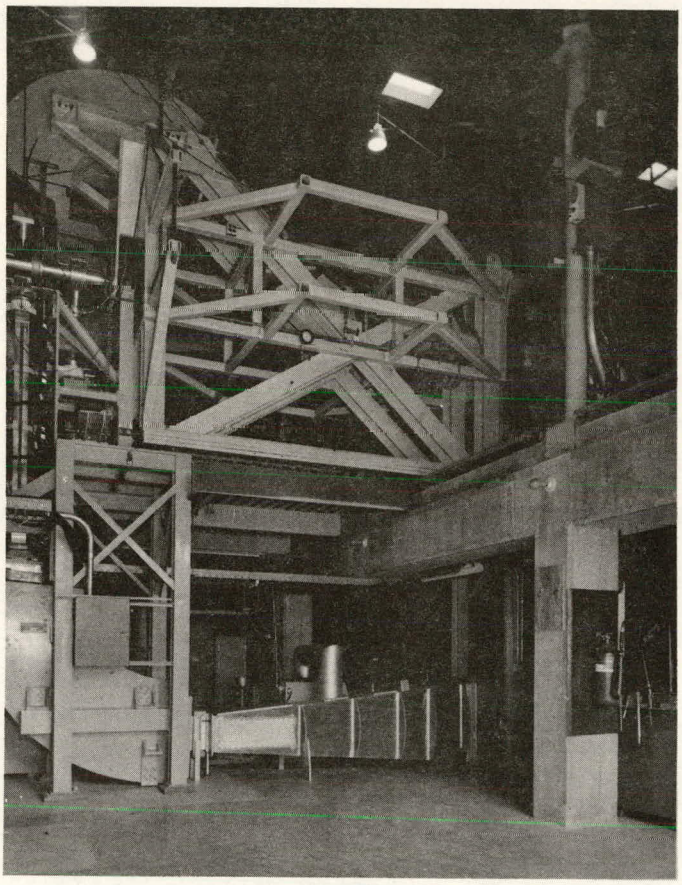

Fig. C1-2 Picture of the magnetic spectrograph system taken after final construction. The beam swinger is at 0° rotation angle.

b. The Beam Swinger

The beam swinger may be operated in either of two modes: an isochronous mode, or a high dispersion mode. These are achieved using different excitations of the QQ doublet.

The isochronous mode is used to deliver beam pulses of very short duration on the target. In this mode, the beam swinger is used for changing the scattering angle of the neutron T.O.F. spectrometer which employs a long fixed neutron flight path. This mode has been used extensively with the results presented elsewhere in this

report.

The high dispersion mode is used in conjunction with the zoom lens and charged particle spectrograph. In this mode, the entrance aperture of the beam swinger becomes a "source" which is transformed to a line image at the target position. The position of this line image in the dispersion plane of the beam swinger is proportional to the momentum of the incident particles.

The momentum resolution of the beam swinger is determined by the coherence of momentum versus position on the target. An experimental check of this coherence was performed using the reaction $^{12}C(p,p')^{12}C$. At 14.231±.004 MeV proton energy, a sharp resonance is known.[3] The shape of the excitation functions for elastic and inelastic scattering differ strongly near 165 deg. scattering angle, with their ratio of course being independent of the beam current incident on the target.

A strip of 50 $\mu g/cm^2$ carbon foil 0.8 mm wide was laid across a thin gold foil placed in the target position. The momentum of the particles striking the strip should be proportional to the magnetic field in the 135° split-pole magnet, which in turn is proportional to the current in the magnet. The observed ratios of elastic to inelastic yield taken with a solid-state counter at 165 deg. are plotted as a function of the 135° magnet current in Fig. C1-3. The solid curve is taken from the high resolution

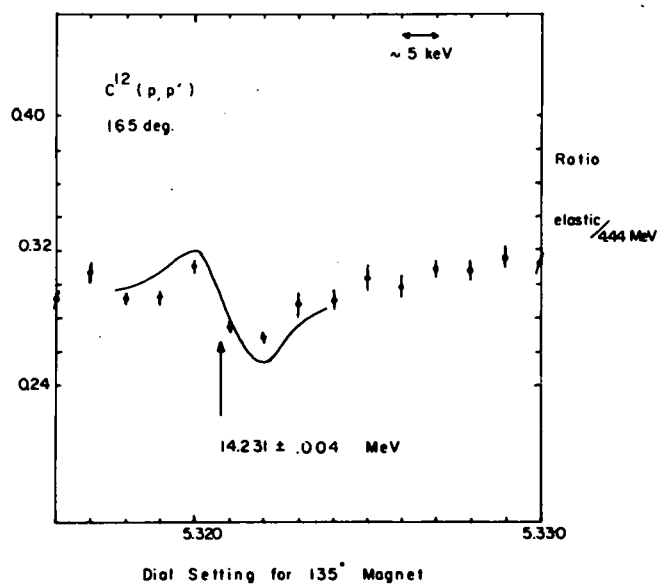

Fig. C1-3 The ratio of elastic to the 4.44 MeV inelastic cross sections of protons on ^{12}C at the 14.231 MeV resonance. The observed anomaly is compared to a curve taken from a high resolution experiment smoothed by the estimated 5 keV target contribution.

data of Levine and Parker,[3] with a 5 keV smoothing corresponding to the estimated contribution due to the target thickness and width of the strip. The results show the energy resolution on target is not more than 3 keV. The momentum resolution of the beam swinger is therefore no worse than one part in 10^4, in excellent agreement with predictions based on ray tracing and beam optics claculations. The properties of the beam swinger are summarized in Table C1-I.

TABLE C1-I

Beam Swinger (Measured Data)

Entrance aperture: 2.53 mm radius

Quadrupole doublet: Standard Spectromagnetic 4" quadrupole

45° Dipole Magnet:

Gap 3.80 cm.
B_{max} 10 kg.
Entrance VFB: orientation ±0.45°, curvature +109 cm.
Bending radius 88.3 cm.
Exit VFB: orientation -45.6°, curvature -109 cm.

135° Dipole Magnet:

Gap 3.80 cm
B_{max} 10 kg.
First pole: entrance VFB: orientation +30°, straight edge
bending radius 87.9 cm.
exit VFB: orientation +18°, curvature +127 cm.
Low field region: bending radius 277.2 cm.
Second pole: entrance VFB: orientation +3.8°, straight edge
bending raiud 87.9 cm.
exit VFB: orientation +30°, straight edge

On Target:

Dispersion 354 cm.
Magnification 0.12
Momentum resolution ≤one part in 10^4
Acceptance momentum band ±0.1% *

* Determined by available target size.

Experimental setup time for the 0° beam line and the beam swinger is minimal with the aid of the computer code OPTICS described elsewhere in this report. In a typical experiment, 90% transmission is achieved from the cyclotron vault (flag 2) to the

target when currents in the beam transport elements are set at the values calculated by OPTICS. Beam currents up to 10 μa. on target are not unusual.

c. Zoom Lens and Charged Particle Spectrograph

Momentum analysis of reaction products is achieved with the charged particle spectrograph, a 90° split-pole dipole magnet. The source for the 90° magnet is the virtual image of the target formed by the zoom lens. Four quadrupoles are needed to fix the axial position of the virtual image in both the dispersion and transverse planes. The transverse magnification is also fixed while the magnification in the dispersion plane, M_x, must be variable within a range 0.7 to 3.1 to provide dispersion matching between the beam swinger and the 90° magnet. The magnification is given by:

$$M_x = 0.89 \frac{\left[\frac{p_1^2}{T_1+m_1}(M-m_2-T_2) + p_1 p_2 \cos\theta\right]}{\left[\frac{p_2^2}{T_2+m_2}(M+m_1+T_1) - p_1 p_2 \cos\theta\right]}$$

where m_1, p_1, and T_1 are the mass, momentum, and kinetic energy of the incident particles, M is the target mass, θ is the laboratory scattering angle, and m_2, p_2, and T_2 are the mass, momentum, and kinetic energy of the reaction product.

Considerable effort was devoted to the design of the zoom lens quadrupole magnets. Calculations based on ray tracing indicated the harmonic content of the magnetic field at the pole tip should be better than 99% pure quadrupole. In addition, the axial position of the virtual field boundary should be independent of radius and field excitation.

A quadrupole field mapper was designed and built specifically to measure magnetic field gradients in the zoom lens quadrupoles.[2] It was found that the line integral through the complete magnet for all four of the zoom lens quadrupoles shows very pure quadrupole fields (see Fig. C1-4). The only higher order multipole of any significance found is the n=6 multipole (dodecapole). The amplitude of the dodecapole at the pole root is less than 0.7% of the quadrupole amplitude. These results were verified with a Bell model 640 Hall effect gaussmeter. The axial position of the virtual field boundary was found to be independent of field excitation and radius to 0.4% of the magnet's effective length.

The momentum resolution of the zoom lens and charged particle spectrograph was checked using a long slotted aluminum plate located in the predicted focal plane. The one mm. wide slots were spaced at 6.35 cm intervals. A solid plate behind the slotted one collected current passing through the slots. The beam swinger was fixed at 0° rotation angle.

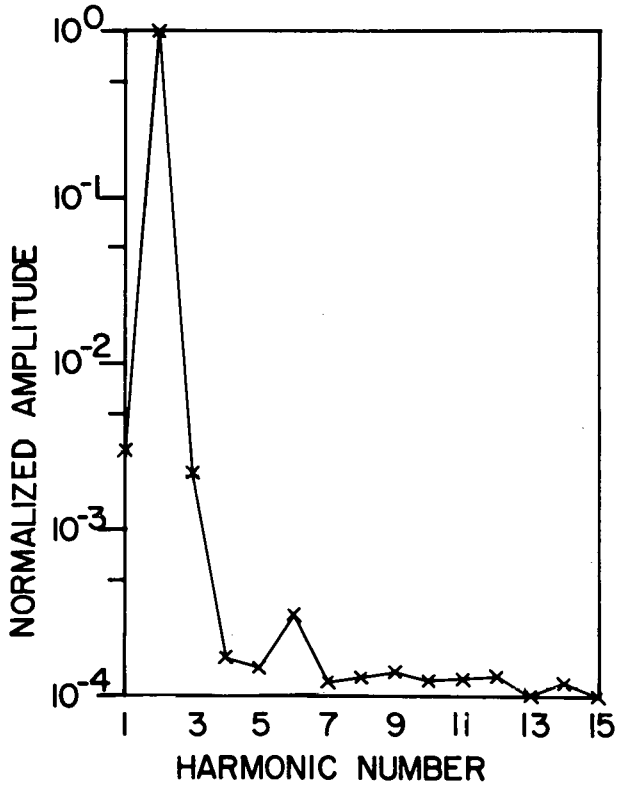

Fig. C1-4 Harmonic content of the magnetic field in the zoom lens quadrupole at a radius of 3.048 cm. The n=1 and n=3 amplitudes shown are due only to the electronics. The field mapping system was accurate to one part in 10^4 of the n=2 amplitude.

Initially an aluminum plate with a one mm. wide slit was placed at the target position to provide a monokinetic beam for the spectrograph. It was found that 80% to 90% of the beam could be transmitted through the slots in the focal plane. A calibration of slot position versus current in the 90° magnet shows the dispersion of the system is constant along the focal plane, with a measured value of 6.42 meters. The momentum resolution is no worse than 1.6 parts in 10^4 (for zero Q-value reactions) and the focal plane is indeed a plane surface at 70°.

Measurements were also made with the slit at the target position removed. In this case, 60% to 80% of the beam was transmitted through the focal plane slots. This verified the dispersion matching for zero Q-value reactions and gives an overall momentum resolution of about 1.6 parts in 10^4, as compared to a predicted resolution of 1.7 parts in 10^4 (see Fig. C1-5). The measured properties of the zoom lens and charged particle spectrograph are summarized in Table C1-II.

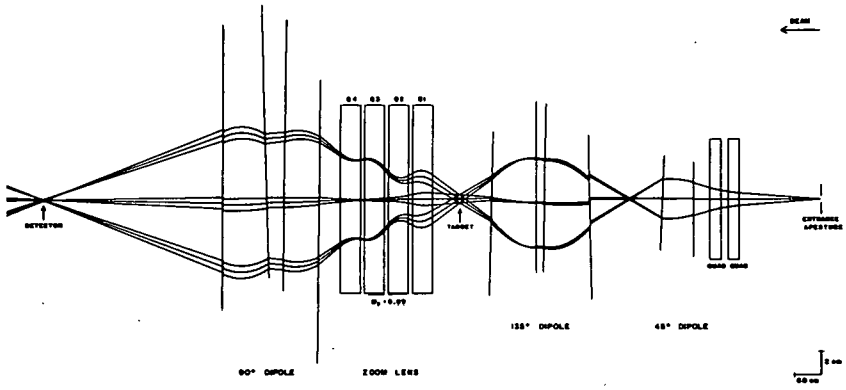

Fig. C1-5 Particle trajectories through the magnetic spectrograph system for a reaction with zero Q-value and initial momenta P_o and $P_o \pm 0.1\%$. Results indicate an expected momentum resolution of 1.7 parts in 10^4.

TABLE C1-II

Zoom Lens and Charged Particle Spectrograph (Measured Data)

Zoom Lens

Four identical units
Each unit: Length 43.18 cm.
Aperture 8.43 cm.
Max field gradient 1.2 kg/cm.
Pole shape: hyperbolic
Harmonic content ≥99% pure quadrupole at pole tip
Magnification M_x - variable from 0.7 to 3.1

90° Dipole Magnet

Gap 4.5 cm.
B_{max} 13 kg.
First pole: entrance VFB: orientation -13.1°, straight edge bending radius 120.5 cm.
exit VFB: orientation +15.4°, radius +105 cm.
Low field region: bending radius 482 cm.
Second pole: entrance VFB: orientation +41.3°, straight edge bending radius 120.5 cm.
exit VFB: orientation +3.7°, curvature -70cm.

At Detector

Solid angle 10^{-3} ster.
Dispersion 642 cm.
Magnification - variable from 1.4 to 6.2
Transverse beam extent ≈ 25 mm.
Momentum resolution $(M_x/0.89) \times 1.7 \times 10^{-4}$
Acceptance momentum band 8.4%

d. Magnetic Spectrograph Trim Coils

When the magnification M_x of the zoom lens is changed significantly from 0.89 (the magnification for zero Q-value reactions) chromatic aberrations are introduced in the virtual image of the target. This causes the focal plane angle of the charged particle spectrograph to decrease and changes the plane to a curved surface. A set of trim magnets are needed to keep the focal surface a plane at a fixed orientation. These trim magnets are placed at both the entrance and exit of the 90° magnet.

From ray tracing results it was found that the trim magnets should have the property:

$$\int \vec{B} \cdot d\vec{\ell} = ax^2 + 6x^3$$

where: B is the magnetic field.
The integral is taken along the particle flight path.
The values of a and b should be variable.
The pronumeral x is the radial distance from the optic axis of the 90° magnet.

The entrance trim magnet uses pole-face windings on the inner faces of the field clamp. Mirror sets of coils were attached to water cooled copper plates inserted between the field clamp and vacuum can at the entrance of the 90° magnet. The exit trim magnet is similar to the laboratory's one degree steering magnets with the pole tips machined to resemble a quadratic function.

The magnetic fields produced by the trim coils were measured with a Bell model 640 Hall effect gaussmeter. In all cases, the line integral $\int B \cdot d\ell$ is within 5% of the desired shape, with no quadrupole component present. The effect of the trim magnets in restoring the focal plane shape and orientation is shown in Fig. C1-6.

e. Focal Plane Detection

Large area position sensitive particle detection can be achieved by a variety of methods. At this laboratory, the detection device chosen was the position sensitive proportional chamber. This choice was governed by factors such as count rate capability, prompt readout, reliability, cost, and flexibility in design.

Although development work was mostly devoted to the multiwire proportional chamber with a cathode delay line readout, the first detector used in the spectrometer was the charge division proportional chamber (CDPC). This detector used a resistive anode (.4 mil Nichrome wire) to divide the avalanche charge pulse in a manner similar to the simple D.C. current divider. Relative pulse amplitudes at the anode ends were converted to position by an on-line computer. The observed resolution depended heavily on such things

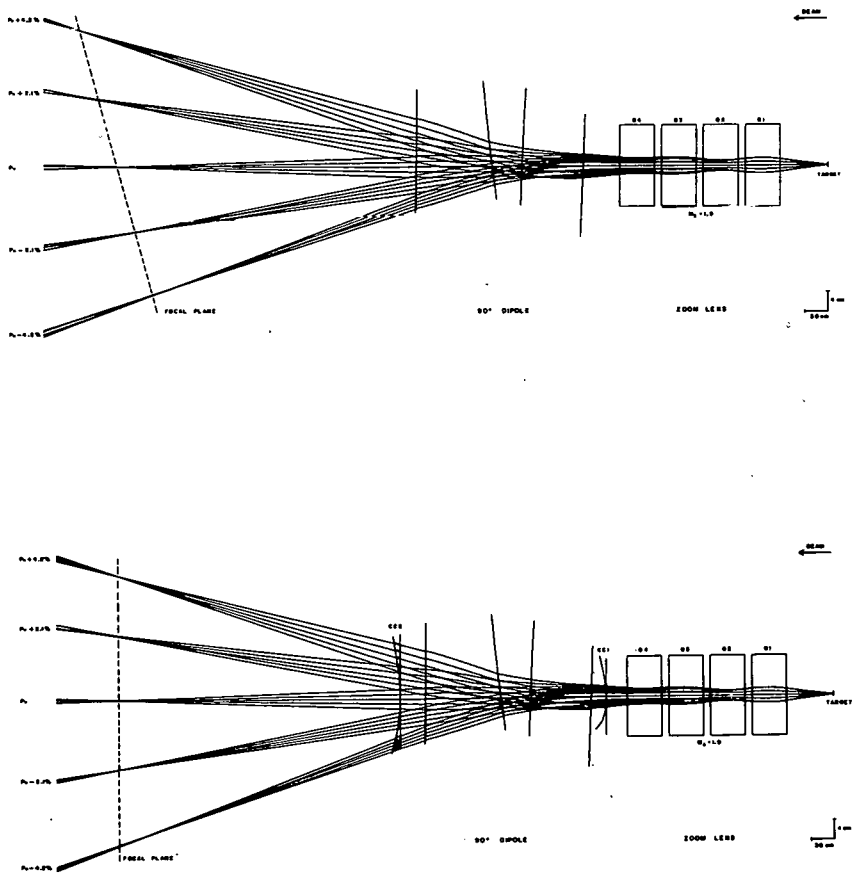

Fig. C1-6 Particle trajectories from the target to the focal surface of the spectrograph for momenta P_o, $P_o \pm 2.1\%$ and $P_o \pm 4.2\%$ with a zoom lens magnification of 1.9. With the trim magnets (cc1 and cc2) installed, the focal surface is restored to a plane at 70° as shown in the lower portion of the figure.

as cable noise, ground loops, amplifier time constants, etc. Once, the resolution observed in the focal plane equaled 0.7 mm, after removing the optics contribution. Usually the detector resolution was no better than 2 mm. This detector was used from April to June.

The multiwire proportional chamber (MWPC) with helical delay line output was first used in June. Its performance indicated this type of proportional chamber to be well-suited to our needs. The first detector featured an active length of about 25 cm. Pre-amp cable drivers on the helix (delay line) ends allowed remote signal processing. A longer detector was installed in August. This detector is sketched in cutaway perspective in Fig. C1-7. This MWPC has an active length (window limited) of

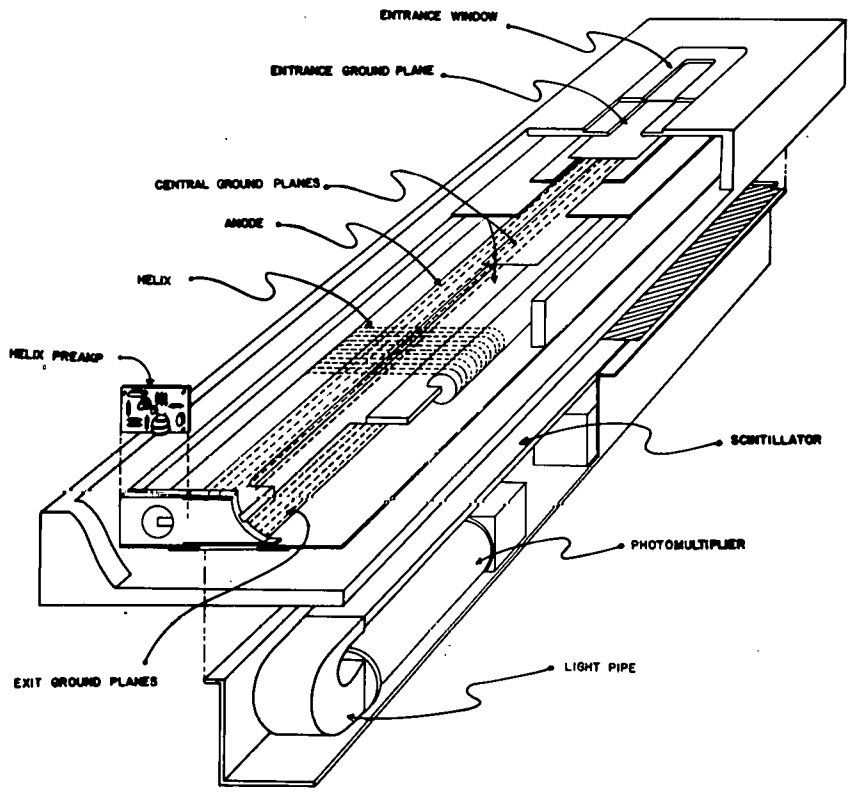

MULTIWIRE PROPORTIONAL CHAMBER

Fig. C1-7 Cutaway perspective of the multiwire proportional chamber.

62.3 cm, and a width of 3.8 cm. Signals due to the avalanche are induced on the helix and then divide to propagate to the helix ends. The relative delay in pulse arrival times is proportional to the position of the avalanche relative to the center of the helix. Fig. C1-8 shows a block diagram of the electronics. A delay, equal to the one-way delay time of the helix (about 1 μsec for the 62 cm. detector), is introduced in the "stop" timing signal so that the position of the avalanche is relative to one end of the anode instead of the center. A count rate of 10^4 per second does not affect the resolution of this detector. An operating voltage of less than 5 KV is adequate for the detection of any reaction product available at this laboratory. With leading edge timing, resolutions of less than 0.5 mm. are easily achieved with a ^{55}Fe 5.9 keV x-ray source. The best overall spectrometer resolution seen is about 0.9 mm, which includes all contributions (e.g. optics + target + detector).

The MWPC was designed as a ΔE or transmission detector. Because of background due to the proximity of the MWPC to beam lines

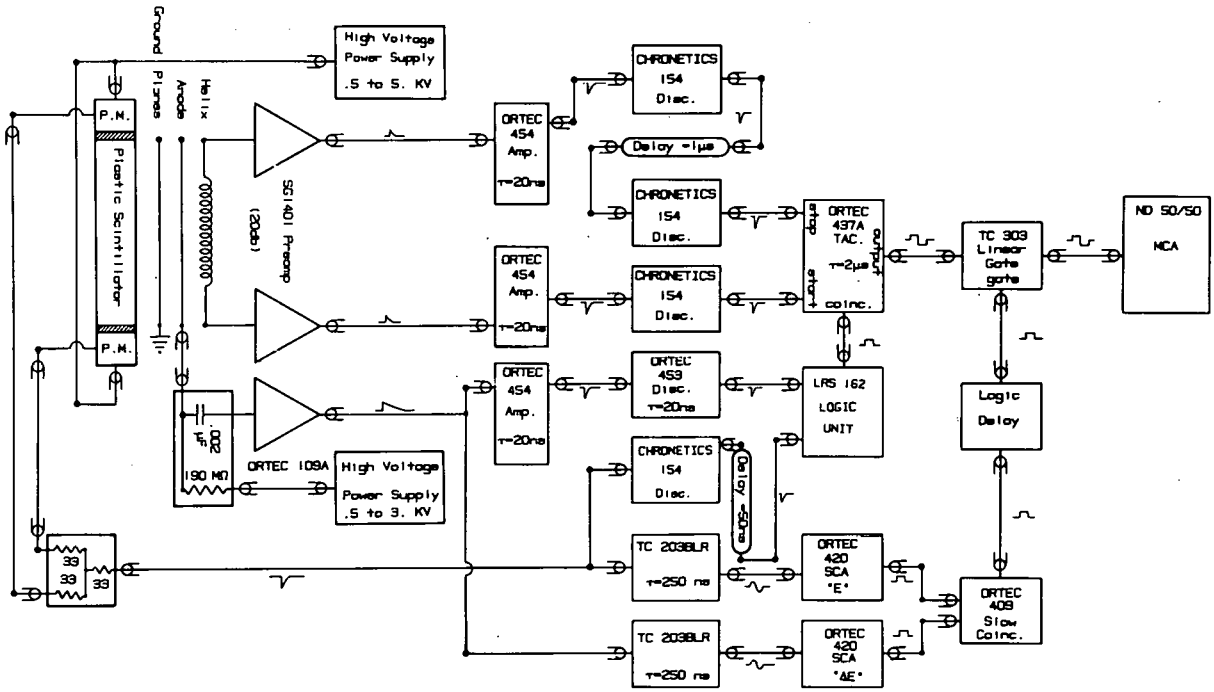

Block Diagram of Electronics in Sept. 1973

Fig. C1-8 Block diagram of the electronics for the multiwire proportional chamber.

and to the Faraday cup, a coincidence detector is advantageous. If this coincidence detector is also an E detector, particle identification is also available. These features are achieved by using a simple plastic scintillator with a phototube at each end. The "thickness" of the 62 cm. MWPC is nearly 60 mg/cm^2 (equivalent carbon). A new 62 cm. MWPC is being constructed with a thickness less than 10 mg/cm^2, which will truly qualify as a transmission detector for nearly every reaction product of interest at this laboratory.

The filling gas used is propane (bottle gas). It has been used exclusively in the MWPC and CDPC detectors. Gains of several times 10^5 can be achieved with stable operation. In addition, this gas works well in the pressure range 0.1 to 1.0 atmospheres. Pulse height resolution on the anode signal of 20% has been observed for gains between 10^3 and 10^5. No performance degradation has been associated with this gas to date.

The anode signal is proportional to ΔE, the energy lost in the anode region. The value of ΔE is nearly proportional to Z^2A/E. At any particular position in the focal plane, the value AE/Z^2 is a constant. Therefore, at any particular position in the focal plane, ΔE is nearly dependent only on A^2. This result is only approximately

valid, and applies only when the projectile energy is greater than about twice the minimum energy needed to traverse the anode region. For the thick (60 mg/cm^2) detector, this is about 3 MeV for protons.

The scintillator signal is nearly proportional to $E/Z\sqrt{A}$, where E is the projectile energy after passage through the MWPC detector. The factor $Z\sqrt{A}$ tends to compensate for scintillator response functions due to ionization density and recombination effects. For different particles with the same magnetic rigidity, the scintillator signal is nearly proportional to $Z/A^{3/2}$.

With these two "rules of thumb", namely

$$\text{Anode Signal} \propto A^2$$
$$\text{Scintillator Signal} \propto Z/A^{3/2}$$

particle identification can be accomplished for many different light reaction products. Note that with an anode signal resolution of 30%, projectile pairs of masses 9 & 10, 10 & 11, etc. can not be distinguished. Note also that with a scintillator signal resolution of 10% that (^{9}Be, ^{10}B) can not be distinguished. Using both anode and scintillator signals, with respective resolutions of 30% and 10%, particle identification can possibly be accomplished for particles of masses up to mass 9. Plotted in Fig. C1-9 are anode and scintillator pulse height spectra for protons, deuterons, and tritons from a ^{107}Ag target, with protons of 26.6 MeV. (These particles do not have the same momentum.)

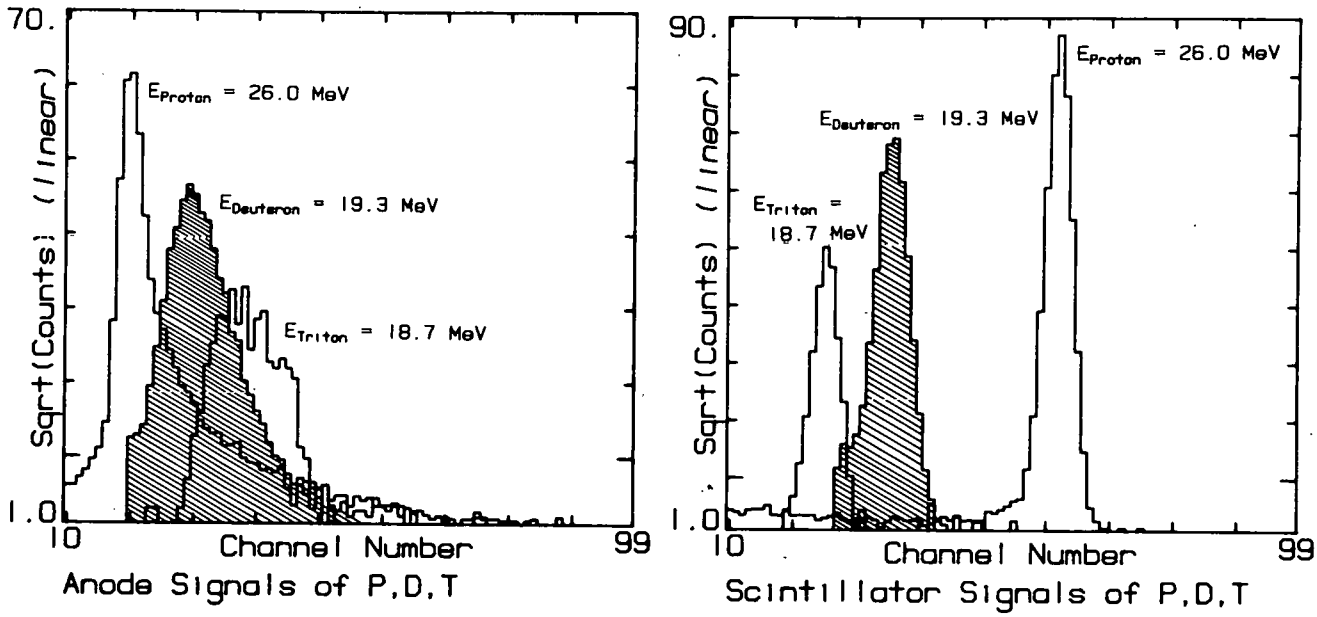

Fig. C1-9 Anode and scintillator pulse height spectra for protons, deuterons, and tritons.

f. Experimental Results

The initial phase of the charged particle program has been oriented towards the acquisiton of experience with a broad variety of reactions and particle energies. Some results of nuclear physics interest have also been achieved, and are presented elsewhere in this and other sections.

Energy spectra of reaction products have been obtained for the following reactions:

(p,p') on targets of ^{40}Ca, ^{58}Ni, ^{197}Au, at E_p=22.8 MeV
(p,d) on targets of ^{106}Pd, ^{107}Ag, ^{209}Bi at E_p=22.8 MeV
(p,t) on targets of ^{106}Pd, ^{107}Ag at E_p=26.6 MeV
(^{3}He,t) on targets of ^{27}Al, ^{46}Ti, ^{107}Ag at $E_{^3He}$=37.7 MeV

The first order energy resolution of the spectrometer with a 5 mm. diameter entrance aperture is predicted to be $\Delta E \approx 3.4 \times 10^{-4} \times E_1$, where E_1 is the primary beam energy. In most cases, the observed line widths are accountable by the first order spectrometer resolution plus target thickness effects and kinematic broadening. No indication of aberrations in the spectrometer has yet been observed. All of the spectra were obtained with the MWPC in coincidence with a backup scintillation counter. The contribution to line width due to the spatial resolution of the MWPC was negligible. Some typical line widths have been observed to be 9 keV FWHM for $^{209}Bi(p,p)$ at 23 MeV, 12 keV for $^{107}Ag(p,t)$ at 26 MeV, and 10 keV for $^{107}Ag(p,d)$ at 23 MeV. Sample spectra are shown in Fig. C1-10.

The signal-to-background ratio has generally been excellent for those instances where the reaction products of interest have greater magnetic rigidity than elastically scattered particles. Particle identification using the MWPC anode signal and the backup scintillator signal has been very clean. Some difficulty has been experienced with background for relatively low energy reaction products. This situation will be remedied by the completion of a shielding cave around the focal plane detector area.

Particularly encouraging has been the high quality of energy spectra obtained at a scattering angle of 2.5°. The ability to observe reactions at scattering angles down to 0° was a significant design feature of the instrument.

g. Present Status and Expected Improvements

The magnetic spectrograph system is now operational. Many experiments have been performed with excellent results. However, there are some improvements planned which should provide users with more flexibility than is now available. These are described in the next three sections.

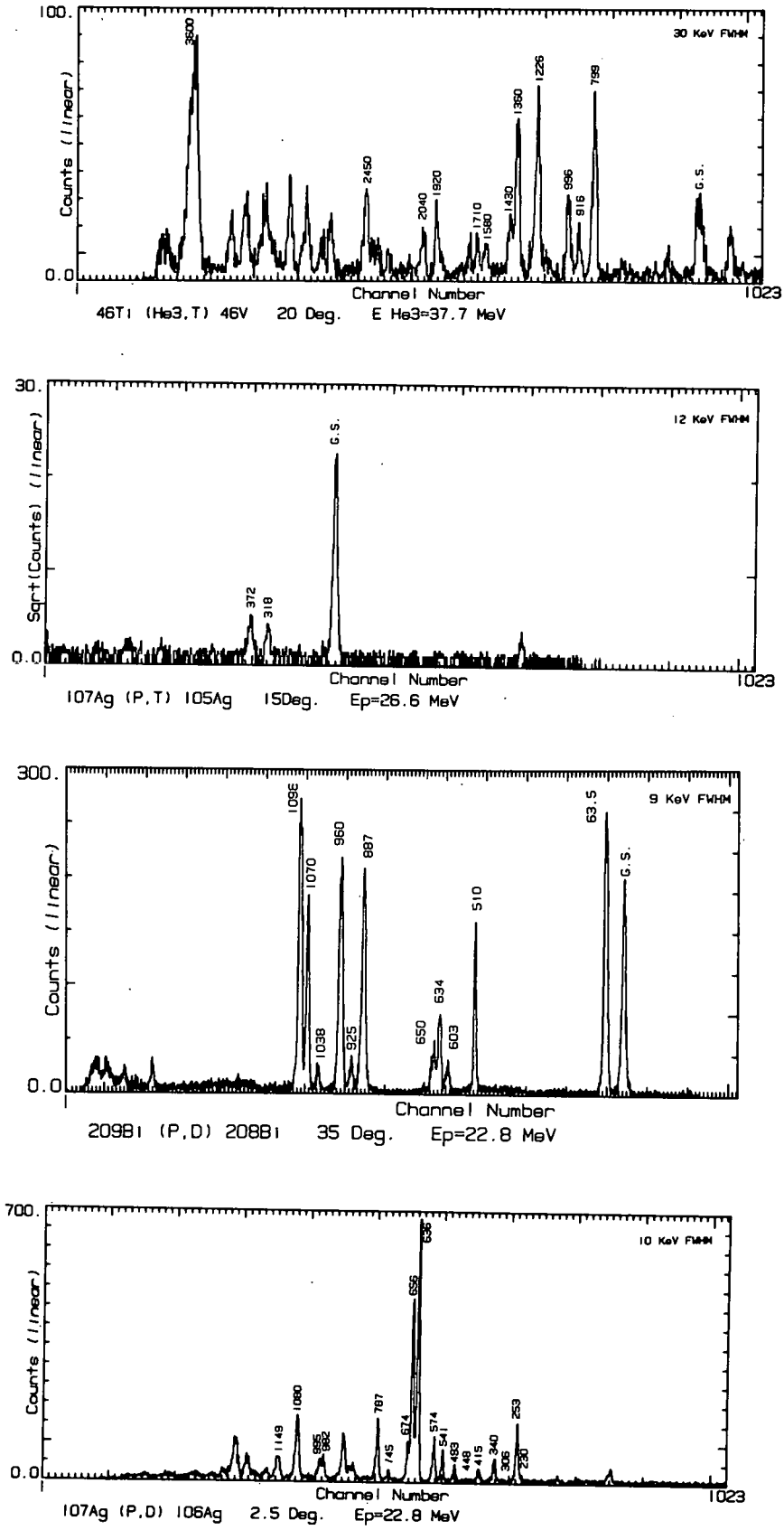

Fig. C1-10 Sample spectra taken with the magnetic spectrograph. Energies are in keV.

i. Scattering Chamber

At present two separate scattering chambers, one for charged particle measurements, the other for neutron TOF experiments, are required. The chamber used with the charged particle spectrograph limits the available scattering angle to the range -10° to +70° and is too small to accommodate a solid state monitor detector. A sliding foil type of chamber 24 inches in diameter and covering scattering angles from -90° to +135° is presently being designed. This chamber will be suitable both for charged particle and neutron time-of-flight experiments.

ii. Electrostatic Deflection Plates

Particle identification based only on pulse amplitudes from the MWPC and the scintillator has been shown to be marginal for particles with $A \gtrsim 7$. There will be no scintillator signals in coincidence with the heavy ions as almost none of them will make it through the MWPC.

Particle identification for these cases can be achieved with electrostatic deflection plates. The plates have been designed and are now being made. The one-half inch aluminum plates will be located in the transition section at the exit end of the 90° analyzing magnet. They will be separated by four centimeters with a maximum of ±20 kv applied. For the worst possible case, there should be a horizontal separation of 28 mm. between the centroids of two different particle groups.

To use the deflection plates for particle identification, the MWPC must be position sensitive in the horizontal plane as well as the vertical plane. This requires slight modifications to the detector presently being used.

iii. Acceptance Solid Angle Delimitation with Slits

The transverse acceptance angle of the spectrometer has been measured by observing the kinematic broadening of protons on protons: H(p,p)H. The measured FWHM value of this $\overline{\Delta\theta}$, the average transverse acceptance, is about 12 mr. This is also the expected value. This often yields unacceptably large kinematic broadening effects for low mass targets and heavier projectiles in experiments such as $^{40}Ca(\alpha,\alpha')^{40}Ca$. This can be corrected by careful placement of adjustable slits.

Beam transport calculations have revealed that at the exit of the third zoom lens quadrupole the transverse displacement of the particles is proportional only to their initial transverse divergence (i.e. the transverse magnification is zero). A slit at this point would effectively control the value $\overline{\Delta\theta}$ seen by the spectrometer. A detailed design is presently being developed.

---

[1] University of Colorado, NPL Progress Report (1971) 106.
[2] University of Colorado, NPL Progress Report (1972) 96.
[3] M. J. Levine and P. D. Parker, Phys. Rev. 186 (1969) 1021.

2. Development of Time-of-Flight System - S. D. Schery, H. Fielding, D. A. Lind, and C. D. Zafiratos

a. Beam Swinger

Satisfactory operation of the beam swinger has been demonstrated by accumulation of data for protons at 16, 23, and 26 MeV. It has also been used at 14 MeV for deuterons and at 25 MeV for ^{3}He. Although the beam optics are quite sensitive to the details of the extraction mode and the setting of individual elements, we have been able to make runs of two weeks duration without difficulty. In the single-turn mode the cyclotron is extremely sensitive to shim coil power supply instabilities and to dee voltage regulation. New power supplies are on order and should be installed in a few months. The dee voltage regulator, although good to ±20 volts, needs improvement to ±5 volts or better; particularly when a set of aperture slits are inserted at about turn 10. For certain tunes of the cyclotron a marked improvement in the time width of the target beam is obtained with the slits.

Cyclotron source gating to select one R.F. burst in 4, 6, or 8 cycles has been used. With a 1 in 8 acceptance, currents up to 300 na average current are run while with 1 in 4 currents up to 1.3 μa average have been obtained.

Fig. C2-1 shows spectra for the (d,n) reaction on ^{9}Be and ^{12}C at 14 MeV for a 9.3 meter flight path. Fig. C2-2 shows a ^{12}C(^{3}He,n)^{14}O at 25 MeV for a 9.3 meter path.

b. Detectors

In addition to 8" diameter by 1" thick cells a number of 8" by 2" thick cells for use at 30 meters with energetic neutrons has been fabricated. Thus far tests on their n-γ discrimination and timing performance show them to be equal to the smaller detectors.

A repeat calibration of the 8" by 1 and 2" thick cells was carried out at the tandem facility at Los Alamos Scientific Laboratory using the proton recoil telescope. Good agreement with a previous calibration was obtained and the efficiency measurements were extended to 28 MeV.

c. 30 Meter Flight Path Facility

The 30 meter flight path facility has been completed. It consists of a 32-inch diameter pipe buried in an earthen bunker with an equipment house at the rear. An array of 7 detectors can be mounted on a thermally insulated dolly for insertion into the tube so that up to 6 ft. of earth shielding is provided on all sides. Along the flight path a collimator of steel followed by paraffin collimates the beam over the first 1.4 meters. At 9 meters a 60 cm. concrete wall with a 25 cm. diameter hole defines the beam envelope. At the detector the tube 6.1 meters long and 80 cm. in diameter, surrounded by earth

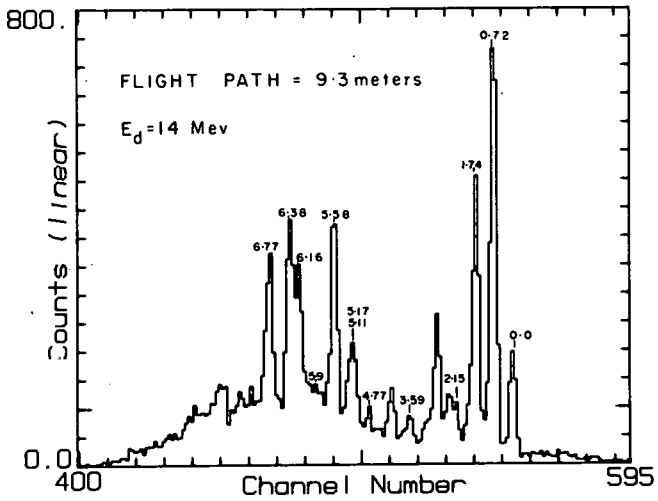

9BE(D,N)10B NEUTRON T.O.F. SPECTRUM AT 31 DEG

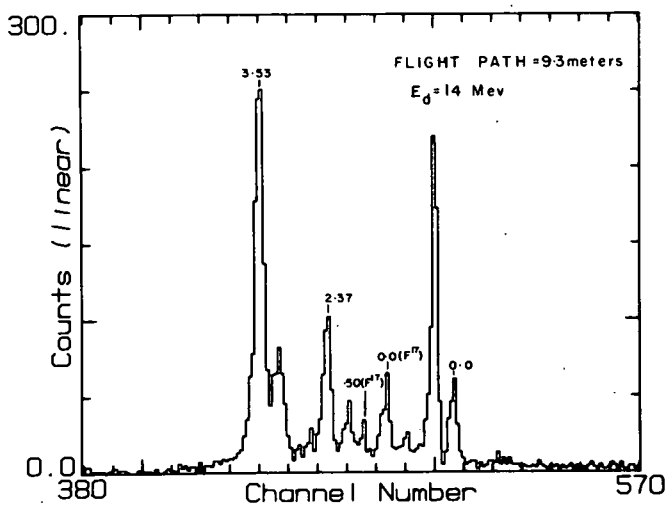

12C(D,N)13N NEUTRON T.O.F. SPECTRUM AT 31 DEG

Fig. C2-1 Time-of-flight spectra for the (d,n) reaction on ^{9}Be and ^{12}C at E_D=14 MeV. The line width is determined largely by the target thickness and kinematic broadening.

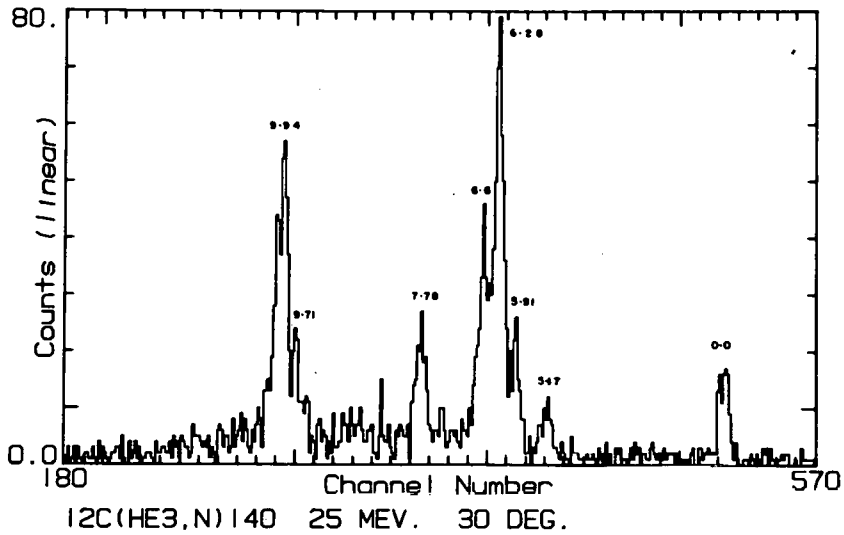

Fig. C2-2 Time-of-flight spectra for $^{12}C(^{3}He,n)^{14}O$ reaction at 25 MeV over a 9.3 meter flight path.

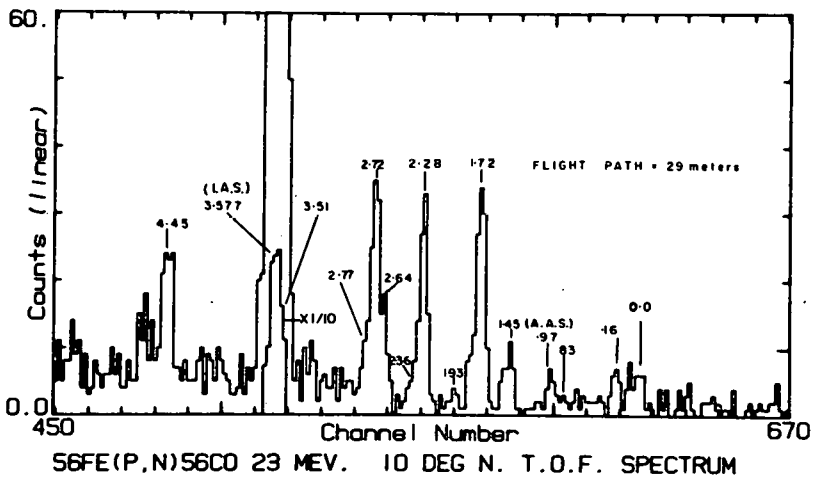

Fig. C2-3 Time-of-flight spectra for $^{56}Fe(p,n)^{56}Co$ over a 29 meter flight path E_p=22.8 MeV.

shields the detector array. The primary neutron beam does not impinge on the detector shield at any point.

Tests with a single 8-inch diameter by 1-inch thick detector have been carried out. Fig. C2-3 shows a spectrum for $^{56}Fe(p,n)^{56}Co$. The resolution for this flight path remains about 1 ns under experimental conditions with small kinematic broadening. Tests of the background indicate that for even quite long runs the natural time independent background should not be significant. The spectrum of Fig. C2-3 was taken over 3 hours. Neutrons from sources generated by the beam other than the target are thus far negligible.

3. Short Rabbit - M. I. Forsythe and M. J. Fritts

The inability of the present astro vault irradiation target holder to allow experiments to be performed on elements with short half lives prompted the construction of a compressed air operated "short rabbit". The present "Astro" system precluded any element with a half-life less than 2-2.5 minutes because of the inherent delay time between cessation of irradiation and commencement of counting.

The "rabbit" (see previous annual Technical Progress Reports) was also found unsuitable because of the necessity of passing the beam through Havar foils. The energies needed in the astro project range from 0.25 MeV to a maximum of 4.0 MeV and with Havar foil (thickness $\approx$ 21 mg/cm^2) corresponding to the range of a proton of energy $\approx$2.7 MeV, it was found necessary to exclude any type of window.

The new "short rabbit" system, therefore, places the target directly in the beam and then extracts it approximately 6" from the target box to be counted, all by means of a double acting piston. The target box used by the "short rabbit" is the one nearest the cyclotron fitted with eight 8.25" lucite flanges, two per side with the beam running the length. The two flanges farthest from the machine on the east and west sides of the base hold the assembly.

On the eastern flange is connected about 7" of rectangular waveguide (brass) capped on the end by a brass flange. This is the counting chamber and use is made for either coincidence or singles counting. To this capping flange is connected a bearing and vacuum seal flange fitted with O-rings. A cylinder, about 13" in length, is connected to this bearing flange. A 3/8" steel shaft connected to an O-ringed piston extends through to the west side of the target box where another bearing and vacuum seal is located.

Fig. C3-1 illustrates the "short rabbit" in place in the target box.

The target holder is a rectangular block of 1/4" aluminum with a 1" square milled in the center into which fits the target

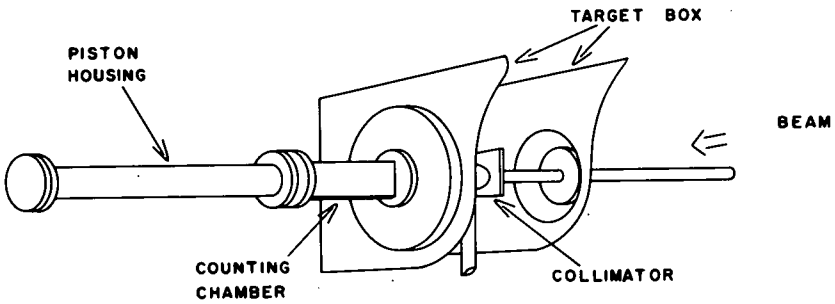

SHORT RABBIT

Fig. C3-1 Schematic of assembled "short rabbit" and collimator. In use, one or two shielded detectors are positioned about the counting chamber.

sandwiched between copper plates. To facilitate target removal, the target holder itself can be detached from its mount, which is screwed onto the shaft. At the limit of the in-stroke, the target is in the beam and at the out-stroke limit, it is about 6" into the waveguide. The total drive distance of the piston is 11.75" and the travel time somewhat less than one second in each direction, depending on the air pressure used.

From the flange underneath the target holder, a water-cooled graphite faced collimator has been inserted. The phosphor coated graphite is backed by a brass plate and set off from the beam at an angle of 45° to allow for TV observation. It contains a 1/4" aperture. Connected to the brass plate is 3" of brass pipe containing an annular magnet (Permag, Texas) and an insulated and biased anti-scattering slit with an 11/32" aperture.

The target holder is shown in position in the mount in Fig. C3-2, with a target in place between the upper plates with circular apertures. The collimator is at the right.

The bearing lubricant is APIEZON vacuum grease and oil and an oil mister provides piston/cylinder lubrication. The timing is controlled by the "rabbit" pin electronics connected to a relay which in turn controls an Avco 4-way valve. The irradiate cycle of the rabbit is driven by the "pin" air from the standard system. In order to accommodate the approximately 1 sec. transit time, a 2 sec. (1.92 sec) delay was introduced into the irradiate cycle.

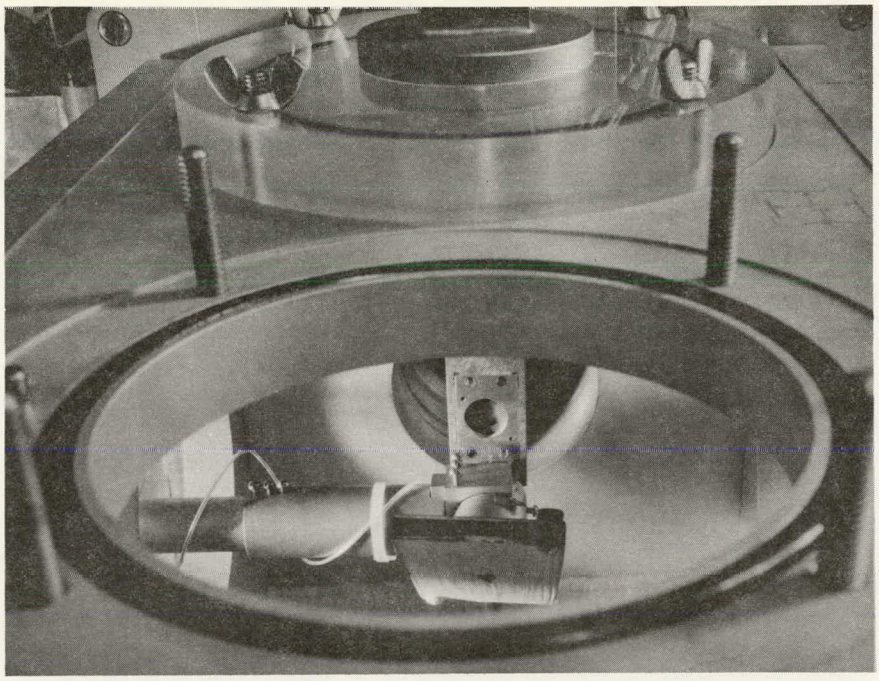

Fig. C3-2 View of the target holder, mount, and collimator system.

To prevent any rotation of the target holder a keying system is set up on the shaft extending from the west side of the target box.

Beam energy measurements are made as usual, merely removing the target sandwich holder, placing the target mount in the irradiate position, and removing the collimator.

4. A High-Pressure Gas Rabbit - M. J. Fritts

A new refillable high-pressure gas rabbit has been constructed for use as a target in the standard pneumatic rabbit system. The design incorporates several features desirable for experiments using gas targets. The path length of the beam in the gas is near optimum, 0.540", with the present foil mounts (84% of the .645" available in a normal rabbit). Gas pressures up to 7 atm. have been obtained using 0.2 mil Havar foils, and a 4 atm. rabbit has been used for over 150 hours without failure with 2 μa of 18 MeV protons and a transit time of 0.400 sec. Scattering from the walls of the chamber is minimized by using a large diameter cell, .390". The large diameter also permits the optical insertion of a polyethene lining with the current rabbit collimation. The rabbit is filled through a small-volume calibrated pumping system which screws

into a small valve at one end of the rabbit. The target may be pumped in stages to attain high pressures, with a nearly 10 to 1 increase in pressure for the initial pumping. Insertion of a lining would of course improve the pumping ratio.

A good deal of effort was expended in an attempt to make the gas target flexible and easy to use. Foils may be mounted on standard 1/4-20 or 5/16-18 washers after suitable drilling and counterboring. Jigs are available for all the drilling, sanding, and boring operations needed. The only restrictions imposed on the foil mounts are the bolt circle and maximum diameter of the foil, making changes in design fairly easy. Foils may be soldered, epoxied, or clamped in place. The best technique found thus far for Havar foils is to soft solder them in place with pure indium over a hotplate.

Fig. C4-1 shows the rabbit and the pumping system. In pumping, the rabbit valve is screwed onto the pump, the retaining ring removed after the rabbit is clamped in place, and the valve pulled

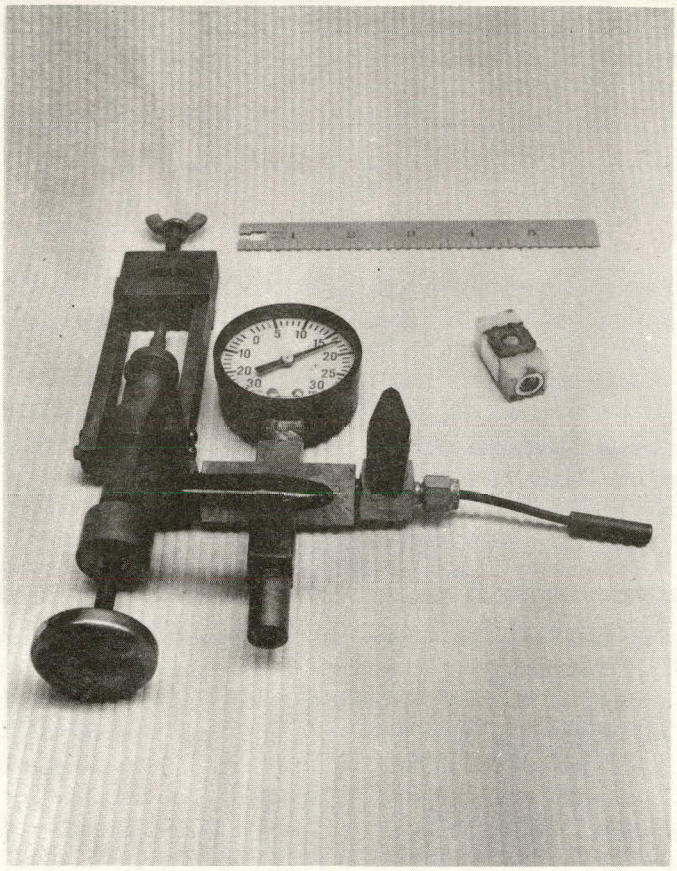

Fig. C4-1 The gas rabbit is shown with the filling valve toward the viewer. The pumping system is shown at left.

slightly out to unseat the O-ring. After the target is evacuated, gas is let into the manifold, pump and target and the initial pressure recorded. The pump is then sealed off, and the desired pressure obtained by tuning the calibrated screw which drives the piston. The target is then sealed and removed.

Beta-delayed γ-spectra following the $^{36}Ar(p,n)^{36}K$ reaction at 18 MeV using this gas rabbit are given elsewhere in this report.

5. Fast Neutron Beam - F. M. Edwards, J. J. Kraushaar, S. Wilmeth

a. New Beam Line

Beam optics program TRANSPORT was run to determine the best configuration for a new beam focus straight through B2 (see Fig. C5-1). It was determined that if a new quadrupole doublet was

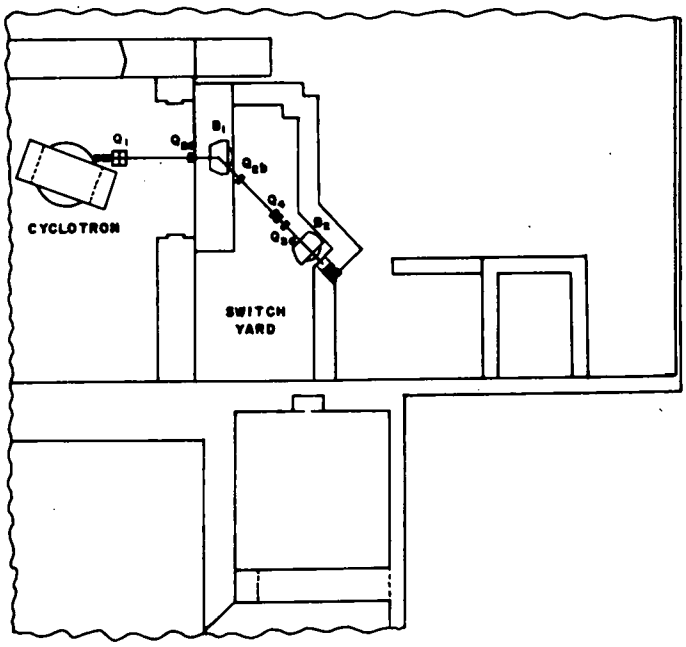

Fig. C5-1 Diagram of beam optics used for fast neutron beam production. Quadrupole doublet Q4 was installed to give a focus at the switchyard wall. The collimator is in the shaded area.

added between existing quadrupoles Q2B and Q3A that a focus could be obtained without physically altering existing beam lines. This quadrupole (labelled Q4 in Fig. C5-1) has been installed and 90% transmission of extracted beam has been obtained. Currents of up to 10 μamps of 17.4 MeV deuterons have been obtained at the focus

which is approximately 30 cm. beyond B2. At present the extracted beam current is limited by power on the deflector septum and it is expected that higher currents will be obtained with the development of a better cyclotron tune.

b. Collimator

It appeared from published reports that steel is the best material for primary neutron collimation. Thus a steel collimator designed to accept inner collimation inserts was constructed. It consists essentially of a cube 20 inches on a side constructed of steel blocks to allow convenient disassembly. The collimator is positioned in the switchyard wall (shown as the shaded are in Fig. C5-1) to take advantage of the switchyard for additional shielding. Work is currently in progress for the design of the inner collimator.

c. Targets

Most existing fast neutron beams use the ^{9}Be(d,n) reaction. However a recent article[1] proposed that a deuterium gas target may in fact yield a more desirable beam. We have designed and built a high pressure deuterium gas cell and are currently testing and comparing it to the more conventional ^{9}Be target. Unnormalized dose data taken in a tissue equivalent phantom indicate a higher dose rate and greater 50% dose depth for the deuterium target. Preliminary neutron time-of-flight data (see below) also indicate that the thick deuterium target is preferable to ^{9}Be. Another advantage of the deuterium target is the sharp forward peak of the resulting neutron beam. This greatly reduces shielding problems (i.e. shielding unwanted large angle neutrons) which are present in thick Be targets.

d. Time-of-Flight Thick Target Yield and Spectra Studies

In order to study and compare thick deuterium and beryllium targets we are developing a pulsed deuteron tune for time-of-flight studies (see TOF section of progress report). We have recently obtained a 14 MeV deuteron tune for this purpose, and further work in this area is in progress. Preliminary results comparing thick target yields and spectra for 14 MeV incident deuterons are shown in Fig. C5-2 for both targets. Due to energy loss in the target window the beam energy on the deuterium target is 13.3 MeV, while the beam energy on the ^{9}Be is the full 14 MeV. The spectra shown are counts vs. flight time (with an approximate energy scale given also), uncorrected for detector efficiency. The spectra are shown for two detector bias levels, 1 x ^{60}Co which gives a low energy cutoff of $E_n \sim 3$ MeV and 2 x ^{60}Co which gives a cutoff of $E_n \sim 5$ MeV. It is easily seen that the deuterium target has its peak at a higher energy than the beryllium. Analysis of this data and further experiments are underway.

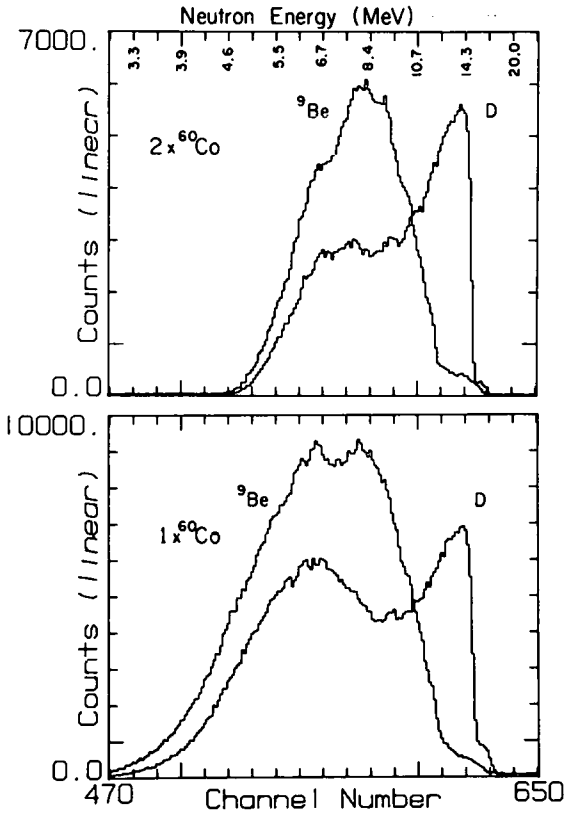

C5-2 Thick target neutron spectra for 14 MeV deuterons on ^{9}Be and 13.3 MeV deuterons on deuterium obtained by time-of-flight methods. Channel number is proportional to flight time. An approximate neutron energy scale is also shown. Detector bias levels are set relative to a ^{60}Co source, the 1 x ^{60}Co bias level does not detect neutrons below ~ 3 MeV, the 2 x ^{60}Co does not detect neutrons below ~ 5 MeV. Spectra are not corrected for detector efficiency.

e. Work in Progress

The fast neutron beam facility will in the future months undertake the following: first, complete the TOF studies to determine the optimum target for our cyclotron. Second, completely determine the physical properties of the neutron beam as they relate to biological and clinical use. This includes dosimetry and dose depth properties, calibration of dose vs. charge on target and similar studies. Third, continue in cooperative efforts which have been initiated with the C.U. Medical School and the Veterinary School at Colorado State University. In particular, we expect to begin animal irradiations before the end of the year.

---

[1] Batra et al., Nucl. Inst. & Meth. 100 (1972) 135-139.

6. Computer Program Development

a. OPTICS - D. E. Prull

A program to calculate the current required in the beam transport elements on the various beam lines has been written for the PDP-9 computer. The calculations are based on magnetic field mapping data and the first-order beam optics design parameters. Relativistic kinematics are included in the laboratory's beam swinger and magnetic spectrometer, since the dispersion matching conditions are based on the reaction being studied.

b. SPECTR - D. E. Prull

A software problem in the VP09 display handlers was causing an interaction between the display and the real time clock. The movable cursors used in interactive data reduction would disappear when the time option of SPECTR was used. The problem was corrected by a minor change in the system's resident monitor, since changing the display handlers would require modifying and recompiling all the user programs which utilize the display.

c. PEAKFIND - R. L. Bunting

A program to locate peaks in gamma-ray and charged particle spectra has been developed for use on the PDP-9 computer. The peak location subroutine is primarily that due to M. A. Mariscotti[1] while the peak parameters are specified according to B. Nyman.[2] No least-squares fitting is attempted in the present version since memory requirements already necessitate an overlay structure for the program. The length of the input spectrum is unrestricted, but the total spectrum is analyzed in units of 1024 channels. Execution time with the program and input data stored on DECTAPE is approximately 30 seconds for 1024 channels. The execution time is considerably less when the program is transferred to a resident disk-pack.

---

[1] M. A. Mariscotti, Nucl. Inst. & Meth. 50 (1967) 309-320.
[2] B. Nyman, Nucl. Inst. & Meth. 108 (1973) 237-241.

d. Energy Loss Calculations - R. A. Emigh and C. S. Zaidins

An analytic expression has been developed for use in the analysis of thick target yields for dE/d(px). This expression has now been applied to the general problem of energy loss in matter. There are a number of applications in which the target or foil is too thick for use of a linear approximation to the energy loss, but yet the particle does not stop in the foil. We have written a program to calculate the energy loss and range of charged particles in a foil of a given material and thickness.

The key ingredient to the method is that we have both an analytic expression for the stopping power

$$\frac{dE}{d(px)} = \frac{C(1-e^{-\alpha E})}{E^{3/4}}$$

which is good to within 5% on the average of the values tabulated in Williamson, Boujot, and Picard (CEA-R3042, Saclay, France, 1966) and an expression for the range, R, which agrees within 2.5% of a numerical integration for the dE/d(px) expression

$$R(E) = \frac{0.585}{C} \frac{E^{7/4}}{1-e^{-3/7\alpha E}} .$$

From these formulae the energy loss, ΔE, is calculated by the following scheme. First the range, R(E), of the incident energy must exceed the thickness, TM. If this is not true, then the particle will stop in the foil and only the range is calculated. If the particle does exit from the foil, it will have an exit energy, EE, which is what we wish to calculate since $EE + \Delta E = E$. However, we know that the range of the exiting particle, R(EE) is related to that of the original energy, R(E), by the expression

$$R(E)-R(EE)=TH. \qquad (1)$$

We then find EE by solving the transcendental equation (1) for EE.

The program is used as follows. The input needed first is the value of the two parameters, C and α. Then the user specifies the incoming particle energy and foil thickness. The program outputs the energy loss, the exit energy, the range of the original energy particle and the range remaining for the exit energy particle. If the thickness exceeds the range, only the range is calculated. Since C and α depend both on the charged particle and target, the program has been written to continue changing energy and thickness for the same C and α until a ↑s starts the program over again and new C and α can be input.

At this time, the values for C and α must be obtained from either tables made up from already calculated fits to the Williamson et al. tables or the Bethe function, or by interpolation of these tables. The parameters C and α can be found by an existing least squares program, FITCAL, over the region of interest, approximately 50 keV to 50 MeV. We have already fit the projectiles p, α, ^{3}He, ^{6}Li, ^{7}Li, ^{7}Be, ^{9}Be, and ^{10}B for a variety of targets from H to U. There are clear trends in both parameters which give good hope that C and α can themselves be fit as a function of Z_1, the projectile charge, A_1, the projectile mass, Z_T, the target charge, and A_T, the target mass. There is a decrease in α with both increasing Z_1 and Z_T, a decrease in C with increasing Z_T, and an increase in C with increasing Z_1 and A_1. We hope to complete the expressions for C and α in the near future, but until then, the interpolations are easily done from the tables that have been computed so far. This technique seems to be a great improvement over the older methods of energy loss calculations.

7. Electronics Maintenance and Development - L. A. Erb

a. Cyclotron

i. Shim Coil Power Supplies

A purchase order has been let to acquire four SCR regulated power supplies. These will be used to replace the existing unregulated shim coil power supplies.

An extensive survey of different supply designs was made and it was found that SCR regulated design gives the best stability per unit price for our application. The design specified closely parallels that used at LAMPF for beam handling magnet excitation.

Construction is under way with CU furnished components to help reduce costs. Delivery is expected later this year.

ii. RF System

The cyclotron RF system has performed well with only minor weekly maintenance. With the development of new single turn tunes for time-of-flight work, it is apparent that better (1 part in 5000) dee voltage regulation is needed.

b. Beam Handling

i. Magnet Interconnections

Additional magnet patch panels have been constructed. These allow more magnets on different beam lines to share a common power supply. This technique obviously reduces power supply costs but unfortunately makes operating the system more complex.

ii. Magnet Current Stability

High voltage shunts have been manufactured and installed in four beamline power supplies to increase the current sense signal to their regulators. Shunt construction is of water cooled manganim and has a resistance close to one milli-ohm.

iii. Swinger Supplies

All the swinger magnet power supplies are now running. Minor modifications will be made occasionally as their requirements become better defined.

A water cooled series load resistor is being completed for the lower resistance 45° magnet. The air cooled resistor now used is creating high ambient air temperatures in the power supply area. Ethylene glycol will be used as a non-corrosive cooling medium to avoid electrolysis effects.

c. Data Processing

Our PDP-9 computer has been operating reliably this past year. An intermittent problem relating to interactions between automatic priority interrupt hardware and software has been solved with a minor software change. Machine usage continues to be quite heavy.

d. Experiment Support

i. Multiple Wire Proportional Counters

Position sensitive multiple wire proportional counters are being developed for the energy-loss spectrometer. High speed delay line amplifiers have been constructed for timing signal processing. Improved chamber design and amplifier rise time has resulted in satisfactory operation. For more details see section II-C-1-e of this report.

ii. Neutron Time-of-Flight

With the advent of the beam swinger, a new 30-meter fixed detector neutron time-of-flight system has been constructed (sect. II-C-2). Instrumentation and power cabling has been installed to the outside detector site.

iii. X-ray Fluorescence System

A PDP-8E computer has been acquired to automate data acquisition for the x-ray fluorescence trace element identification system. Three laboratory devices are being interfaced to the PDP-8E to complete a usable hardware configuration. The first device is a Northern Scientific ADC. A dead time corrected clock is also provided within this interface. The second instrument is an automatic sample changer. It can be either manually operated or can be placed under computer control. Third is a controller for the x-ray tube power supply. This involves sensing and control of power switching circuits, as well as safety interlocks. All these interfaces are constructed in NIM module form to be housed in the computer system rack NIM BIN.

iv. General Purpose NIM Modules

An increase in experiment complexity has required the manufacture of more in-house designed NIM modules. These modules fulfill a need which cannot be provided economically by commercially available modules. They include mostly logic functions such as delays, inverters, "and" and "or" gates, level converters, pulse stretchers, and a ratemeter with an averaged rate discriminator.

D. Cyclotron Operation - A. B. Phillips

Operation for the period 1 September 1972 to 31 August 1973 is covered below. Table D-I shows hours of cyclotron operation by purpose. Table D-II shows hours of cyclotron operation by type of particle accelerated. The 28-hour difference between the totals on the two tables represents time spent in tests of cyclotron components.

TABLE D-I

Hours of Cyclotron Operation - Purpose

Month	Cyclotron Development & Test	Research		Radionuclide Production		Subtotal Hrs/mo.
		Staff	Collaborate	Staff	Outside & Collaborate	
Sept. 72	0 + 28T	287	---	---	---	315
Oct. 72	---	408	7	---	---	415
Nov. 72	---	532	---	---	---	532
Dec. 72	---	311	10	---	---	321
Jan. 73	---	665	---	---	---	665
Feb. 73	---	443	10	---	---	453
Mar. 73	---	638	---	---	---	638
Apr. 73	---	496	9	---	---	505
May 73	---	246	---	---	---	246
June 73	---	520	---	---	---	520
July 73	8 + 0	571	---	---	---	579
Aug. 73	---	607	---	---	---	607
Totals	8 + 28T	5724	36	---	---	5796

TABLE D-II

Hours of Cyclotron Operation - Particle

Month	Protons 0.27/27.6 MeV	Deuterons 3/18 MeV	H_2^+	^3He 14/43 MeV	^4He 12/36 MeV	Other	Sub-Total Hrs/mo.
Sept. 72	244	---	---	43	---	---	287
Oct. 72	251	40	---	124	---	---	415
Nov. 72	337	87	---	108	---	---	532
Dec. 72	196	10	---	105	10	---	321
Jan. 73	360	101	---	199	5	---	665
Feb. 73	159	105	---	179	10	---	453
Mar. 73	428	28	---	137	45	---	638
Apr. 73	318	---	---	33	154	---	505
May 73	208	---	---	---	38	---	246
June 73	412	10	---	68	30	---	520
July 73	480	9	---	73	17	---	579
Aug. 73	352	120	---	85	50	---	607
Totals	3745	510	---	1154	359	---	5768

Of the 8760 hours in the year, the cyclotron was in use for 5768 hours, or 66% of the year. Actual beam-on-target time was 4238 hours, or 73% of cyclotron running time.

Cyclotron runs for outside users were 7 hours for Ball Bros. Research Corp., Boulder, Colorado, and 29 hours for Colorado State University, Ft. Collins, Colorado.

The cyclotron was out of commission for a total of 585 hours, or 6.7% of the year. 255 hours were used for scheduled maintenance, 52 hours for scheduled repairs, and 278 hours for non-scheduled repairs. Of the non-scheduled repairs, 228 hours were for repairs to one of the main diffusion pumps. The imminent pump failure was discovered near the end of the annual maintenance period. During another 142 hours, the cyclotron was ready but not used to allow access for set-up of experiments.

Table D-III is a list of scheduled visitors to the laboratory during the period.

TABLE D-III

Scheduled Visitors - 9/1/72 to 8/31/73

Date	No.	From
10-28-73	30	High school teachers, C. U. conference
11-9-72	9	Strasburg, Colo., High school physics class
11-9-72	30	C.U. Denver Center physics class
11-13-72	20	Sigma Pi Sigma, C.U. physics society
11-15-72	50	C.U. physics 112 class
12-11-72	7	C.U. physics class
12-14-72	7	Colo. Sch. of Mines, Golden, Colo., honors class
2-19-73	8	C.U. Physics Dept., grad student familiarization
3-8-73	15	Nederland, Colo., Jr. and Sr. High School
4-3-73	61	C.U. physics 112 class
4-4-73	21	C.U. class, Intro. Modern Physics
4-13-73	13	Univ. of Wyoming, Laramie, Wyo., physics class
4-16-73	50	C.U. Physical Science 102 class
4-21-73	40	C.U. Denver Center physics class
4-24-73	16	C.U. Health Physics class
5-8-73	30	Boulder High School, Boulder, Colo., physics classes
5-23-73	16	Community College, Denver, college physics class
5-31-73	16	Univ. of No. Colo., Greeley, Colo., physics class
7-27-73	10	Univ. of Wyoming, Laramie, Wyoming
7-31-73	13	Colo. State Univ., Ft. Collins, Radiation Biol. Dept.
8-21-73	40	High school honors students, C.U. summer institute
	502	

E. Outside Users of Cyclotron Facilities

The Nuclear Physics Laboratory has continued to encourage outside groups to make use of the cyclotron facility for educational or research purposes. These uses have included service irradiations, collaborative research, and educational tours of the laboratory.

The cooperative program with the University of Wyoming has continued. Professor R. Kunselman and two graduate students have participated in the short-lived radioisotope studies that are described in this report (II-A-2-i).

Dr. Charles Goodman of Oak Ridge National Laboratory spent the past year as a Visiting Professor in the Department of Physics and Astrophysics and conducted research at the Nuclear Physics Laboratory during this time. During the current year, Professor Martin Rickey of the University of Indiana is a Visiting Professor in the Department of Physics and Astrophysics and will be working at the Nuclear Physics Laboratory.

For the fourth year, outside users of the laboratory facilities included students from the Hispano Summer Program of the Department of Physics and Astrophysics. This program works with selected Hispano students between their sophomore and junior years from Denver's North High School. The goal of the program is to acquaint these students with the possibilities and realities of higher education through a series of seminars, lectures, field trips, and laboratory work for one month. Our participation consisted of supplying lab space and instructors for eight of the students for 20 afternoon lab sessions. Various students and faculty volunteered time for this program.

Professor S. A. Watkins and several advanced physics students from Colorado State College in Pueblo, Colorado, have collaborated in the use of the laboratory's x-ray fluorescence facilities for studying selenium uptake in plants. The results which this group has obtained have been sufficiently encouraging to warrant an expanded program of investigation at their home institution.

Several solar cells were irradiated with protons for Ball Brothers Research Corporation in order to provide a calibration between integrated proton flux and efficiency loss for the solar cells. After this calibration information was obtained, an additional forty-two solar cells were aged by irradiation with a proton flux of sufficient integrated intensity so that the radiation they would experience when used in subsequent space flights would not produce a significant further change in efficiency.

There are, of course, a number of classes that visit the laboratory every year and these visitors are listed in the preceding section of this report.

III. THEORETICAL PROGRAM

A. Pionic Reaction Investigations - E. Rost, P. D. Kunz, and G. W. Edwards

The program of investigating simple nuclear reactions involving pions is continuing and is being extended as the prospect of definitive data from LAMPF becomes imminent.

The simplest reactions, elastic scattering and inelastic pion scattering to collective levels, have been successfully analyzed for the existing ^{12}C experiments by employing optical model techniques. In this past year the computer programs[1] have been refined and generalized so that meson factory experiments can be immediately analyzed.

The more controversial optical-model extension involving single and double charge-exchange scattering exciting analog states has been carefully studied[2] for parameter sensitivity effects for the $^{91}Zr(\pi^+,\pi^\circ)^{91}Nb^*$ reaction. This reaction will be soon measured at LAMPF by looking at delayed proton decay. A somewhat similar reaction, $^{13}C(\pi^+,\pi^\circ)^{13}N$, has been measured recently[3] by looking at the ^{13}N radioactivity (the ground state is the only particle-stable state). The experimental data do not agree at all with the predictions based on the generalized optical model; in particular, the 180 MeV measurement, if correct, would imply no absorbtion, a result at variance with many other experiments. This puzzle has led to some experiments performed at Colorado and described in sect. II-A-3-d of this report.

The analysis of (p,π^+) or (π^+,p) reactions exciting discrete state in terms of a stripping or pickup mechanism has been very exciting since the large momentum transfers involved make these reactions qualitatively different from conventional nuclear physics stripping reactions. This past year has seen a paper published[4] and considerable effort expended in understanding the many parameter sensitivities and generalizations to other energies, targets, reactions, etc. A review paper was presented at a LAMPF summer study session.[5] The computer programs have been developed so that new data can be readily analyzed when available. At present, we are also investigating the (p,π^-) reaction for which some limited data exist in terms of a two-step direct mechanism (stripping plus charge exchange).

---

1 G. W. Edwards, Pionic DWUCK, unpublished computer program.

2 G. W. Edwards, "Study of the $^{91}Zr(\pi^+,\pi^\circ)^{91}Nb^*$ Analog State Total Cross Section from 30 MeV to 300 MeV", unpublished.

3 J. Alster et al, to be published.
D. T. Chivers, E. M. Rimmer, B. W. Allardyce, R. C. Witcomb, J. J. Dominga, and N. W. Tanner, Nucl. Phys. A126 (1969) 129.

4 E. Rost and P. D. Kunz, Phys. Letters 43B (1973) 17.

5 E. Rost, Pion Reactions, Proc. LASL summer school, July, 1973, to be published.

Dup: 70799 J PYLBB

B. Microscopic Calculations of (p,n) Reactions to Isobaric Analog States - L. D. Rickertsen and P. D. Kunz

104-7

Last year[1] we reported preliminary calculations of the (p,n) reaction to isobaric analog states taking into account the two-step process through intermediate deuteron channels as well as the usual charge-exchange. In the past year we have improved these calculations and extended them to a wide range of target nuclei and incident proton energies. The results of many of these calculations are shown in Figs. T1 and T2. The calculated energy dependence of the $^{90}Zr(p,n)$ reaction is shown in Fig. T3. We note that for most cases, the two-step cross section is of the order of magnitude of the data.

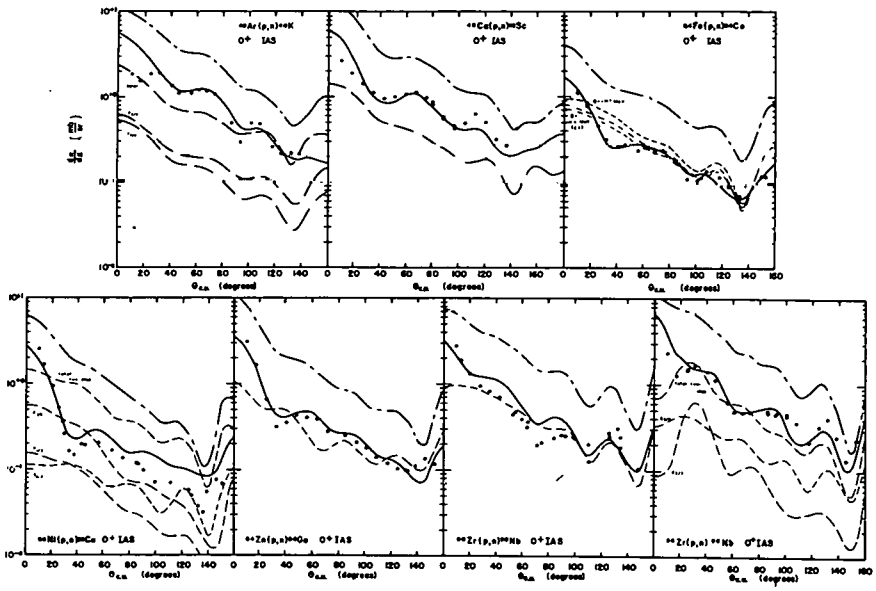

Fig. T1 Calculated angular distributions for (p,n) IAS transitions, A=40-96. Dashed-dot curve for direct-only transition, dashed curves for various two-step transitions and full curves give coherent sums of direct and two-step transitions. E_p=22.8 MeV.

The calculations consist of the solutions to coupled equations with coupling from the proton channel to the neutron and deuteron channels and from the deuteron to the neutron channels, thus nearly corresponding to a second-order Born approximation calculation of the reaction. The Becchetti and Greenlees[2] parametrizations were used for the proton and neutron optical potentials. The optical potentials in the deuteron channels were derived from the adiabatic model of Johnson and Soper.[3] The calculations for A ≥ 96 seen as solid curves in Fig. T2 have been performed by artificially binding the protons in the residual nucleus by 0.1 MeV. The spectroscopic factors for coupling strengths to the deuteron states are given by agreement to experimental (p,d) data. We have found that the differences in excitation of the deuteron states do not have much effect on the final cross sections and that very similar results

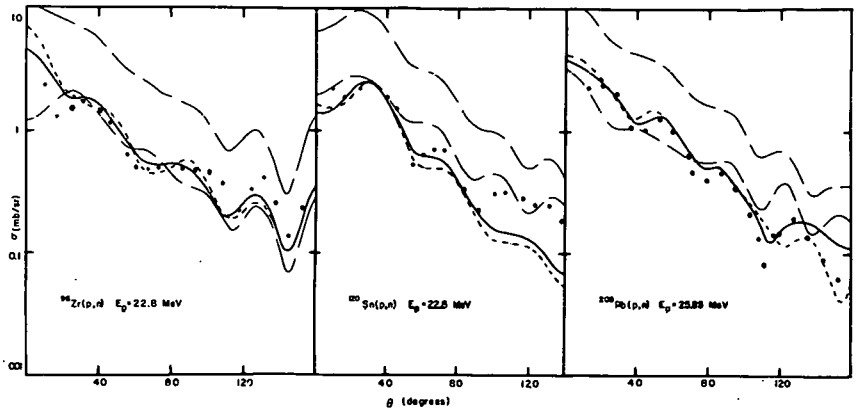

Fig. T2 Calculated angular distributions for (p,n) IAS transitions A=96-208. Dotted curve is result of calculation using resonance form factors. Full curve is coherent (p,n) cross section binding final proton by 0.1 MeV. Upper and lower dashed curves correspond to direct and two-step cross sections, respectively, for bound form factors.

may be obtained by taking the summed two-step spectroscopic strength through a single deuteron state. The coupling from the elastic channel to the isobaric analog channel is proportional to the strength of the charge-exchange part of the effective two-nucleon interaction (here taken to be of Yukawa form with a range of 1 F). The resulting strengths are much more consistent than when the two-step mechanism is ignored and are given in Table T-I. In addition, the energy dependence of these strengths is substantially reduced when the two-step process is explicitly included, as seen in Table T-I for both the ^{90}Zr(p,n) and ^{120}Sn(p,n) reactions.

Recently polarization data has been obtained[4] for the (p,n) reaction with behavior not explained in several cases by the usual direct-transition form factors. An attempt has been made[4] to explain this anomalous behavior in terms of a spin-orbit part of the effective two-nucleon interaction. The two-step process through intermediate channels can also have the effect of a spin-dependent force. For example, although the direct charge-exchange on 0^+ targets cannot lead to a projectile spin-flip amplitude, the two-step process does have a spin-flip as well as a non-spin-flip transition amplitude. The effect of the two-step mechanism upon the differential analyzing power is seen in Fig. T4 for ^{60}Ni(p,n) and ^{120}Sn(p,n), the latter case showing a forward angle anomaly which cannot be interpreted in the usual DWBA with spin-independent forces.[4] The calculations for ^{120}Sn(p,n) have been made assuming the protons are bound in ^{120}Sb by 0.1 MeV. Although the final state is quite long-lived (decay width/excitation energy <0.05), the long-ranged tail of the resonance is expected to affect the higher partial waves somewhat and since these manifest spin-orbit influences most strongly, Fig. T4 is expected to change when the unbound nature is treated less

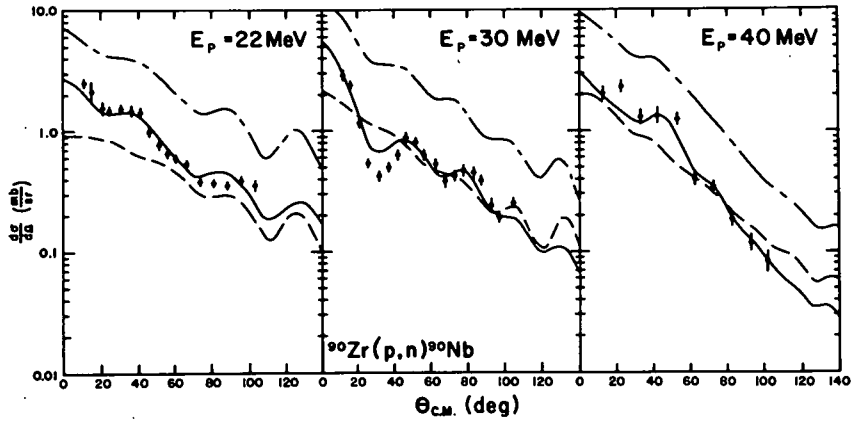

Fig. T3 Energy dependence of (p,n) reaction. Notation same as Fig. T1.

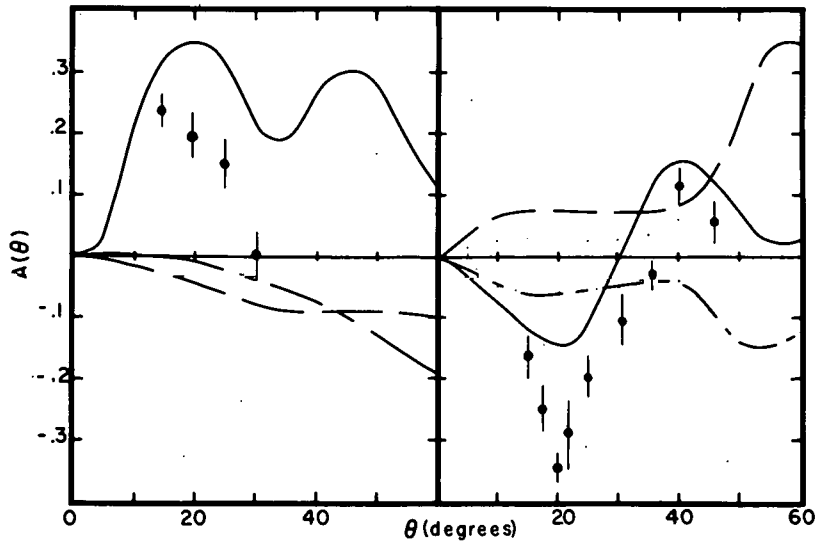

Fig. T4 Differential analyzing power of (p,n) reactions. Dot-dashed curve is result of microscopic charge-exchange transition only, dashed curve is polarization due to two-step process and full curve is the coherent sum of the two. E_p=24.5 MeV. V_τ for both cases taken to be 32 MeV. Left-hand side for $^{60}Ni(p,n)$ and right-hand side for $^{120}Sn(p,n)$.

TABLE T-I

Strengths required for (p,n) IAS transitions. Strengths in column (a) obtained by fitting the data (minimizing χ^2) calculating only the direct transition in DWBA. Those in column (b) obtained by fitting coherent one- and two-step calculations by eye. "Bound" means that residual nuclei are treated as bound. "Unbound" means approximate resonance form factors used in calculations.

Target	E_p (MeV)	V_T (MeV)	
		a) Direct-only Transition	b) Including Two-Step
^{40}Ar	22.8	21.7	40.3±1.0
^{48}Ca	22.8	20.0	33.0±0.5
^{54}Fe	22.8	20.4	32.3±0.5
^{56}Fe	22.9	18.5	33.0±1.3
^{58}Ni	22.8	17.9	33.0±1.2
^{64}Zn	22.8	15.2	32.6±1.0
^{90}Zr	22.0	32.5	35.2±1.0
^{90}Zr	22.8	19.5	33.4±1.0
^{90}Zr	30.0	20.5	30.7±1.0
^{96}Zr	40.0	17.0	30.0±1.0
^{96}Zr (bound)	22.8	16.9	32.8±1.5
^{120}Zr (unbound)	22.8	16.9	32.7±1.5
^{120}Sn (bound)	22.8	17.1	33.8±1.5
^{120}Sn (unbound)	22.8	17.6	34.1±1.5
^{120}Sn (unbound)	25.0	14.7	32.6±1.0
^{208}Sn (unbound)	35.0	11.7	28.8±1.5
^{208}Pb (bound)	25.9	15.8	32.3±1.5
^{208}Pb (unbound)	25.9	15.4	30.5±1.5

approximately. In the calculations we have ignored the deuteron spin-orbit potential which may represent another drawback to these results. The most we can say at present is that it will be difficult to accurately assess spin-orbit effects in the reaction without also properly treating the important multistep processes which contribute.

[1] L. D. Rickertsen and P. D. Kunz, Prog. Report, Univ. of Colo., 1972.
[2] F. D. Becchetti and G. W. Greenlees, Phys. Rev. 182 (1969) 1190.
[3] R. C. Johnson and P. J. R. Soper, Phys. Rev. C 1 (1970) 976.
[4] J. M. Moss et al., Phys. Rev. C 6 (1972) 1698.

C. Microscopic Studies of (p,n) Reactions to Unbound Final States - P. D. Kunz and L. D. Rickertsen

The usual method of treating reactions in the DWBA to an unbound final state in stripping or (p,n) reactions is to rewrite the cross section as an integral over the resonance energy of the unobserved particle, the integrand being an artificial cross section which is calculated in the usual way evaluating a radial integral over a product of distorted waves and a form factor which is the resonance wave function.[1,2] The latter integral is extremely time consuming because of the contributions of the form factor at large radii and often a "convergence factor" is inserted and extrapolated to zero. That is, for stripping

$$T = \lim_{\alpha \to 0} D_o \int d\vec{r}_n \, \chi_p^{-*}(\vec{r}_p) \, F_{\ell j}(\vec{r}_n) \, \chi_d^{+}(\vec{r}_n) \, e^{-\alpha r_n}. \tag{1}$$

Vincent and Fortune[1] have shown that the convergence factor offers no advantages to computation because the integral (1) does not converge uniformly. The integral over the resonance energy can be facilitated by employing, rather than the resonance wave function for $F_{\ell j}$, the resonant part of this function, the so-called Gamow state. (Ref. 2.) However, this introduces even more severe convergence problems in the radial integral (1).

Recently a procedure has been derived[3] for treating the scattering to long-lived resonant states ($\Gamma/E_o \ll 1$, where Γ is the width and E_o is the energy of the resonance) which does not have the convergence problems and does not require an integral over the resonance energy. The method shows the existence of a form factor which plays the same role as the wave function for the transferred particle in the usual DWBA treatment of the scattering to bound states.

In a first approach to this problem we choose a normalized form factor of the form

$$F_{\ell j}(\vec{r}) = N \, \varphi^R_{\ell j}(\vec{r}) \, e^{-\gamma r} \tag{2}$$

where N is the normalization and $\varphi^R_{\ell j}$ is the solution to the Schroedinger eqn. near resonance and is asymptotic to

$$\varphi^R_{\ell j}(\vec{r}) \simeq \frac{\sin(k'r + \delta)}{k'r}. \tag{3}$$

Eqn. (2) has the appearance of leading to a radial integral (1) with a convergence factor except that no attempt is made to take $\gamma \to 0$. In the Schlessinger and Payne approach, the Fourier transform of their form factor is given by

$$\bar{F}_{\ell j}(k) = \frac{\bar{\nu}(k,E_o)[\Delta(k) - 1]}{(E - E_o + i\frac{\Gamma}{2})} \tag{4}$$

where $\bar{\nu}(k,E_o)$ is the solution to an eigenvalue problem corresponding to the Schroedinger eqn. at the resonance and $\Delta(k)$ is a smooth function which is unity over the width of the resonance and which vanishes for

$$|k^2-k_o^2| \geq \frac{2\mu\lambda}{\hbar^2} \tag{5}$$

and where

$$\Gamma < \lambda < E_o \tag{6}$$

The asymptotic scattering is then determined by the poles of (4). In our approximation, we assume that the pole is at the value

$$E_\lambda = E_o + i_\lambda \tag{7}$$

or

$$k_\lambda = k' + i\gamma \tag{8}$$

Hence k' and γ are determined from the width and energy of the resonance. While it is unlikely that (2) is valid on the interior of the nucleus, it may be useful in the asymptotic region.

Fig. T5 compares the results of our form factor and resulting cross sections with those of Schlessinger and Payne for $^{16}O(d,p)^{17}O$

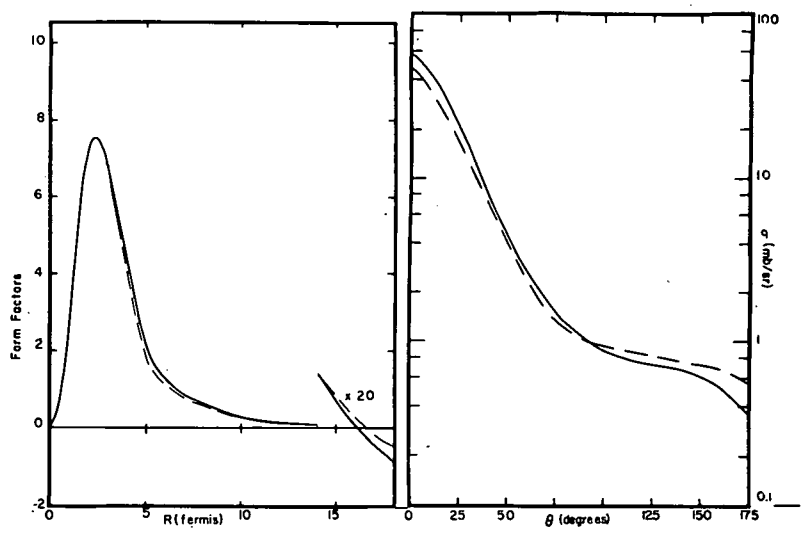

Fig. T5 Resonance form factors and resulting angular distribution for $^{16}O(d,p)^{17}O(3/2^+)$ at E_d=12 MeV. The full curves correspond to the results of Schlessinger and Payne[3]. Dashed curves correspond to calculations using approximate resonance form factor described in text. The parameters are the same as in ref. 3. The spectroscopic factor in both cases is 0.78.

and the agreement is quite exceptional. We have used the same potential as in ref. 2 to calculate the resonant wave function and taken λ a little larger than the geometrical mean of Γ and E_0 for the neutron resonance on ^{16}O. Our resulting binding energy is 1.27 MeV and the damping factor is 0.08 F^{-1}. The results are not sensitive to the value of γ.

With this background we venture to use the approximate form factors in preliminary calculations of (p,n) reactions to the unbound but long-lived analog states of ^{96}Zr, ^{120}Sn, and ^{208}Pb. We have used the approximate resonance wave functions and the appropriate damping factor in the calculation of both the charge-exchange form factor and the stripping form factor for the second leg of the (p,d;d,p) process. The calculations are not sensitive to the precise damping factor used. Large variations in λ within the restrictions of (6) do not change the calculated angular distributions. The results of the unbound calculations with

$$\gamma(^{96}Zr) = 0.05\ F^{-1}$$
$$\gamma(^{120}Sn) = 0.05\ F^{-1}$$
$$\gamma(^{208}Pb) = 0.03\ F^{-1}$$

are shown as dashed curves in Fig. T2 and compared with those which treat the proton in the residual nucleus as bound by 100 keV, seen as the solid curves. In all respects other than the form factors which couple to the analog state the parameters and spectroscopic strengths for the two calculations are taken the same. The resulting charge-exchange strengths are given in Table T-I. At most, these calculations are preliminary and further work is in progress.

---

[1] C. M. Vincent and H. T. Fortune, Phys. Rev. C 2 (1971) 782.
R. Huby and J. R. Mines, Rev. Mod. Phys. 37 (1965) 406.
[2] J. Bang and J. Zimányi, Nucl. Phys. A139 (1969) 534.
W. R. Coker, Phys. Rev. C 7 (1973) 2426.
[3] L. Schlessinger and G. L. Payne, Phys. Rev. C 6 (1972) 2047.

(24,873)

110-4

D. Effective Deuteron Optical Potential in (p,d;d,n) Processes - L. D. Rickertsen

The adiabatic model of Johnson and Soper[1] has shown itself to be useful in the analysis of (d,p) and (p,d) reactions.[2] Moreover, in calculations of (p,d) reactions, we have obtained spectroscopic values which are more consistent with sum rule strengths than those obtained with elastic deuteron optical potentials. For example, Table T-II shows the spectroscopic values we have obtained for the $^{54}Fe(p,d)$ reaction.

The adiabatic model provides an effective optical potential which implicitly accounts for the deuteron break-up states in an approximate way. In (p,n) reactions, the two-step process through intermediate deuteron channels has been shown to be important[3] and it may be necessary to treat the deuteron breakup channels in this

TABLE T-II

Spectroscopic values obtained in the $^{54}Fe(p,d)^{53}Fe$ reaction at E_p=28 MeV. Column (a) obtained from Sherr et al.[5] using deuteron optical model which fits elastic scattering. Column (b) obtained using deuteron parameters derived from adiabatic model of Johnson and Soper.[1]

$^{54}Fe(p,d)^{53}Fe$ Experimental Spectroscopic Factors			
E (Level)	J^{π}	C^2S (a)	C^2S (b)
g.s.	$7/2^-$	4.0	5.1
2.840	$7/2^-$	0.2	0.2
3.321	$7/2^-$	0.4	0.5
4.206	$7/2^-$	1.1	1.9
		5.7	7.7

case as well.

The influence of the (p,d;d,n) amplitude upon the reaction is illustrated in a model calculation shown in Fig. T6. Setting all spin-orbit potentials to zero, we have calculated an $f_{5/2}$ transition on mass 58. The one- and two-step non-spin-flip amplitudes have similar angular dependence and interfere to produce in this case the dashed curve of Fig. T6. Although a spin-flip transition is forbidden for the direct charge-exchange between 0^+ states, a spin-flip amplitude is possible for the two-step process and the resulting cross section is shown as the dotted curve. Because of the strong destructive interference at the non-spin-flip amplitudes and because of the phase difference between the spin-flip and non-spin-flip angular distributions, the weak spin-flip cross section can be important. The incoherent sum of the two amplitudes results in the solid curve. Spin-orbit potentials in the proton and neutron channels can cause mixing of the spin-flip and non-spin-flip amplitudes but calculations including them show that the above arguments are not seriously affected. The spin-orbit potential in the deuteron channel can also mix these amplitudes; and, because this potential alters the mixing due to the two-step mechanism and therefore the coherence of the one- and two-step processes, its effect can be significant. We have found, in fact, for most cases the (p,n) cross sections do not depend very sensitively on the precise deuteron optical parameters employed in the calculation with the exception of the spin-orbit part of the optical potential and it may be possible to use this fact to identify an appropriate set of deuteron parameters.

For a spin-orbit potential

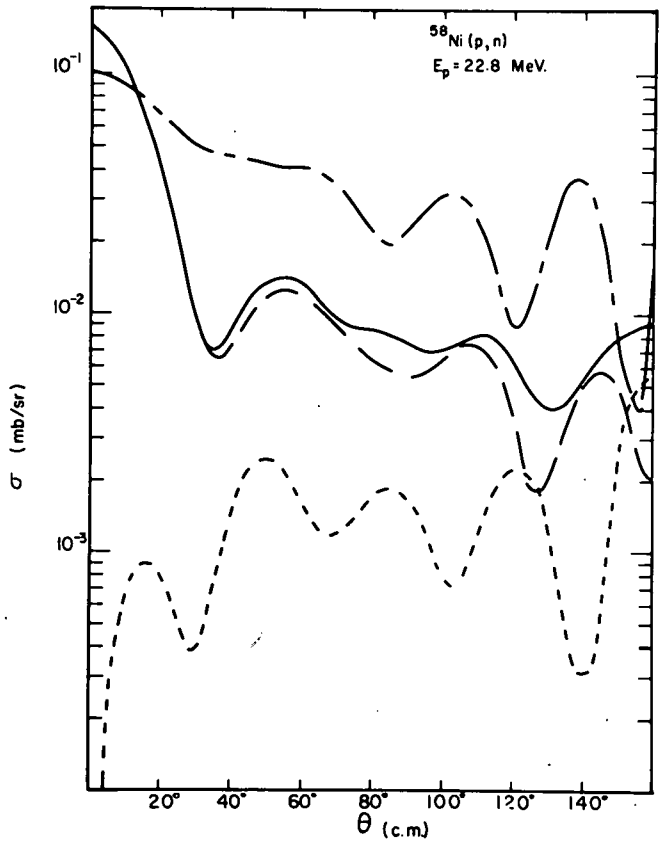

Fig. T6 ^{58}Ni(p,n) angular distributions assuming an $f_{5/2}$ transition and suppressing spin-orbit forces. Dashed curve is coherent non-spin-flip angular distribution, dashed-dotted curve is non-spin-flip two-step-only cross section, dotted curve is spin-flip two-step cross section and full curve is final (p,n) angular distribution.

$$U_{so} = V_{so} \left(\frac{\hbar}{m_\pi c}\right)^2 \frac{1}{r} \left(\frac{\partial f}{\partial r}\right) \vec{L} \cdot \vec{\sigma}$$

where

$$f = \frac{1}{1 + \exp((r - r_{so} A^{1/3})/a_{so})}$$

the usual parametrizations of elastic deuteron scattering have a weak spin-orbit part of short range,[4]

$$r_{so} \lesssim 0.85 \text{ F}$$

$$V_{so} \cong 6 \text{ MeV.}$$

In the adiabatic model, the spin-orbit potential would be nearly equal to the sum of proton and neutron contributions,

$r_{so} \cong 1.01$ F.

$V_{so} \cong 12$ MeV.

Fig. T7 shows the results of calculations for the $^{54}Fe(p,n)$ reaction with 22.8 MeV protons. While all other deuteron parameters are the same, we have varied V_{so} from 0 to 12 MeV. The

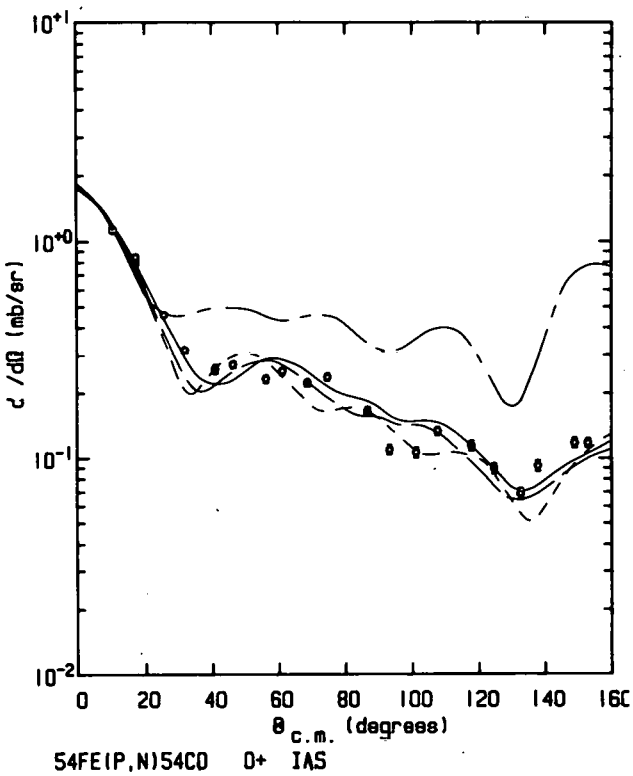

Fig. T7 Effect of deuteron spin-orbit potential on $^{54}Fe(p,n)$ at E_p=22.8 MeV. Deuteron spin-independent optical potential from adiabatic model.[1] Full curve has V_{so}=12, dashed curve has V_{so}=10, dotted curve has V_{so}=5, and dashed-dotted curve has V_{so}=0.

charge-exchange strength is taken to be 33 MeV. While the calculation for $V_{so} \cong 0$ has much the same, flat shape for $30° \lesssim \theta \lesssim 80°$ as the $^{54}Fe(p,n)$ angular distribution, the resemblance does not persist for nearby nuclei. Moreoever, the fit to the forward angles is lost when the charge-exchange strength is reduced to fit the magnitude at other angles.

A strength of V_{so}= 10±2 appears to provide the best fit to the phasing of the (p,n) angular distribution over a number of nuclei; and we are inclined to use the adiabatic model prescription for the deuteron-nucleus optical potential in such calculations, although other parametrizations are not completely excluded in this study.

---

[1] R. C. Johnson and P. J. R. Soper, Phys. Rev. C 1 (1970) 976.
[2] J. D. Harvey and R. C. Johnson, Phys. Rev. C 3 (1971) 636; G. R. Satchler, preprint, 1972.

[3] L. D. Rickertsen and P. D. Kunz, to be published, Phys. Lett., 1973.
[4] H. Wilsch, G. Heil, and G. Klier, in Polarization Phenomena in Nuclear Physics, Univ. of Wisc. Press (1971), Madison.
[5] R. Sherr et al., Phys. Rev. 139 (1965) B1292.

E. Macroscopic Analysis of (p,n) Reactions - P. D. Kunz and L. D. Rickertsen, with G. W. Hoffmann, Center for Nuclear Studies, University of Texas, Austin

A recent attempt[2] to extract the isovector part of the optical potential contains assumptions which need to be made explicit. When a parametrization of the nucleon-optical potentials over a range of nuclei and energies has been obtained, the isovector term may be extracted in a straightforward way. However, when a parametrization is obtained only for a single nucleus, one is forced to make assumptions concerning the division of the energy dependence between the isoscalar and isovector parts of the optical potentials. A typical parametrization[1] of the nucleon optical potentials for a target A is

$$U_{pA} = U_o - U_o'(E_p) - \xi U_1(E_p) + U_c$$

$$U_{nA} = U_o - U_o'(E_p) + \xi U_1(E_n)$$

where U_{pA} is the proton potential, U_{nA} is the neutron potential, U_o is the energy-independent isoscalar potential, U_o contains the energy dependence of the isoscalar part, U_c is the Coulomb correction term for the proton potential due to this energy dependence, $\xi=(N-Z)/4A$ and U_1 is the isovector part of the potential. U_c for ^{208}Pb is nearly 10% of the real part of U and nearly of the same size as the symmetry term, ξU_1. To extract an average U_1, we have

$$\bar{U}_1 = \frac{1}{2\xi}\left[U_{nA}(E_n) - U_{pA}(E_p) + \Delta U_1\right],$$

with

$$\Delta U_1 = U_c + U_o'(E_p) - U_o'(E_n).$$

In ref. 1, ΔU_1 has implicitly been assumed to vanish, and it was asserted that the resulting prescription for U_1 satisfactorily describes the energy dependence of the (p,n) reaction on ^{208}Pb and ^{209}Bi. We suggest the implied assumption is unreasonable. Since the usual parametrizations of the optical potentials contain only a real Coulomb correction, U_c, and a complex energy dependence in U_o', only the real part of ΔU_1 can possibly be cancelled unless one assumes the entire imaginary part of the energy dependence of U is contained in U_1.[3] This assumption is not justified as shown by careful analyses[3] of optical model parameters for N=Z nuclei.

In Fig. T8 we calculate the energy dependence of the (p,n) reaction on ^{208}Pb using the coupled Lane equations[2] and compare

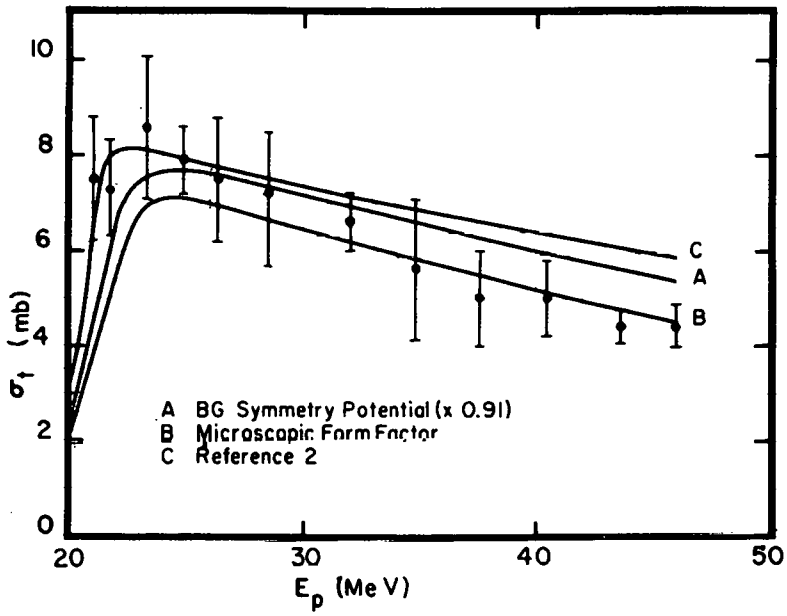

Fig. T8 Energy dependence of ^{208}Pb(p,n) excitation function. Form factors used in calculation: (A) proportional to BG symmetry potential, (B) derived from real, effective two-nucleon interaction, and (C) proportional to difference of neutron and proton optical potentials. Optical potentials described in text.

with data.[4] The calculations have been made with proton optical potentials taken from the Becchetti and Greenlees (BG) best fit parameter set[1] and the neutron parameters for $E_n < 16$ MeV from the study of Fu and Perey[5] (FP). Above this energy ($E_p > 35$ MeV) we have used the BG neutron parameters.[2] We have chosen three different prescriptions for the (p,n) coupling form factor which is proportional to U_1, with no effort to make the coupling consistent within the Lane model.[2] Curve A uses the symmetry term of the BG parameter, normalized by a factor of 0.9, for the coupling form factor. Curve B has been calculated using a form factor derived from a two-nucleon effective interaction of Yukawa form with a range of 1F and a strength of 16 MeV. In curve C we use the prescription of ref. 1, taking U_1 as proportional to the difference of proton and neutron optical potentials at their respective energies. The data does not allow us to choose between these prescriptions for the form factor and the use of proton and neutron optical parameters which fit the elastic scattering at the appropriate energies appears to be sufficient to explain the energy dependence of the total (p,n) cross sections.

---

[1] F. D. Becchetti and G. W. Greenlees, Phys. Rev. 182 (1969) 1190.
[2] G. W. Hoffmann, Phys. Rev. C 8 (1973) 761.
[3] W. T. H. van Oers, Phys. Rev. C 3 (1971) 1550.

[4] G. W. Hoffmann et al., Phys. Lett. 40B (1972) 453. This data is renormalized to the cross section of Schery (S. Schery, Ph.D. Thesis, Univ. of Colorado, 1973) at 26 MeV.

[5] C. Y. Fu and F. G. Perey, Oak Ridge National Laboratory, Report No. ORNL-4765 (1972), unpublished.

F. Computer Code Developments - P. D. Kunz and L. D. Rickertsen

CHUCK - The coupled channels code, CHUCK, has been improved to increase considerably its capability in size of cases handled and speed of computation. All the form factor options of DWUCK have been added to the program so that any DWBA calculation may be run via coupled channels if necessary.

DWUCK - The DWBA program, DWUCK, has been undergoing a continuous revision to make it ready for the next export version, DWUCK4. The improvements over the 9/Aug/69 version are 1) coherent summing of amplitudes, 2) change in angular momentum algebra and agreement more closely with that of Satchler[1], 3) first order finite range correction for multi-nucleon transfer, 4) compatibility with the IBM 360, 5) the cross sections may be plotted, 6) the program may be divided into two overlays for use on smaller computers, 7) a saving in time required for cases where the projectile has spin but no spin-orbit potentials, but where the full spin algebra is needed, 8) a 15% reduction in physical size of the program (without overlay), 9) correction of overflow difficulties in the angular momentum subroutines for large angular momentum transfers, and 10) compatibility of data input and output of results with previous versions of DWUCK.

[1] G. R. Satchler, Nucl. Phys. 55 (1964) 1.

IV. PUBLICATIONS AND REPORTS

A. Published Articles

Two-Nucleon Pickup from Spin 1/2 Targets II: ^{89}Y. R. J. Peterson and H. Rudolph, Nucl. Phys. A202 (1973) 335.

^{20}Na Beta Decay. P. D. Ingalls, Phys. Rev. C 7 (1973) 464.

Violation of Isospin Conservation in Two-Nucleon Pickup Reactions. P. D. Ingalls, Phys. Rev. Letters 31 (1973) 605.

(p,t) and (p,^{3}He) Reactions on ^{27}Al at E_p=27 MeV. R. Graetzer, J. J. Kraushaar, and J. R. Shepard, Phys. Rev. C 7 (1973) 199.

A Study of the Excited States of ^{57}Ni via the (p,d) and (^{3}He,α) Reactions at 27.5 and 37.7 MeV. F. M. Edwards, J. J. Kraushaar, and B. W. Ridley, Nucl. Phys. A199 (1973) 463.

Multi-Step Processes in the ^{12}C(^{3}He,α)^{11}C Reaction. R. N. Singh, N. De Takacsy, S. I. Hayakawa, R. L. Hutson, and J. J. Kraushaar, Nucl. Phys. A205 (1973) 97.

Study of the (p,t) Reaction on the Even-A Titanium Isotopes. H. W. Baer, J. J. Kraushaar, C. E. Moss, N. S. P. King, R. E. L. Green, P. D. Kunz, and E. Rost, Annals of Physics 76 (1973) 437.

Analysis of (π^+,p) and (p,π^+) Reactions. E. Rost and P. D. Kunz, Phys. Letters 43B (1973) 17.

Muscle and Serum Trace Element Profile in Uremia. H. Rudolph, A. C. Alfrey, and W. R. Smythe, Trans. Amer. Soc. Artif. Int. Organs XIX, (1973) 456.

The (^{3}He,t) Reaction on ^{54}Fe, ^{58}Ni and ^{60}Ni. H. Rudolph and R. C. McGrath, Phys. Rev. C 8 (1973) 247.

Beta Decay of ^{32}Cl and ^{40}Sc. C. Détraz, C. S. Zaidins, D. J. Frantsvog, R. L. Wilson, and A. R. Kunselman, Nucl. Phys. A203 (1973) 414.

Search for the Excitation of the Giant Dipole State by Direct Inelastic ^{3}He Scattering. R. J. Peterson, Nucl. Phys. A202 (1973) 557.

Remarks on Absorptive Potentials and Heavy Ion Elastic Scattering. L. D. Rickertsen, Phys. Lett. 41B (1972) 473.

Laser Evaporation and Elemental Analysis. J. K. Kliwer, J. Appl. Phys. 44 (1973) 490.

Determination of Trace Amounts of Fluorine by Nuclear Inelastic Scattering. H. Rudolph, J. J. Kraushaar, R. A. Ristinen, and R. R. Meglen, Proceedings of the 7th Annual Conference on Trace Substances in Environmental Health, Columbia, Missouri, June 1973.

A Study of the $^{113}In(^{3}He,d)^{114}Sn$ Reaction at 37.7 MeV. M. E. Cage, P. D. Kunz, R. R. Johnson, and D. A. Lind, J. Phys. 5 (1972) 1529.

Test of the Lane Model for Nucleon-Nucleus Optical Potentials. J. D. Carlson, D. A. Lind, and C. D. Zafiratos, Phys. Rev. Letters 30 (1973) 99.

The Level Structure of ^{48}Cr and ^{68}Ge from the (p,t) Reaction at E_p=27 MeV. J. R. Shepard, R. Graetzer, and J. J. Kraushaar, Nucl. Phys. A197 (1972) 17.

B. Articles Submitted for Publication

Inelastic Scattering Studies on ^{50}Cr. R. J. Peterson and E. W. Stoub, submitted to Nucl. Phys.

On Two-Step Processes via Particle Transfer Channels. P. D. Kunz and E. Rost, submitted to Phys. Lett.

Microscopic Calculations for (p,n) Reactions to Isobaric Analog States. L. D. Rickertsen and P. D. Kunz, accepted by Phys. Lett.

Comment on Macroscopic Analysis of the (p,n) Reaction. P. D. Kunz, L. D. Rickertsen, and G. W. Hoffmann, submitted to Phys. Rev.

Identification of Silver in a Periapical Lesion of a Tooth. E. H. Macintyre, J. K. McClatchy, H. Rudolph, and J. J. Kraushaar, to be published by Am. J. Clin. Path. in Nov., 1973.

The Radius of the Neutron Distribution in ^{208}Pb from (p,n) Scattering. S. D. Schery, D. A. Lind, and C. D. Zafiratos, accepted by Phys. Rev.

Field Mapping of the Dipole Magnets for the University of Colorado Energy-Loss Spectrograph. S. D. Schery and D. E. Prull, submitted to Nucl. Inst. and Methods.

Widths of Analog States in Heavy Elements from (p,n) Spectra. H. Fielding, S. D. Schery, D. A. Lind, C. D. Zafiratos, C. D. Goodman, submitted to Phys. Rev.

Thick Target Measurement of the (p,γ) Stellar Reaction Rates on the Nuclides ^{12}C, ^{29}Si, ^{46}Ti, ^{47}Ti, and ^{56}Fe. N. A. Roughton, M. J. Fritts, R. J. Peterson, C. S. Zaidins, and C. J. Hansen, submitted to Astrophysical Journal.

Charge Exchange Reactions on ^{91}Zr. P. D. Ingalls and H. Rudolph, submitted to Nucl. Phys.

Data Simulation Techniques for Reactions of the Form X(a,b,c)Y. M. J. Fritts and P. D. Parker, submitted to Nucl. Inst. and Methods.

Neutron-Proton Shell Model Multiplets in ^{88}Y and ^{90}Y from a Study of the $(\alpha,n\gamma)$ Reaction. H. W. Baer, R. L. Bunting, J. E. Glenn, and J. J. Kraushaar, submitted to Nucl. Phys.

Nuclear Data Sheets for A = 136. R. L. Bunting and J. J. Kraushaar, submitted for publication in Nuclear Data Sheets.

A Diffraction Spectrometer for Studies of Particle Excited Radiative Transitions. J. H. Jett, N. S. P. King, D. A. Lind, and P. Henning, accepted by Nucl. Inst. and Methods.

C. Published Abstracts and Conference Presentations

Scattering of 27 MeV Protons by Polarized ^{3}He. R. H. Ware, P. D. Ingalls, and W. R. Smythe, Bloomington Meeting of the APS, Nov., 1973.

The $^{12}C(d,p)^{13}C$ Reaction at 17.25 MeV. M. L. Munger and R. J. Peterson, Bloomington Meeting of the APS, Nov., 1973.

Comparison of Activation and Direct Measurement Yields for the $^{13}C(p,n)^{13}N$ (g.s.) Reaction. D. A. Lind, R. J. Peterson, and H. Fielding, Bloomington meeting of the APS, Nov., 1973.

The (p,α) Reaction on ^{90}Zr and ^{92}Zr. R. J. Peterson and H. Rudolph, Bull. Am. Phys. Soc. 17 (1972) 909.

The Levels of ^{106}Ag from the $^{103}Rh(\alpha,n\gamma)$, $^{107}Ag(p,d)$ and $^{106}Pd(^{3}He,t)$ Reactions. R. L. Bunting, S. Chinn, J. J. Kraushaar, R. J. Peterson, B. W. Ridley, and R. A. Ristinen, Bloomington meeting of the APS, Nov., 1973.

Two-Step Processes in Direct Nuclear Reactions. P. D. Kunz and E. Rost, Bull. Am. Phys. Soc. 17 (1972) 902.

Contribution of Single-Nucleon Transfer Channels to (p,n) Reactions. L. D. Rickertsen and P. D. Kunz, Bull. Am. Phys. Soc. 17 (1972) 903.

Aspects of Particle Transfer Channels in Two-Step Processes. P. D. Kunz, Gordon Research Conference on Nuclear Structure Physics, 1973.

Pion Reactions. E. Rost, Proceedings LASL Summer School, July, 1973 (to be published).

Utilization of the $^{19}F(p,p'\gamma)$ Reaction in Determining Trace Amounts of Fluorine. H. Rudolph, J. J. Kraushaar, R. A. Ristinen, and R. R. Meglen, Bull. Am. Phys. Soc. 18 (1973) 579.

A Progressive Encephalopathy Associated with Elevated Brain Tin in Chronic Dialysis Patients. J. Burks, E. Lewis, A. C. Alfrey, and H. Rudolph, Amer. Neuro. Assoc. 1973.

Thick Target Measurements of Astrophysically Interesting Cross Sections. N. A. Roughton, M. J. Fritts, C. J. Hansen, C. S. Zaidins, and R. J. Peterson, Bull. Am. Phys. Soc. 18 (1973) 651.

The Decay of ^{36}K. M. J. Fritts, Bloomington meeting of the APS, Nov., 1973.

Nuclear Reactions of Astrophysical Interest on Middle-Mass Nuclei. N. A. Roughton, M. J. Fritts, R. J. Peterson, C. S. Zaidins, and C. J. Hansen, Bloomington meeting of the APS, Nov., 1973.

Protons, X-Rays, and Trace Elements. H. Rudolph, R. A. Ristinen, and W. R. Smythe, Middle Atlantic Regional Meeting of the American Chemical Society, Jan., 1973.

Some Biological and Medical Applications of X-ray Fluorescence. H. Rudolph, Gordon Research Conference: Metals and Metal Binding in Biology, August, 1973.

Gamma-Ray Branching Ratios in ^{28}Al. C. E. Moss, Bull. Am. Phys. Soc. 18 (1973) 601.

$(^{3}He,2n)$ Excitation Functions on ^{9}Be, ^{24}Mg, and ^{27}Al. C. E. Moss and C. S. Zaidins, Bull. Am. Phys. Soc. 18 (1973) 603.

Operational Experience with a New Spectrograph System for Use with the University of Colorado Cyclotron. Invited paper at the Bloomington meeting of the APS, Nov., 1973, given by B. W. Ridley.

Measurements of Widths and Reaction Q-Values for the Analog State by the (p,n) Reaction in Pb and Bi. H. Fielding, S. D. Schery, C. D. Goodman, D. A. Lind, and C. D. Zafiratos, Bull. Am. Phys. Soc. 18 (1973).

Angular Distribution of the (p,n) Reaction on High-Z Nuclei at 25.9 MeV. S. D. Schery, H. Fielding, D. A. Lind, L. D. Rickertsen, and C. D. Zafiratos, Bull. Am. Phys. Soc. 18 (1973).

Differential Cross Sections for $^{10}B(p,n)^{10}C$ and $^{11}B(p,n)^{11}C$. C. D. Goodman, H. W. Fielding, and D. A. Lind, Bloomington meeting of the APS, Nov., 1973.

Angular Distribution of the Anti-Analog State of ^{56}Fe from the (p,n) Reaction at 23 MeV. H. W. Fielding, L. D. Rickertsen, P. D. Kunz, D. A. Lind, and C. D. Zafiratos, Bloomington meeting of the APS, Nov., 1973.

D. Theses

A Design for an Energy-Loss Spectrometer. Dale Eugene Prull, M.S., 1972.

The (p,n) Reaction on High Z Elements at 25.8 MeV Using a Rotating Beam Neutron Time-of-Flight System. Stephen Dale Schery, Ph.D., 1973.

V. PERSONNEL

A. Academic and Scientific

R. E. Anderson[1]	Research Associate
R. L. Bunting[2]	Research Associate
G. W. Edwards[3]	Research Associate
M. J. Fritts	Research Associate
C. D. Goodman[4]	Visiting Professor
P. D. Ingalls[5]	Research Associate
J. J. Kraushaar	Professor
P. D. Kunz	Professor
D. A. Lind	Professor
C. E. Moss[6]	Research Associate
R. J. Peterson[7]	Assistant Professor
L. D. Rickertsen	Research Associate
M. E. Rickey[8]	Visiting Professor
B. W. Ridley	Professor
R. A. Ristinen	Professor, Chairman of the Laboratory
E. S. Rost[9]	Professor
N. A. Roughton[10]	Research Associate
H. Rudolph[11]	Research Associate
M. J. Schneider[12]	Research Associate
W. R. Smythe	Professor
C. D. Zafiratos	Professor
C. S. Zaidins	Associate Professor

B. Technical and Support Staff

R. H. Akers	Electrician
R. C. Armstrong	Research Technician
J. Boyd[13]	Research Technician
E. C. DeGabain	Instrument Maker
B. A. Deobler	Design Engineer
L. A. Erb	Electronic Engineer
J. L. Homan	Research Technician
W. G. Minor	Instrument Maker
A. B. Phillips	Cyclotron Engineer
D. E. Prull	Research Physicist
J. N. Sonnenberg	Administrative Assistant
A. K. Wiles	Instrument Shop Foreman
D. H. Zurstadt[14]	Systems Analyst

C. Research Assistants

P. G. Brabeck
J. D. Burch
H. H. Chang
S. R. Chinn
H. W. Fielding[15]
R. A. Emigh
M. S. Iverson
M. L. Munger
D. R. Komonytsky[16]
S. D. Schery[17]
E. W. Stoub
R. H. Ware
W. R. Zimmerman

D. Other Students (Part-time)

T. Bowles[18]
B. Briggs
W. Buskirk[18]
S. Christensen
C. Cisneros[11,18]
M. DeHerrera[11,18]
S. Depetris
P. Doble[18]
W. Downum[18]
M. Forsythe[18]
S. Greene
C. Hanzon[11,18]
N. Iverson
L. Johnson
J. Leonard[18]
W. Lynch[18]
M. Mauro[11]
L. Peck
R. Perko
A. Randall
C. Roark
P. Schreck[11]
J. Speer[18]
L. Wolfson[11,18]

NSF SUMMER UNDERGRADUATE RESEARCH PARTICIPANTS

S. Chinn
A. Rosenthal
S. Wilmeth

---

1 Appointment began September, 1973.
2 NIRA appointment.
3 Part-time appointment which ended June, 1973.
4 Returned to Oak Ridge National Laboratory, August, 1973.
5 Appointment ended Sept., 1973. Now at California Institute of Technology, Pasadena, California.
6 Appointment ended July, 1973. Now at Los Alamos Scientific Laboratory.
7 Research associate appointment ended Aug., 1973. Now Assistant Professor in Department of Physics and Astrophysics, University of Colorado.
8 Appointment began Sept., 1973. On leave from University of Indiana, Bloomington, Indiana.
9 On leave at Saclay, France, for 1973-74 academic year.
10 Part-time appointment. Chairman, Department of Physics, Regis College, Denver, Colorado.
11 Partial NSF support.
12 Appointment began September, 1973.
13 Supported by NSF grant.
14 Appointment ended February, 1973. Now with Digital Equipment Corporation, Denver, Colorado.
15 Supported by the University of Wyoming.
16 Appointment ended December, 1972.
17 Ph.D., 1973. Now at Kenyon College, Gambier, Ohio.
18 Appointment ended 1973.